Light at the End of the Funnel: Fluorescence-Detected Two-Dimensional Electronic Spectroscopy to Probe Photosynthesis in Bacteria

by

Ariba Javed

A dissertation submitted in partial fulfillment
of the requirements for the degree of
Doctor of Philosophy
(Materials Science and Engineeting)
at The University of Michigan
2024

Doctoral Committee:

Professor Jennifer Ogilvie, Co-Chair
Professor Rachel Goldman, Co-Chair
Professor Eitan Geva
Professor John Heron

Ariba Javed

aribaj@umich.edu

ORCID iD: 0000-0003-1908-6361

Dedicated to my grandfather

ACKNOWLEDGEMENTS

I owe deep gratitude to my advisor, Prof. Jennifer Ogilvie for her support and guidance through the last 5 years. I have always admired her kindness and ability to see the humane side of things. Her thorough involvement in everyone's work in the lab and her efforts at making time for individual meetings every single week have always been a source of constant motivation for me during the Ph.D. I am always inspired by how beautifully she manages her personal life, while being one of the most respected names in the field.

I have had the chance to work with great collaborators during my Ph.D. I want to thank Prof. Manuel Joffre and Xavier Solinas for the many insightful discussions - I learnt a lot from them. I also want to thank Prof. Pavel Malý for working with us on the simulations and for coming up with new approaches to solve the different problems we faced.

I have met many talented and wholesome human beings as a part of the Ogilvie lab and I am grateful that I got to work with several of them, while building beautiful friendships over the years. I always enjoyed the morning before-the-lab discussions with Stephanie about work and our common love, food. You have always surprised me with very thoughtful gestures, the latest one being you bringing me a cake for the defense celebrations. I will always be thankful to Rhiannon who checked on me every few days when times were tough. I am inspired by Francesco's kindness and

considerate nature and want to thank him for introducing us to Arlina! I want to thank Yogita for simply being the sweetest, and for her aggressive support - it saved me on multiple days. I hope we get to go on many more trips together. Julian for all the scientific advice, and for being a really fun lab partner who always appreciated good banter. Thank you for facing LH2 with me. I wish Muyi, the man of most perfect one-liners, all the very best in his graduate studies.

I appreciate Riley's friendship and their efforts to always stay in touch. Libby for being an amazing human and for the much helpful career advice towards the end of my Ph.D. Veronica for showing me for the first time what a day in the laser lab looks like. I am extremely grateful to Vivek who I only had a week of overlap with but who managed to teach me a lot. Yassel for passing down the setup and the knowledge to me. Yin for letting me bother him with questions all the time. I am also thankful to Hoang for helping me out with wetlab things and to Damianos for working with me on the DAQ paper.

I am extremely grateful to my parents for their encouragement and limitless love. Being far away from home is not always easy, and I hope that I make you proud. My sister, a fellow Ph.D., for always being the one I look up to and for the care you show me. My brother, for always knowing the funniest things to say, and for being so affectionate and supportive. I consider myself immensely lucky for the many people I have come to form deep bonds with. I want to thank Priyal for a decade long friendship and one that I wouldn't know what to do without. I am grateful for Shivanshu who always had my back and tirelessly cheered me on throughout the Ph.D. I can't thank Shamalee enough for always being there to listen to my struggles, Ph.D. or otherwise. Diksha for being my favorite friend to share a meal and worries with. Brandon for being a constant support through life and through grad school

- I'll see you soon in Oregon! Hitesh for being one of the sweetest people I know. Abhishek for the walks and all the comical stories you always bring with you. Ekdeep for always knowing when to remind me that a catch-up is due. I also want to thank Ankit, Shwetha, and Achu for their love and for generously feeding us home-made food a countless number of times. I am grateful to Elsa, Anurag, Sumedh, Aman, Faraz bhai, and Partho for being there for me.

TABLE OF CONTENTS

LIST OF FIGURES

Figure

LIST OF ABBREVIATIONS

2DES Two-dimensional electronic spectroscopy

C-2DES Coherent two-dimensional electronic spectroscopy

F-2DES Fluorescence two-dimensional electronic spectrocopy

BChl Bacteriochlorophyll

TEM Transmission electron microscopy

AFM Atomic force microscopy

LH1 Light harvesting complex 1

LH2 Light harvesting complex 2

NMR Nuclear magnetic resonance

AO Acousto-optic

AOM Acousto-optic modulator

AC Autocorrelation

FWM Four-wave mixing

MZ Mach-Zehnder

BS Beam splitter

DS Delay stage

RM Retroreflector mirror

MC Monochromator

APD Avalanche photodiode

PR Photoreceiver

SP Short pass

LP Long pass

DM Dichroic mirror

AOB Air objective

DAQ Data acquisition card

YAG Yttrium Aluminum Garnet

WLG White-light generation

MIIPS Multiphoton intrapulse interference phase scan

RC Reaction center

OM Outer membrane

PM Plasma membrane

AFM Atomic force microscopy

RWA Rotating wave approximation

IR Infrared

DOPA Degenerate Optical Parametric Amplifier

ABSTRACT

Photosynthesis relies on solar energy absorption by the light-harvesting complexes and ultrafast energy transfer to the reaction centers, where the excitation is converted into a stable charge-separated state. This process happens with a high quantum efficiency $\sim$1. The mechanisms underlying the ultrafast energy and charge transfer in photosynthesis have been the subject of numerous spectroscopic studies. In this thesis, I focus on fluorescence-detected two-dimensional electronic spectroscopy (F-2DES) which offers high sensitivity and the ability to be combined with a microscope, an added advantage to its coherently-detected counterpart, C-2DES.

Fundamental differences between C-2DES and F-2DES techniques lead to strikingly different looking spectra. Currently, F-2DES is not very well-understood as compared to C-2DES and warrants more investigation. The light-harvesting 2 complex in photosynthetic bacteria is a well characterized pigment-protein complex and makes for an ideal model system to understand the potential of F-2DES for studying multichromophoric systems. In this thesis, we compare F-2DES and C-2DES by studying the energy transfer dynamics in purple bacterial LH2 using the two methods. From our experiments, we determine that C-2DES is clearly a better choice than the F-2DES to study energy transfer dynamics in large systems. This is because in case of F-2DES, an increasing number of chromophores in the system reduces the relative weights of pathways that can reveal energy transfer signatures to the ones that are

present as a large background in the signal. We also present preliminary F-2DES simulations on LH2 to support our findings. In addition, we report preliminary F-2DES measurements to probe the energy transfer in a newly discovered phototrophic bacterial species *Gemmatimonas phototrophica*. We point out that the F-2DES measurements may benefit from lower acquisition times, which would help achieve higher averaging. To this end, we present a rapid-scanning F-2DES methodology based on continuous time-delay scanning and digital lock-in acquisition. In addition, a broadband method capable of improving the bandwidth accessed with our current F-2DES measurements is demonstrated.

CHAPTER I

Introduction

Photosynthesis is a remarkable biological process that transforms light energy into chemical energy and forms the basis of most life on Earth [3, 9]. Performed by an enormous variety of phototrophs such as plants, algae, and certain bacteria [10], photosynthesis is nature's ingenious way to produce oxygen and to mitigate the carbon dioxide concentration in the atmosphere.

In the face of pressing environmental challenges such as climate change and air quality deterioration due to excessive burning of fossil fuels, there is an urgent need for sustainable energy sources. Several technologies focused on finding such solutions may benefit from an understanding of the underlying mechanisms involved in photosynthesis. For example, artificial photosynthetic systems, inspired by the efficiency and elegance of natural photosynthesis, are a promising renewable energy source. These artificial systems harness photovoltaic materials and utilize sunlight to promote photophysical processes or to produce solar fuels, making use of light-harvesting as well as excitation energy transfer principles [11]. Thus a better fundamental understanding of natural photosynthetic energy conversion may advance our ability to design improved material systems to meet our energy needs.

A detailed understanding of light-harvesting and energy transfer in photosynthesis requires the resolution of the fast timescales at which these processes occur in the photosynthetic apparatus. The development of ultrashort pulsed-light sources (mostly lasers) opened up the nanosecond (10^{-9} s) and picosecond (10^{-12} s) time domains to spectroscopists between the mid-70s and mid-90s [12–14]. Later, femtosecond lasers were developed leading to improved time resolution. The initial studies used an ultrafast technique called pump-probe spectroscopy, which uses one pulse called a pump to excite the sample and another time-delayed pulse, called the probe which investigates the state of the system as a result of the pump interaction. However, pump-probe spectroscopy is limited by the trade-off between temporal and spectral resolution: to obtain higher frequency resolution a narrowband pump pulse must be used, compromising the achievable time resolution. Two-dimensional spectroscopy (2DES) is an advantageous technique because it circumvents this problem by decoupling the time and spectral resolution dependence in a measurement using Fourier-transformation. A number of photosynthetic systems have been studied using this technique [15–17], which has been shown to enable the resolution of energy transfer pathways, charge separation mechanisms as well as coherent processes. Most previous studies have examined solutions of isolated components of photosynthetic systems, ignoring the interactions between these components. Photosynthetic membranes are known to show growth-dependent structural variation and heterogeneities [2], motivating improved methods that can provide higher sensitivity as well as spatial resolution to probe the structure-function relationship across spatial and temporal scales.

1.1 Bacterial photosynthesis

While green plants are commonly known to perform photosynthesis, releasing oxygen as a byproduct, there is strong evidence to suggest that anoxygenic photosynthesis occurred significantly earlier than the oxygenic photosynthesis performed by

plants [18]. In particular, bacterial photosynthesis emerged on Earth over more than 3 billion years ago [19]. This, as well as their well-characterized structures and the ability to genetically modify them, makes bacterial systems that perform anoxygenic photosynthesis useful model systems to shed light on the fundamental mechanisms of photosynthesis.

The primary events of photosythetic energy conversion and storage are strikingly similar across the wide variety of photosynthetic organisms present in nature [10]. A remarkable characteristic of the photosynthetic apparatus is its ability to adapt to environmental changes such as light quality and quantity, CO_2 levels, temperature, and nutrient availability [20]. Typically, the pigments involved in harvesting light in the photosynthetic unit are chlorophylls or bacteriochlorophylls, carotenoids, and bilins [21]. These pigments are packed into light-harvesting antenna complexes with structures that vary considerably among different photosynthetic organisms. The excitation energy harvested by the antennas is then transferred to the reaction centers (RCs) which initiate the charge separation process. Remarkably, the quantum yield of this process is close to unity [3]. Furthermore, the photophysical and photochemical reactions that follow the initial light absorption step are among the fastest events in biology, occurring on the timescales of picoseconds to a few nanoseconds. In particular, energy transfer during photosynthesis happens on a timescale of less than 100 fs to hundreds of ps [22, 23].

The solar spectrum is modified as a result of scattering and absorption in the atmosphere. At sea level, the visible and part of the near infra-red (NIR) spectrum is available for photosynthesis. However, under harsher conditions such as aquatic environments at increased depths, the intensity of light decreases as one goes deeper into the water column. Thus, the availability of red photons is reduced at such depths,

owing to their absorption in the upper layers for photosynthesis. The blue photons are reduced either due to absorption or scattering by suspended particles. Under such conditions, photons from the green and NIR regions of the solar spectrum are most abundant [24]. Moreover such environments are often anoxic, that is, lacking an abundant supply of oxygen for metabolic functionality. More examples of such harsh habitats include hot springs, marshes, sediments, sewage and wastewater, coral reefs, acidic lakes, permafrost, glaciers. Interestingly, they form thriving ecosystems for bacteria which have evolved to efficiently use the rather limited resources for survival.

To date, chlorophyll or bacteriochlorophyll-based photosystems have been found in bacterial species from seven phyla: Cyanobacteria, Proteobacteria (purple bacteria), Chlorobi, Chloroflexi, Firmicutes, Acidobacteria, and the most recently discovered Gemmatimonadetes [25]. In this thesis, we have studied energy transfer in purple bacteria and in Gemmatimonadetes. The next two sections provide a background on the structure and reported energy transfer in purple bacteria and Gemmatimonadetes respectively. The pigments responsible for light-harvesting in purple bacteria and Gemmatimonadetes are carotenoids, bacteriochlorophyll (BChl) *a* and *b*. Carotenoids absorb light in the green region before transferring the energy to the bacteriochlorophylls. They also play a key role in photoprotection by quenching the triplet excited states of BChls, as well as singlet excited states of oxygen. Unlike the carotenoids, BChls absorb in the visible as well as the NIR region. The structure of BChl *a* is shown in Fig. 1.1 (a), depicting its squarish-planar structure with a long hydrocarbon tail. At the center of the planar structure, a Mg atom is present and is conjugated to four nitrogen (N) atoms shown in blue. Most BChls are classified as bacteriochlorins because of their reduced rings (marked 1 and 2 in Fig. 1.1 (a)). The $\pi \rightarrow \pi^*$ transitions involving electrons in the π conjugated bacteriochlorin molecule make up the bands, as shown Fig. 1.1 (b), of the absorption spectrum of BChl *a*. The

two lowest-energy bands, called the Q bands, are classified as Q_x and Q_y according to the direction of their transition dipole moments along the x and y axes in the molecular plane. The higher energy band is called the Soret band (B band), having a mixed polarization. In addition, a vibrational progression is observed in the Q_y band, leading to a peak at 773 nm, arising from mixing between electronic and vibrational degrees of freedom [3]. The spectral properties of these pigments are affected by the protein scaffold that holds them in place, making up unique structures that form the light-gathering antenna complexes and the RCs.

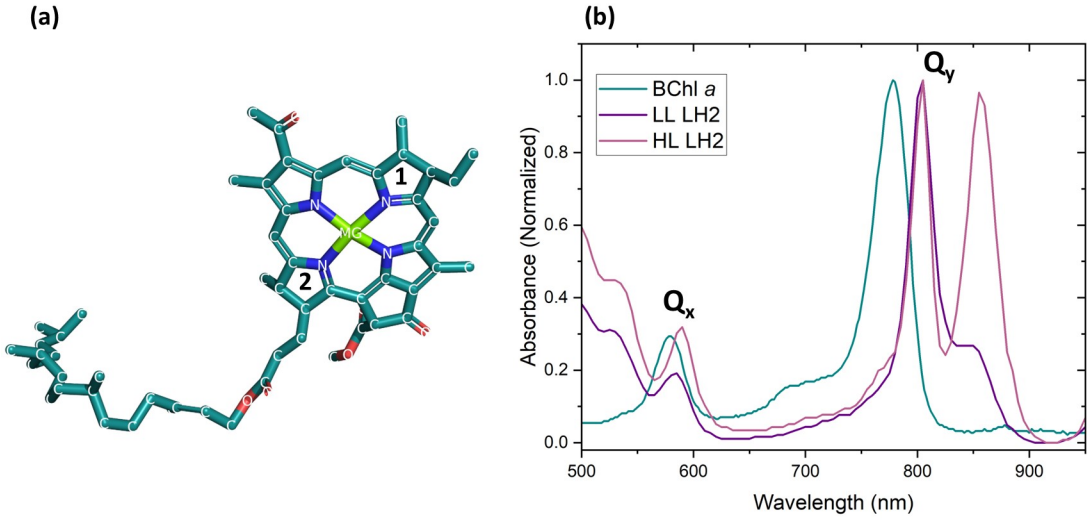

Figure 1.1: (a) Crystal structure of a BChl *a* molecule made up of a bacteriochlorin macrocycle and a phytyl tail. A Magnesium atom at the center (bright green) is conjugated to four Nitrogen atoms (dark blue). The greenish-blue and red segments represent Carbon and Oxygen respectively. Figure obtained from Protein Data Bank File N1KZ using PyMOL [1] (b) Room-temperature UV-Visible absorption spectra of BChl *a* (greenish-blue) in Toluene, LH2 from *Rhodopseudomonas palustris* grown under low-light, LL (dark purple) and high-light, HL (light purple) conditions. A clear red-shift in the BChl *a* absorption is observed as a result of pigment-protein interactions. In case of the B850 band, excitonic interactions also contribute to the strong red-shift.

Fig. 1.1 (b) highlights the spectral shifts for the light-harvesting complex 2 from *Rhodopseudomonas palustris* grown under different light-conditions. A red-shift is observed for the Q_x and Q_y bands, affecting the Q_y band more strongly. Different

protein environment is also often the cause of spectral inhomogeneities in pigment-protein complexes.

1.2 Light-harvesting (LH) complexes in purple bacteria

Purple bacteria are named for the characteristic red-purple appearance of many of the common species, resulting from the presence of bacterochlorophyll and carotenoids. Purple bacteria are anoxygenic phototrophs, and are found in a wide number of environments, especially anaerobic environments such as sewage treatment ponds. They are capable of using a variety of electron donors including H_2S or other compounds containing sulfur, organic compounds, or just H_2. It has been shown that most of these bacteria when grown under anaerobic conditions perform photosynthesis, while they show no expression of photosynthetic pigments and proteins when grown aerobically. Purple bacteria have been the focus of numerous structural and spectroscopic studies, making them the best understood photosynthetic organisms in terms of the energy collection and the primary energy transfer processes [3]. This motivates the use of the light-harvesting complex from purple bacteria as a model system for understanding the information available from the fluorescence-detected two-dimensional spectroscopy method developed in this thesis.

Two types of antennas are found in most purple bacterial photosystems - light-harvesting 1 and 2 complexes, LH1 and LH2. LH1 makes up the core antenna system and is usually closely associated with the RCs. LH1 usually occurs in

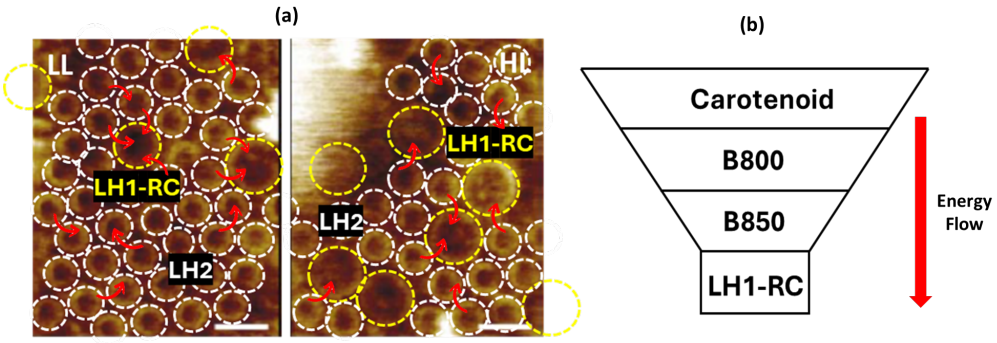

Figure 1.2: Spatial and energetic landscape in a bacterial photosynthetic membrane (a) AFM images (adapted from [2]) of the photosynthetic membrane from *Rhodopseudomonas palustris* grown under low-(left) and high-(right) illumination conditions, showing the spatial arrangement of LH1-RC core (small rings highlighted with white circles) complexes in a "lake" of LH2 antenna complexes (large rings highlighted with yellow circles). The higher relative ratio of LH2 to LH1-RC in case of low-light compared to high-light grown membranes is evident. The excitation absorbed by the LH2 complexes is transferred within and between LH2 before making it to the LH1-Rc complexes. (b) Energy funnel (Figure adapted from [3]), depicting the direction of excitation energy transfer within LH2, starting with absorption by the carotenoids, then to B800 and B850 rings that make up LH2. LH2 excitation is subsequently transferred to LH1-RC complexes.

a fixed proportion to the RCs, unlike the LH2 which serves as an accessory antenna and is present in variable amounts depending on the growth conditions, without being in direct contact with the RCs [3]. An understanding of the energetic and spatial landscape of the photosystem is important. A "funnel" model describes the energy transfer from the antennas to the RC quite well (Fig. 1.2 (b)). The blue-absorbing pigments absorb the initial excitation from the sunlight, and then transfer it further downhill to more red-absorbing pigments with some loss of energy in the form of heat. LH2 absorbs shorter wavelengths than LH1 which are proximal to the RCs. Thus, as one gets closer spatially to the RCs, the excitation energy moves to longer wavelengths, that is, it is effectively "funneled" to the RCs. Similarly, within the antenna complexes, carotenoids absorbing shorter wavelengths rapidly transfer energy to the BChls [3].

Initial fluorescence studies of purple bacterial photosystems have predicted that the RCs are spatially embedded in a "lake" of antenna complexes, enabling the antenna complexes to transfer excitation energy to any of the RCs in the lake [26]. Thus, the antenna complexes effectively increase the absorption cross-section of the RCs, both spectrally and spatially [3, 11]. An AFM image of the photosynthetic membrane (adapted from ref. [2]) of the purple bacterium *Rhodospirillum photometricum* is shown in Fig. 1.2 (a), depicting this arrangement of LH2 antennas around LH1 antennas (small rings, ∼50 Å) bound to RC in the form of LH1-RC core complexes (elliptical in shape). The two images also highlight the influence of light conditions on the ratio of LH2 to LH1-RC needed for optimum excitation energy concentration. Under low-light (LL) conditions more LH2 is present relative to LH1-RC, consistent with the fact that under such conditions, more LH2 is required for light-harvesting. On the contrary, high-light (HL) adapted membrane shows a smaller LH2/LH1-RC ratio (∼3.5 compared to 7 in case of LL) but a more homogeneous distribution of complexes compared to LL adapted LH2 [2]. This adapted architecture ensures adequate light gathering under LL conditions while preventing photodamage under HL conditions. Thus, the structural modulation of the photosynthetic membrane plays a key role in modifying the energy harvesting and transfer mechanisms.

1.2.1 Double-ring structure of LH2

The structure of LH2 from several purple bacterial species has been well characterized by X-ray diffraction studies [8, 27–29]. LH2 is comprised of units with a heterodimer of two protein subunits, namely the α and β apoproteins, three non-covalently bound BChl molecules and one carotenoid molecule. The complex is made up of two concentric rings of helical protein subunits with the α-poplypeptides inside and the β-polypeptides outside [22], shown in Fig. 1.3 (a). The protein subunits further rearrange into two separate symmetric ring-shaped units [3]. The two rings

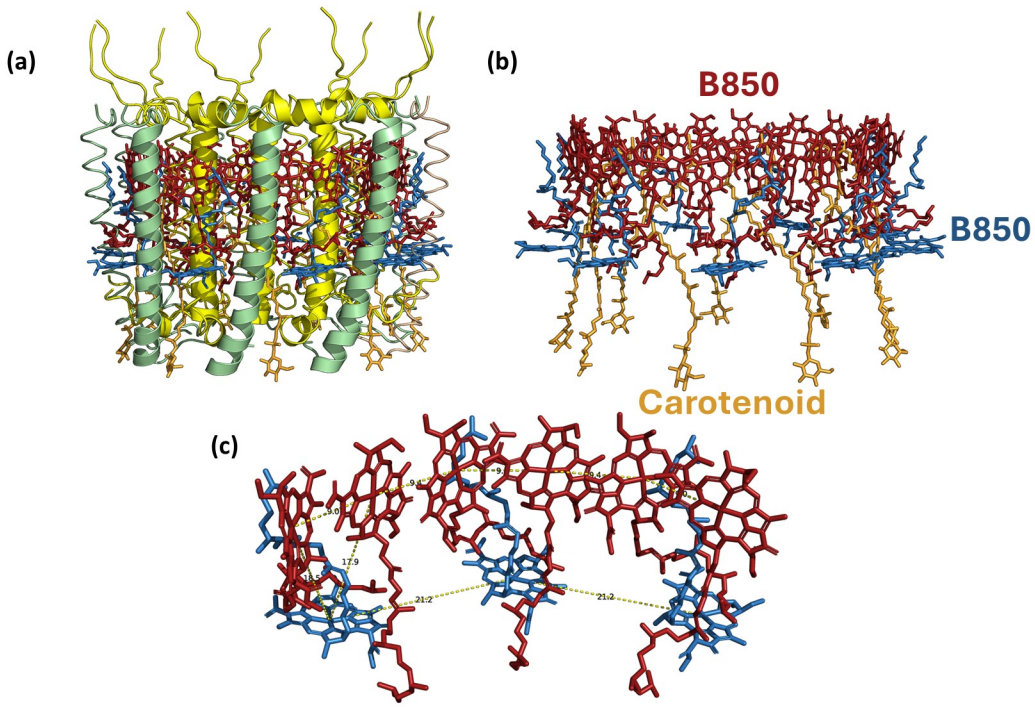

Figure 1.3: Crystal structure of light-harvesting LH2 complex from *Rhodoblastus acidophilla (Rbl. acidophilla)* (a) With the protein scaffold. α and β polypeptides are shown as yellow and green ribbons (b) Without the protein structure. B800 and B850 rings are shown in blue and red, the carotenoids are shown in orange (c) A segment of the LH2 complex showing the inter-pigment distances in Å. Figure obtained from the Protein Data Bank Library 1NKZ using PyMOL [1].

are named B800 and B850 after their respective absorption maxima (Fig. 1.1 (b)). The B800 ring consists of 8-9 weakly coupled BChl molecules (coupling ∼30 cm^{-1}) with the bacteriochlorins arranged parallel to the plane of the membrane in which the complex is embedded. The inter-pigment distance in B800 is approximately 21 Å. B850 ring, on the other hand, is made up of more strongly coupled (coupling ∼250-400 cm^{-1} [30]) BChl *a*-BChl *a* dimers forming a band of 8-9 units in a plane perpendicular to that of the membrane, with inter-pigment distances around 9 Å [22]. The inter-pigment distances in the two rings are shown in Fig. 1.3. The noticeable BChl *a* absorption shift from 800 nm to 850 nm in the B850 ring is caused both by pigment-protein interactions as well as excitonic interactions between neighboring BChl *a* molecules in the ring. Excitonic delocalization is one of the crucial features

of energy transfer in LH2, and the resulting excitonic states are given as superpositions of the individual excited molecular states. The nearest neighbour couplings in B850 are ∼300 cm^{-1}, which is nearly ten times that between the chromophores in the B800 ring [31, 32]. Thus, the strong electronic interactions in the B850 ring result in an energy gradient directing downhill excitation transfer from B800 to B850. Lastly, the carotenoid molecules in LH2 lie generally perpendicular to the membrane plane, very close (3.4-3.7 Å) to both the B800 and B850 pigments [3]. Carotenoids also play a important structural role in LH2 by effectively bolting together adjacent $\alpha\beta$-apoprotein pairs together [30]. Fig. 1.3 shows the crystal structure of LH2 derived from the purple non-sulfur purple bacterium *Rbl. acidophilla*, on which all the measurements reported in Chapter IV have been performed. The structure with and without the protein scaffold is shown, with 9 BChl *a* monomeric and dimeric units forming the B800 and B850 rings respectively. Center-to-center separation of BChl *a* in B800 is 21.3 Å, while in the B850 ring it is much smaller, at 9.5 Å within each $\alpha\beta$ apoprotein unit, and at 8.8 Å between two closest BChl *a* molecules in adjacent $\alpha\beta$ apoprotein units [30]. It is worth pointing out that the different degrees of excitonic delocalization in the B800 and B850 bands in LH2 play an interesting role in the manifestation of energy transfer dynamics extracted using fluorescence-detected two-dimensional spectroscopy, and this will be the focus of discussion in Chapter IV.

1.2.2 Energy transfer dynamics in LH2: Previous spectroscopic studies

LH2 is one of the most widely studied photosynthetic antenna complexes, forming the subject of a number of structural as well as spectroscopic studies [22, 30, 33]. In particular, the initial energy transfer within LH2 before further downhill transfer to LH1-RC is a crucial and fundamental step that sheds light on pigment-pigment and pigment-protein interactions in the B800 and B850 rings. It has been revealed that even though the bacteriochlorin planes in the B800 and B850 rings are perpen-

dicular to each other, their Q_y transitions are rather parallel, enabling B800→B850 energy transfer [30]. Fig. 1.3 (c) depicts the relative distances and orientations of the B800 and B850 BChl *a* pigments. The classical Förster theory, describing weak interactions between a donor and an acceptor, breaks down [1] when the distances between interacting pigments are smaller compared to the size of the pigments, as is observed in the B850 ring of LH2. In line with this reasoning, the measured experimental rates of energy transfer are not correctly described with the classical Förster mechanism. Instead, the excitonic picture accounting for delocalization spread across several pigments, limited by factors such as static disorder, is a more accurate description. Other approaches such as generalized Förster resonance energy transfer [34], multichromophoric Förster resonance energy transfer [35], and modified Redfield theory [36–38] have been used to describe the excitation energy transfer in the antenna system.

Within LH2, energy transfer can occur between carotenoids to BChl *a* molecules as well as between BChl *a* molecules. The latter encompasses intra-ring energy transfer within the B800 and B850 rings, in addition to the B800→B850 excitation transfer. The B800→B800 energy transfer competes with the B800→B850 transfer and has been reported to occur on a timescale of ∼1.5 ps in LH2 complexes from *Rbl. acidophilla* using absorption anisotropy decay studies [39, 40] as well as three-pulse echo shift peak and transient grating [41] studies. Slightly faster time-scales (∼ 0.5 ps) for B800-B800 energy transfer have been reported in other studies and can be inferred from the Förster energy transfer description owing to the weak coupling between the BChl *a* molecules in the B800 ring [22]. An additional ∼300 fs isotropic decay component has been observed and attributed to possible vibrational relaxation and/or excitation transfer [39].

B800→B850 energy transfer and coherence dynamics using LH2 from different purple bacterial species has been studied extensively by many groups in the last 40 years [1, 39, 40, 42–55]. Initial time-resolved absorption anisotropy decay studies reported energy transfer time for *Rhodobacter sphaeroides* to be 1 ps [42, 56, 57]. Later, two-color transient absorption studies conducted at room temperature determined it to be close to 0.7 ps [44], a timescale which has been reproduced with polarization-controlled 2DES studies [58]. Other 2DES studies have also resolved the B800-B850 energy transfer, reporting similar timescales [58–60]. The time constant for the B800-B850 energy transfer in LH2 from *Rbl. acidophilla* at room temperature is reported to be 0.8-0.9 ps [40, 45]. Furthermore, large temperature independence of the B800-B850 energy transfer step has been revealed, showing only slower rates of 1.8-2.4 ps at low temperatures of 1.4-10 K [40, 61].

Once excitation reaches the B850 ring, it is rapidly delocalized over many BChl *a* molecules, but due to disorder this excitonic wavepacket becomes more localized within ∼0.1 ps. The ultrafast decay happening under 0.1 ps has been reported from different measurements, including transient absorption [62, 63], three-pulse echo shift peak [64] and all-parallel polarization 2DES [58] studies, and has been attributed to relaxation to the lowest excited state in LH2, and indeed to the reduction of the coherence length of the exciton. This resulting localized excitonic state then migrates around the ring on a very fast timescale, before eventual energy transfer to LH1.

1.3 New class of phototrophs: *Gemmatimonas phototrophica*

The first known phototrophic member from the phylum Gemmatimonadetes, *Gemmatimonas (G.) phototrophica* or AP64 was reported in 2014 [19]. It was isolated from

a freshwater lake in the Gobi desert in North China, revealing its abilities to exist in unique habitats [19]. *G. phototrophica* shows the highest biomass yields under semi-aerobic conditions (reduced oxygen concentration 9.8 %-15.2 % compared to the 21 % in the atmosphere) [4]. It has been found that *G. phototrophica* is not an obligate phototroph, meaning that it doesn't exclusively rely on light as a source of energy for its metabolic activity. For its survival, it requires a supply of organic substrates, and is able to exhibit growth in the dark. Thus, instead of being the sole pathway to obtain energy, the photosystem in AP64 may act as an additional source to do so, providing an advantage over purely heterotrophic members of the genus *Gemmatimonas* increasing the chances of survival in harsh environments [4].

The photosystem in *G. phototrophica* is made up of a BChla *a*-containing Pheophytin-quione based RC (classified as type-2 RC), typically found in anoxygenic photosynthetic bacteria, such as purple bacteria. The similarity in the photosynthetic apparatus between *G. phototrophica* and purple bacteria, in addition to their analogous photosynthetic gene cluster organization and close phylogenetic relationship of their photosynthesis genes suggests that phototrophy in Gemmatimonadetes bacteria emerged as a result of a horizontal photosynthesis gene transfer from a purple photosynthetic bacterium [25], although how the gene transferred happened between the distant phyla is yet unclear. Thus, *G. phototrophica* is an important system that provides insights into the evolution of photosynthesis, and reveals the nature of horizontal gene transfer between distant phyla. This interesting phenomenon has relevance to synthetic biology and to attempts to reprogram heterotrophic bacteria for light-powered metabolic processes [65]. So far very little is known about the how the growth conditions like light and oxygen regulate the expression of the photosynthetic genes in *G. phototrophica*. Another open question pertains to the mechanism of light harvesting and energy transfer in the *G. phototrophica* photosystem, meaning that

there is a huge scope for structure-function relationship studies. A recent study [5] answered the preliminary questions in this direction. We aim to explore in greater depth with the help of multidimensional spectroscopy.

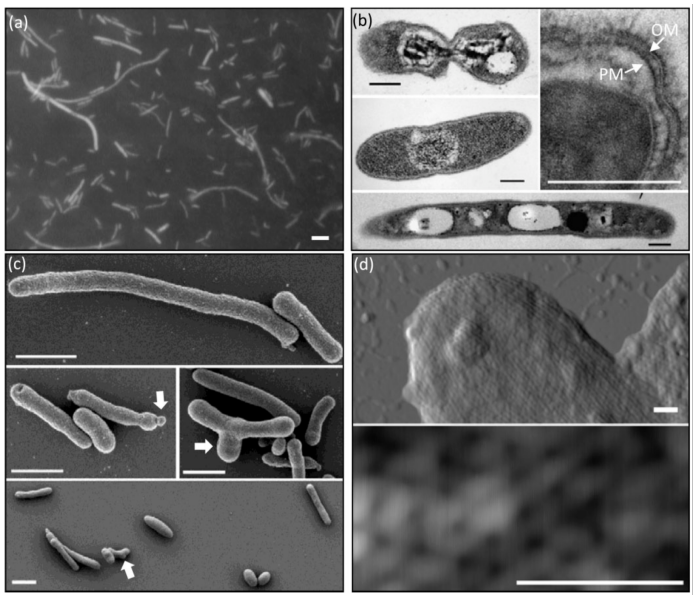

Figure 1.4: Microscopic images of AP64 cells. (a) Infrared fluorescence image showing rod- and long filament- like cells. Bar: 1 μm. (b) Transmission electron micrographs: Outer membrane (OM), Plasma membrane (IM). Bar: 200 nm. (c) Scanning electron micrographs. Arrows point out the budding structures. Bar: 1 μm. (d) Atomic force microscopy (AFM) deflection images revealing porous surface layer with hexagonal structures. Bar: 100 nm. Figure adapted from [4].

1.3.1 Double-ring structure of the *G. phototrophica* photosystem

Fig. 1.4 (adapted from [4]) shows the microscopic images of *G. phototrophica* cells, which are rod-shaped with a width of 0.3-0.5 μm and a length of 1-6 μm. Transmission electron microscopy (TEM) images show structures of gram-negative cell envelope and the cells contain electron-dense small bodies and transparent vesicle-like structures. The cells reproduce by binary fission and are motile, consistent with the fact that its genome contains flagellar biosynthesis genes. Atomic force microscopy (AFM) images show hexagonal features with 30 nm diameter at cell surface.

Fig. 1.5 shows the crystal structure of *G. phototrophica*. The relatively simple photosystem of Bchl-based phototrophs consists of a specific type of RC surrounded by a ring of light-harvesting 1 (LH1) subunits, sometimes accompanied by smaller rings of LH2 complexes [66]. A recent work [5] revealed the structure of the photosynthetic core complex from *G. phototrophica*. Particles of the purified complex are ∼20 nm in size, much larger than the previously described RC-LH1 complexes which are ∼16 nm in size [67, 68]. As seen from Fig. 1.5 (a), the complex consists of an RC at the center, with a surrounding LH1 ring similar to the one found in RC-LH1 complexes [67, 68], and a concentric outer surrounding LH ring (referred to as LHh) of a new kind. The antenna component of the double-ring complex designated as RC-dLH is thus collectively composed of LH1 and LHh. This double, concentric LH complex is made up of heterodimeric units of transmembrane α- and β-polypeptides. The inner LH1 ring consists of 16 pairs of α/β apoproteins, while the outer LHh rings has 24 subunits. The LH1 α-β heterodimers are interlocked by partially overlapping bacteriochlorin rings of the BChls, with few specific protein-protein interactions. Both LH1 and LHh are slightly elliptical (Fig. 1.5 (a)) and have pseudo-C8 symmetry. It should also be noted that the distances of the LH1-β helices to the LHh-α helices are much shorter than the helical distances within LH1 rings, suggesting strong protein-protein interactions [5].

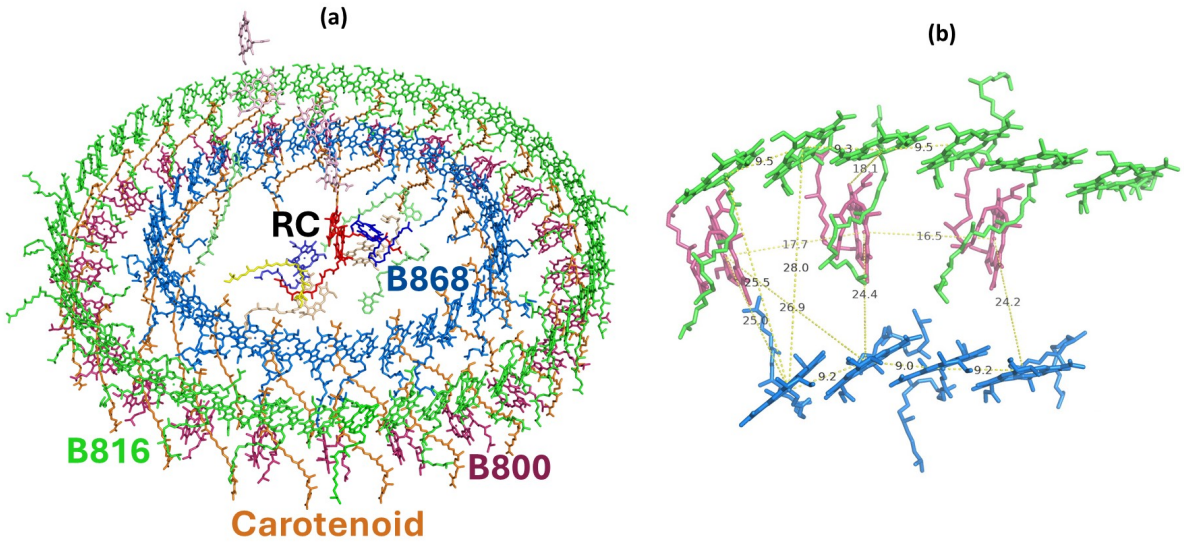

Figure 1.5: (a) Crystal structure of the dlh-RC complex from *Gemmatimonadetes phototrophica*, shown without the protein scaffold for clarity. Three concentric pigment-protein rings are present -B800 and B816 make up the outer LHh ring and B868 represents LH1. At the center, the RC is shown. (b) A segment of the dlh-RC complex is shown, with the different inter-pigment distances given in Å. Figure was obtained from the Protein Data Bank Library 7o0u [5] using PyMOL.

.

Not surprisingly, the overall RC architecture is similar to that present in phototrophic Proteobacteria [67, 68], exhibiting L and M transmembrane subunits, as well as a bound cytochrome c exposed on the periplasmic side of the complex. The RC also has similar pigment architecture to purple bacteria. However, the presence of membrane-extrinsic polypetides have been reported to distinguish the RC-LH1 subcomplex of *G. phototrophica* from purple bacteria [5].

1.3.2 Spectral features of *G. phototrophica* RC-dLH complex

Purple phototrophic bacteria usually have relatively small LH2 rings that absorb light and transfer the excitation energy to LH1 to be further passed on to the RC which performs the charge separation step in photosynthesis [30]. Despite the lack of LH2 in its photosystem, the LHh ring in *G. phototrophica* plays a similar role, adding

two infra-red BChl a 800- and 816- nm absorption bands to the 868-nm absorption of the inner LH1 ring (the 77 K absorption spectrum is shown in Fig. 1.6), building an energy gradient to funnel energy to the RC. A carotenoid band is present with absorption peaks at 478. 507, and 542 nm. The oscillol series carotenoids do not play a role in light-harvesting, but are important for photoprotection, as is reflected in the high carotenoid to BChl *a* ratio of 5.5 ± 1.7 mol:mol [19].

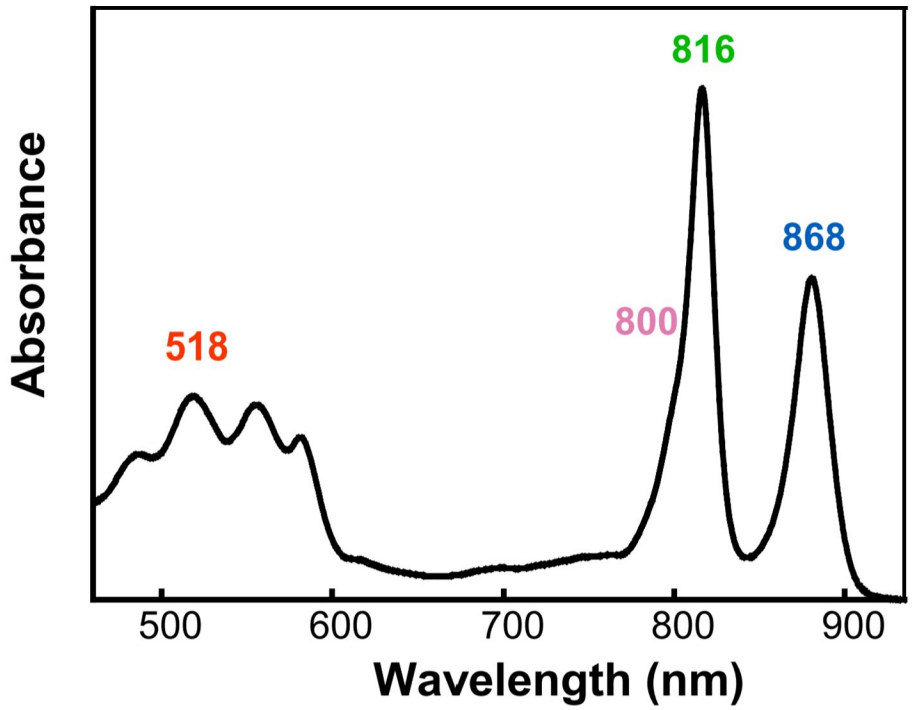

Figure 1.6: 77 K absorption spectrum of the RC-dLH complex. Red label represents Carotenoid absorption, pink corresponds to B800 absorption, green to B816, and blue depicts the B868 band. Figure adapted from [5]

.

1.3.3 Energy transfer dynamics in *G. phototrophica*

The first (and so far, the only) report on the energy transfer dynamics between the different pigment networks in *G. phototrophica* were made by Qian and co-workers [5] using transient absorption measurements. They determined with a sub 0.3 ps rise

of the 816 nm signal that in the outer LHh ring, energy transfer occurs from the S_2 state of the initially excited carotenoids. They also found that this S_2 pathway is also active for energy transfer to B868 in the LH1 ring. Of the excited carotenoid S_2 population that is not transferred via the S_2 pathway, some fraction relaxes to the lowest carotenoid excited state, which is a coupled S_1/ICT state (ICT stands for Intramolecular charge transfer). The shortened lifetime, as determined in [5], suggests that the S_1/ICT state can act as an energy donor to low energy BChls, likely within the LH1 ring. The carotenoid-B800 energy transfer is reported to be negligible, if present at all.

Energy transfer in the outer LH1 ring was also probed by Qian and co-workers [5]. They found that B800-B816 energy transfer occurs on a time scale of $\sim$0.4 ps. The time evolution of transient absorption spectra shows that the B800 BChls are preferentially excited at 785 nm and transfer energy to the BChls absorbing at 820 nm. Inter-ring energy transfer from B816 in LHh to B868 in the LH1 ring happens at $\sim$2 ps, faster than the 3-5 ps energy transfer between LH2 and LH1 complexes in purple bacteria [14]. Finally, B868 decay is attributed to the slow energy transfer to the RC.

1.4 Thesis overview

This thesis explores the potential of fluorescence-detected two-dimensional electronic spectroscopy (F-2DES) in comparison to its coherently-detected counterpart to elucidate energy transfer dynamics in multichromophoric systems. We also propose implementations of F-2DES to achieve increased signal-to-noise ratios as well as broader bandwidth capabilities. Coherently-detected two-dimensional electronic spectroscopy (C-2DES) leverages the simultaneous high temporal and spectral resolution of Fourier-transform based 2DES. By correlating excitation and detection frequencies on a 2D map, it provides information about electronic couplings, correla-

tions, and energy transfer dynamics in a system. In C-2DES, signal is emitted due a macroscopic polarization generated as a result of three pulse interactions. As a result, the system sizes that can be studied using C-2DES are limited to $\sim \lambda^3$ because a coherent build-up of the signal is required [69]. Thus, the C-2DES signal is averaged over an ensemble of molecules, and hence, poorly suited for single-molecule studies as well as spatially resolved measurements. F-2DES, using an additional fourth-pulse interaction to generate an incoherent signal as the observable instead of a coherent field, circumvents this limitation. The increased sensitivity offered by F-2DES, in addition to the ease of implementation in a miscroscope, is ideal for spatially resolved measurements and has been previously demonstrated by our group [70] on LH2 grown under different illumination conditions.

The advantages offered by F-2DES motivate its use for further studies on photosynthetic systems with the objective of understanding the structure-function relationship on a molecular level. However, it has been pointed out that the interpretation and understanding of F-2DES is not straight-forward [71]. The addition of a fourth pulse leads to additional Liouville pathways that change the appearance of F-2DES spectra compared to C-2DES spectra for the same systems. Furthermore, the longer excited state lifetime of fluorescence leads to longer detection times, making it prone of additional dynamics, such as exciton-exciton annihilation and incoherent mixing, during this time [72, 73]. Thus, the detection scheme in F-2DES itself introduces additional complexities to the signal. We compare the theory of F-2DES with its well-understood counterpart C-2DES in Chapter II. Chapter III describes experimental implementation of F-2DES using phase-cycling and phase-modulation methodologies. We describe the implementation of our lock-in detection based phase-modulated setup, first demonstrated by Tekavec et al [74]. Some basic tests done prior to the measurements to make sure that the signal is free from detector non-linearity

effects are also shown. In Chapter IV, we investigate the capability of F-2DES to report on energy-transfer dynamics in multichromophoric systems using LH2 as a model system. We highlight high suppression in the signatures of energy transfer dynamics compared to C-2DES and establish that such signatures are system-dependent, with the delocalization in the system changing the relative weights of pathways that carry energy transfer signatures against a constant background. A simplistic simulation to support the energy transfer dynamics in F-2DES is also provided, in addition to C-2DES measurements on LH2. In Chapter V, we report F-2DES and energy transfer in the recently discovered dLH-RC complex of AP64. We observe, interestingly, larger energy transfer signatures in F-2DES relative to LH2. Future C-2DES measurements, which, as we show in Chapter IV, are clearly better suited for resolving energy transfer in large systems, will be used to better characterize the energy transfer process in dLH-RC.

We find that a large amount of signal averaging is required to reveal the energy transfer signatures in F-2DES. This makes the measurements vulnerable to laser noise and at the same time, dictates the need for overall faster measurements to enable high averaging. In Chapter VI, we demonstrate a rapid-scanning implementation of F-2DES based on digital lock-in acquisition and Fourier-filtering in post-processing. The methodology is demonstrated for a specific waiting time but can be readily extended to also rapidly scan the waiting time, enabling high averaging for observing energy transfer with improved signal-to-noise ratios. In addition, we address the bandwidth limitations imposed by the use of acousto-optic modulators (AOM) in our F-2DES setup by introducing an alternative phase-modulation based scheme in Chapter VII and provide results for the proof of concept. In addition to use in microscopy, this implementation will be useful as a broadband probe to correlate the excitation and detection in systems with a wide range of interacting absorbers. Chapter VII also

discusses future directions such as time-gating in F-2DEs which will be useful in revealing the detection-time dynamics. In addition, a separation of the pathways contributing to the overall signal is proposed. Chapter VIII summarizes the work in this thesis and discusses some potential systems that could be well-suited to exploit the advantages offered by F-2DES.

CHAPTER II

Non-Linear Two-Dimensional Fourier-Transform Spectroscopy

This chapter covers the basic framework required to understand material properties through their interactions with light fields. A semi-classical perturbative approach to predict and interpret spectroscopic signals is detailed. Different relevant non-linear spectroscopic techniques, their implementation, and the information provided by them are also detailed. Emphasis is placed on 2DES which decongests spectral features that are otherwise obscured in one-dimensional spectroscopies, especially for systems like photosynthetic complexes with multiple absorbers and high energetic disorder. 2DES enables the measurement of ultrafast dynamics in photosynthetic systems with high temporal and spectral resolution. Its fluorescence-detected variant, which is the main focus of this thesis, is discussed as a method that offers increased sensitivity and compatibility with a microscope to enable imaging. A description of the root of complexities in the interpretation of F-2DES spectra is made as a way to lay the groundwork for Chapters IV and V.

2.1 Theory

2.1.1 Non-linear optics

Light-matter interactions and modification of the optical properties of a material system by the presence of light form the basis of optical measurements and spectroscopy. The electronic motions and relaxation processes that take place as a result of these light-matter interactions manifest as a change in material polarization. Typically, an intense input light field from a laser is needed to see a non-linear dependence of the induced polarization on the intensity. Non-linear spectroscopy makes use of such phenomena, described using the principles of non-linear optics [75, 76], to provide insights into the electronic structure, interactions and relaxation processes, as well as ultrafast energy and charge transfer dynamics of interesting material systems.

In the context of electronic interactions, material response to a light field can be understood by considering that a material system is a collection of charged particles: electrons and ion cores. When an electric field is applied to charged particles, positive charges tend to move along the direction of the field while negative charges move in the opposite direction. In dielectric materials, the charges are held in place by bonds, which possess "elasticity" [76]. As an effect of the applied electric field, these bound positive and negative charges are displaced from their usual positions by an amount that is determined by the strength of the field. This movement of the charges results in a collection of electric-dipole moments. Thus, the applied field induces a net polarization in the dielectric material [76].

To further elaborate on the above picture, let us consider a mechanical analogy of a spring with two attached masses, the heavier (and hence, stationary) ion core and the mobile electron. The displacement x of the electron of mass m and charge $-e$ as

a result of the force $-eE(t)$ due to the applied electric field $E(t)$ varies according to an equation of motion for an oscillator:

$$m\left[\frac{d^2x}{dt^2} + 2\Gamma\frac{dx}{dt} + \Omega^2 x - \left(\xi^{(2)}x^2 + \xi^{(3)}x^3 + ...\right)\right] = -eE(t) \tag{2.1}$$

where the left-hand side is the restoring force of the spring, and Γ is a damping constant, Ω is the resonance frequency, and the term $(\xi^{(2)}x^2 + \xi^{(3)}x^3 + ...)$ accounts for the non-linearity of the displacement x as a response to the input field E, and $\xi^{(n)}$ are constants. For a weak input field E, the displacement x is small, and the non-linear term becomes insignificant. Then the response of the material to $E(t)$ can be considered harmonic. In this case, when an electric field $E(t)$ of the form

$$E(t) = Ee^{-i\omega t} + c.c. \tag{2.2}$$

is substituted in 2.1, we obtain a linear dependence of the position x in $E(t)$ oscillating at the frequency ω of the optical field. If we consider N electric dipoles per unit volume, the induced polarization is given by $P = -Nex$. Hence, the polarization P will also vary linearly with $E(t)$ and describes the linear optical properties of the medium.

If, however, the electric field E is significant, it leads to a large displacement x about the equilibrium position and the restoring force becomes highly non-linear in x, i.e. the spring becomes distorted when the extension or compression is large. The anharmonic response, accounted for by the terms $\xi^{(2)}x^2+\xi^{(3)}x^3+...$, leads to an induced polarization P which varies non-linearly with $E(t)$[76]. This non-linearity underlies non-linear phenomena such as second-harmonic generation, two-photon absorption, self-phase modulation, four-wave mixing, to name a few. Non-linear spectroscopy utilizes these non-linear processes which, as described above, can arise from interactions with an intense electric field as well as with multiple independent electric fields. Some

of the most commonly used non-linear optical phenomena will be discussed later in this chapter.

With the understanding that the anharmonic terms are small compared to the harmonic ones, equation 2.1 can be solved by expressing x as a power series in $E(t)$. Equivalently, $P(t)$ can be generally expressed as a power series dependent on the strength of the applied electric field *E(t)* as

$$P(t) = \epsilon_0 \left[\chi^{(1)}E(t) + \chi^{(2)}E^2(t) + \chi^{(3)}E^3(t) + ...\right] \equiv P^{(1)}(t) + P^{(2)}(t) + P^{(3)}(t) + ... \tag{2.3}$$

where ϵ_0 is the permittivity of free space, $\chi^{(1)}$ represents the linear susceptibility tensor and $\chi^{(n)}$ represents the higher order non-linear susceptibilities to the n^{th} order. For simplicity, the tensor notation is left out. The assumption that the polarization *P(t)* depends on the instantaneous electric field *E(t)* also implies that the medium must be dispersionless and lossless. It must be noted that another important underlying assumption in expressing *P(t)* as a power series in *E(t)* as in Eq. 2.3 is that the strength of electric field *E(t)* is small compared to the field E_a (typically, $E_a \sim 3 \times 10^{10} Vm^{-1}$) holding the electrons and ions together [76].

From equation 2.3, the linear electric field dependence of the polarization is described by $P^{(1)}$, which oscillates at the optical frequency ω of the field. Examples of such linear processes in which no new frequencies are generated as a result of interaction with the field include linear absorption, light propagation, reflection, and refraction [75]. Spectroscopic methods which use linear optical material response include linear absorption or emission spectroscopies, typically expressed as a function of a single frequency axis.

Non-linear contributions to the polarization *P(t)*, described by the terms dependent on higher powers ($\geq$2) of the electric field *E(t)* in Eq. 2.3 lead to different non-linear optical phenomena. For example, if an electric field given by Eq. 2.2 is incident upon a material whose second-order non-linear susceptibility $\chi^{(2)}$ is non-zero, it leads to the generation of radiation that oscillates at the second-harmonic or twice the driving frequency at 2ω. This process, called second-harmonic generation (SHG), can be elucidated by substituting Eq. 2.2 in Eq. 2.3 to yield a polarization term $P^{(2)}(t)$ that contains a 2ω contribution. In addition, the polarization contains a zero-frequency component that represents the process of optical rectification, where a static electric field is generated across the non-linear crystal. Other non-linear processes such as sum-frequency generation (SFG) and difference frequency generation (DFG) can occur as a result of the interaction of a second-order non-linear material with field/(s) containing two distinct frequency components ω_1 and ω_2 according to

$$E(t) = E_1 e^{-i\omega_1 t} + E_2 e^{-i\omega_2 t} + c.c. \tag{2.4}$$

Substituting Eq. 2.4 in Eq. 2.3 yields a polarization $P^{(2)}(t)$ that contains contributions from the second-harmonic ($2\omega_1$ and $2\omega_2$), sum (ω_1+ω_1), and difference (ω_1-ω_1) frequencies of the input field. Typically, a phase-matching condition needs to be satisfied for any one of these frequency contributions to significantly contribute to the radiated electric field. Experimentally, this is achieved by proper selection of the polarization of the input electric fields and the orientation of the non-linear crystal. These non-linear light-matter interactions arising from $\chi^{(2)}$ have various applications. For example, SFG is used to produce tunable ultraviolet radiation by using a tunable visible laser and a fixed frequency visible laser as the two inputs. Similarly, DFG is used to generate tunable near-infrared light by choosing one of the inputs to be a tunable visible laser and the other to be a fixed-frequency visible laser [77]. Another interesting phenomenon arising from non-zero $\chi^{(2)}$ in materials is 'parametric ampli-

fication'. It occurs when a small signal electric field at frequency ω_1 is sent through a medium in the presence of a powerful pump electric field at frequency ω_2, resulting in the generation of an idler field at frequency ω_3= ω_2-ω_1. Energy conservation dictates that for every idler photon created, a photon at the pump frequency be destroyed and one at signal frequency be created, leading to the amplification of the signal field [77].

Second-order non-linear interactions such as the processes described above, are only possible in noncentrosymmetric media, i.e. media that do not possess a center of inversion. For materials that possess a center of inversion symmetry, the lowest order non-linear response is a third-order contribution to the polarization, and is described by a $\chi^{(3)}$ susceptibility [77].

2.1.2 Third-order polarization

Let us consider a more complete definition of an applied position and time-dependent field consisting of three frequency components ω_i, wave-vectors $\vec{k_i}$, and phase ϕ_i according to

$$E(\vec{r},t,\phi) = \sum_{i=1}^{3}(E_i(\vec{r},t)e^{-\iota(\omega_i t+\vec{k_i}.\vec{r}+\phi_i)}+c.c.) \equiv \mathbf{E_1}(\vec{r},t)+\mathbf{E_2}(\vec{r},t)+\mathbf{E_3}(\vec{r},t)+c.c. \quad (2.5)$$

where $\vec{r}$ is the spatial coordinate. The induced third-order polarization $P^{(3)}(t)$ will contain a total of 44 different frequency contributions [77]. Consequently, many effects arise from $P^{(3)}(t)$ such as the Kerr effect, self-focusing, and self-phase modulation. More examples include third-harmonic generation, leading to a signal oscillating at $\omega_1 + \omega_2 + \omega_3$, and four-wave mixing, with the signal oscillating at $\pm\omega_1 \pm \omega_2 \pm \omega_3$. 2DES relies on the four-wave mixing contributions resulting from one interaction with each of the fields $\mathbf{E_1}(\vec{r},t)$, $\mathbf{E_2}(\vec{r},t)$, and $\mathbf{E_3}(\vec{r},t)$. It must be pointed out that

the four-wave mixing signal is generated in a phase-matched direction according to $k_s = \pm\vec{k_1} \pm \vec{k_2} \pm \vec{k_3}$, which may or may not be the same direction as one of the incoming beams, depending on their geometry. Other spectroscopic techniques including hole-burning, pump-probe, two-photon absorption, photon-echo, transient grating and stimulated Raman are also related to $P^{(3)}(t)$ [77][75].

To understand 2DES, the third-order polarization $P^{(3)}(t)$ can be expressed as a non-linear impulse response dependent on the three interacting fields as

$$P^{(3)}(\vec{r},t) = \epsilon_0 \int_0^\infty dt_3 \int_0^\infty dt_2 \int_0^\infty dt_1 S^{(3)}(t_3,t_2,t_1) E(\vec{r},t-t_3) E(\vec{r},t-t_3-t_2) E(\vec{r},t-t_3-t_2-t_1) \tag{2.6}$$

where t_1, t_2, and t_3 are time intervals during which the system is allowed to evolve between interactions with the three different electric fields and $S^{(3)}$ is the third-order non-linear response function containing microscopic information about the system.

2.1.3 Non-linear response functions

In an optical spectroscopic measurement, the electronic and nuclear motions and relaxation processes show up through their effect on the polarization. Thus, the optical polarization provides a direct way to interpret any spectroscopic measurement. The position and time-dependent polarization $P(\vec{r},t)$ is given by the expectation value of the dipole operator $\hat{\mu}$, according to

$$P(\vec{r},t) \equiv \langle \hat{\mu}\hat{\rho}(t) \rangle \equiv Tr[\hat{\mu}\hat{\rho}(t)] \tag{2.7}$$

where $\hat{\mu} = \sum_\alpha q_\alpha(\vec{r} - \vec{r_\alpha})$ for all charges q_α at positions r_α and $\hat{\rho}$ is the density matrix.

It is clear from Eq. 2.7 that in order to understand the polarization $P(\vec{r},t)$, we

need to follow the evolution of the density matrix operator $\hat{\rho}$ during the course of a spectroscopic measurement. In order to do so, we take a semiclassical approach where we assume a classical electric field, but treat the material response quantum mechanically. We also assume that the electric field is weak enough to allow for us to perturbatively expand the material response in powers of the electric field. For the simplified case where a small particle can be represented as a point dipole interacting with the field, the evolution of the density matrix $\hat{\rho(t)}$ is described by the Liouville Von-Neuman equation [75]

$$\frac{d\hat{\rho}}{dt} = -\frac{i}{\hbar}[\hat{H}, \hat{\rho}] - \frac{i}{\hbar}[\hat{H}_{int}(t), \hat{\rho}] \tag{2.8}$$

where H is the unperturbed Hamiltonian of the system and $H_{int}(t)$ describes the time-dependent radiation-matter interaction according to $H_{int}(t) = -E(\vec{r}, t).\hat{\mu}$.
The density matrix can be approximated as a power series in the weak field $E(\vec{r}, t)$ according to

$$\hat{\rho}(t) = \hat{\rho}^{(0)}(t) + \hat{\rho}^{(1)}(t) + \hat{\rho}^{(2)}(t) + ... \tag{2.9}$$

where $\hat{\rho}^{(0)}(t) = \hat{\rho}^{eq}$ is the equilibrium density operator and $\hat{\rho}^{(n)}(t)$ contains the n^{th} order contribution in the electric field $E(\vec{r}, t)$. For a system undergoing n time-ordered interactions, $\hat{\rho}^{(n)}(t)$ is given by the general expression

$$\begin{aligned}\hat{\rho}^{(n)} = (\frac{i}{\hbar})^n \int_0^\infty dt_n \int_0^\infty dt_{n-1} ... \int_0^\infty dt_1 G(t_n) V G(t_{n-1}) V ... G(t_1) V \hat{\rho}^{eq} \\ \times E(\vec{r}, t - t_n) E(\vec{r}, t - t_n - t_{n-1}) ... E(\vec{r}, t - t_n - t_{n-1} ... - t_1)\end{aligned} \tag{2.10}$$

where $G(t)$ denotes the Liouville space Green function describing the evolution of the system in the durations between the field interactions and V represents a Liouville space operator given by $VA \equiv [V, A]$. The field-free expression in the right-hand side of Eq. 2.10 can be interpreted as sequential interactions of the system originally in

the state $\hat{\rho}^{eq}$ with the time-ordered fields, each followed by free evolution during a time interval t_n. Eq. 2.10 can be substituted in Eq. 2.7 to yield the expectation value of the induced polarization $P^{(n)}(\vec{r},t)$

$$P^{(n)} = \int_0^\infty dt_n \int_0^\infty dt_{n-1} ... \int_0^\infty dt_1 S^{(n)}(t_n, t_{n-1}, ..., t_1) \\ \times E(\vec{r}, t-t_n)E(\vec{r}, t-t_n-t_{n-1})...E(\vec{r}, t-t_n-t_{n-1}...-t_1) \tag{2.11}$$

where

$$S^{(n)}(t_n, t_{n-1}, ..., t_1) \equiv (\frac{i}{\hbar})^n \langle \hat{\mu} G(t_n) V G(t_{n-1}) V ... G(t_1) V \rho^{eq} \rangle \tag{2.12}$$

denotes the n^{th}-order non-linear response function carrying complete microscopic information needed for the calculation of optical measurements. By the principle of causality, the polarization $P^{(n)}(\vec{r},t)$ at a given time can only depend on the electric field at earlier times, implying that $S^{(n)}(t_n, t_{n-1}, ..., t_1) = 0$ if $t_i < 0$ where $i \in [1, n]$ [75].

It must be noted that the response function can be calculated by alternative methods, such as by evaluating the wavefunction (instead of the density operator) or using equations of motion in the Heisenberg picture [75] but this thesis will only focus on the density matrix approach.

We can obtain the third-order non-linear response function by putting n=3 in Eq.2.12

$$S^{(3)}(t_3, t_2, t_1) \equiv (\frac{i}{\hbar})^3 \langle \hat{\mu} G(t_3) V G(t_2) V G(t_1) V \hat{\rho}^{eq} \rangle \tag{2.13}$$

The presence of commutators from the definition of V in Eq. 2.10 implies that there will be 2 terms corresponding to each occurence of V, hence a total of 2^n terms contributing to the density matrix. Only half of the 2^n terms are unique and represent

what are called the Liouville pathways. For the third-order response, we get a total of 8 pathways, 4 of which are independent. The response function can be expressed as a sum of these pathways [78]

$$S^{(3)}(t_3,t_2,t_1) \equiv (\frac{i}{\hbar})^3 \theta(t_1)\theta(t_2)\theta(t_3) \sum_{i=1}^{4} [R_i(t_3,t_2,t_1) - R_i^*(t_3,t_2,t_1)] \tag{2.14}$$

where $\theta(t_n)$ is the Heavyside step function to ensure causality [$\theta(t) = 1$ for $t > 0$ and $\theta(t) = 0$ for $t < 0$] and

$$\begin{aligned}
R_1(t_3,t_2,t_1) &= \langle \hat{\mu}(t_1)\hat{\mu}(t_1+t_2)\hat{\mu}(t_1+t_2+t_3)\hat{\mu}(0)\hat{\rho}^{eq}\rangle \\
R_2(t_3,t_2,t_1) &= \langle \hat{\mu}(0)\hat{\mu}(t_1+t_2)\hat{\mu}(t_1+t_2+t_3)\hat{\mu}(t_1)\hat{\rho}^{eq}\rangle \\
R_3(t_3,t_2,t_1) &= \langle \hat{\mu}(0)\hat{\mu}(t_1)\hat{\mu}(t_1+t_2+t_3)\hat{\mu}(t_1+t_2)\hat{\rho}^{eq}\rangle \\
R_4(t_3,t_2,t_1) &= \langle \hat{\mu}(t_1+t_2+t_3)\hat{\mu}(t_1+t_2)\hat{\mu}(t_1)\hat{\mu}(0)\hat{\rho}^{eq}\rangle
\end{aligned} \tag{2.15}$$

where $R_i(i = 1-4)$ represent the four unique Liouiville pathways contributing to the third-order non-linear response function and $R_i^*(i = 1-4)$ are the corresponding complex conjugates of R_i [75, 78].

2.1.4 Double-sided Feynman diagrams

To understand the physical significance of the Liouville pathways described in the previous section (Eq. 2.15 for 3^{rd} order non-linear interactions), it is possible to adopt a graphical representation of the pathways. One such representation is the double-sided Feynman diagram representation which contains information about the evolution of the density matrix elements and provides knowledge of the time-ordering, frequency and the sign with which the different pathways contribute to the non-linear response function. Feynman diagrams are also useful to distinguish between coherence and population states in which the density matrix evolves during a given time interval. They enable easy understanding of the different pathway contributions to spectra and

can be understood with the following rules [75]:

1. Two vertical lines are used to represent the density operator. The left-hand side line represents the ket and the right-hand side represents the bra.

2. Time progresses from the bottom to the top of the diagram

3. Accounting for the minus sign each time an interaction V acts from the right in a commutator, the overall sign of a diagram is given by $(-1)^m$, where m is the number of interactions from the right side (bra).

4. Every interaction with the system is represented by a separate arrow and is labelled by a corresponding electric field parameter (frequency ω_i, wave-vector k_i, phase ϕ_i, depending on the relevance to the spectroscopic technique). The sign convention is such that each arrow pointing to the right (i.e. an incoming arrow on the ket side or an outgoing arrow on the bra side) represents a contribution of $E_i e^{\iota(-\omega_i t+\vec{k}_i.\vec{r}+\phi_i)}$ to the polarization while an arrow pointing to the left (i.e. an outgoing arrow on the ket side or an incoming arrow on the bra side) represents a contribution from $E_i e^{\iota(\omega_i t-\vec{k}_i.\vec{r}-\phi_i)}$. That is, the incoming arrows represent photon absorption while outgoing arrows represent photon emission.

5. The system evolves freely under the unperturbed system Hamiltonian H between interactions, and the density matrix element during that interval is explicitly written

6. The overall frequency or phase of the emitted signal (often depicted by a wavy arrow at the end) is given by the sum of all the frequencies or phases from the fields contributing with appropriate signs in the particular pathway.

To describe the third-order response (as probed using 2DES) using Feynman diagrams, we take three interacting fields $\mathbf{E_1}$, $\mathbf{E_2}$, and $\mathbf{E_3}$ each represented by their characteristic frequencies, wave vectors, and phases $(\omega_1, \vec{k_1}, \phi_1)$, $(\omega_2, \vec{k_2}, \phi_2)$, and $(\omega_3, \vec{k_3}, \phi_3)$

respectively. Performing a permutation over the time ordering of three fields according to 3!=6, a complete set of $(2^3) \times 6 = 48$ diagrams can be drawn. Therefore, for any given phase matching condition $\vec{k_s} = \pm\vec{k_1} \pm \vec{k_2} \pm \vec{k_3}$, only $2^3 = 8$ pathways remain. It can be generalized that for a given phase matching condition there are 2^n terms for an n^{th} order of polarization. It should also be noted that only half of these need to be considered since the other half are their complex conjugate, as can be seen from Equation 2.14. Fig. 2.1 shows the 8 representative double-sided Feynman diagrams corresponding to the independent Liouville pathways from the third-order non-linear response of any system containing three energy levels, $|g\rangle$, $|e\rangle$ and $|f\rangle$ representing the ground state, singly excited state and the doubly excited state respectively. The state $|f\rangle$ can be the two-exciton state of a molecular aggregate but also a higher existing state of a system like molecule or nanocrystal with energy about twice the energy of $|e\rangle$ that can be excited when $|e\rangle$ absorbs a photon. Only the rephasing contributions, given by the phase-matching condition $\vec{k}_s = -\vec{k}_1 + \vec{k}_2 + \vec{k}_3$, are shown here. Understanding the rephasing pathway is simple for a two-level system - the system evolves in conjugated coherences during the time intervals t_1 and t_3, that is, the phase acquired during t_1 reverses during t_3, explaining the name rephasing. The terms R_2 and R_3 in Eq. 2.15 correspond to rephasing pathways. Another type of pathway (not shown here) describes the evolution of the system in the same coherences during t_1 and t_3 and is called the non-rephasing pathway, corresponding to R_1 and R_4 in Eq. 2.15.

Not all of the pathways shown in Fig. 2.1 contribute significantly to the signal. Assuming that all the laser beams are in resonance with the material electronic transition frequency ω_{eg}, the resonant terms contribute significantly to the signal with a denominator $\sim (\omega_i - \omega_{eg})^{-1}$. These terms correspond to processes where photon absorption leads to excitation of the system and photon emission leads to de-excitation.

As can be seen from Fig. 2.1, 5 of the pathways violate this condition i.e. the system gets de-excited with photon absorption or excited with photon emission. This results in highly oscillatory off-resonant terms with a denominator $\sim (\omega_i + \omega_{eg})^{-1}$. Such off-resonant contributions are negligible and can be discarded under the rotating wave approximation (RWA) [79]. The three dominant pathways are highlighted in Fig. 2.1 with transparent blue boxes.

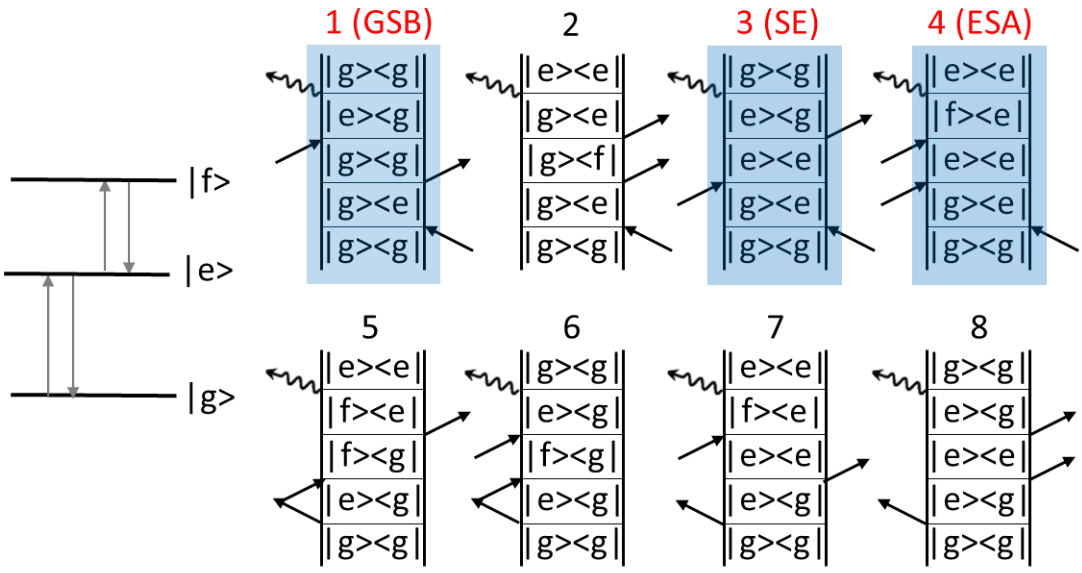

Figure 2.1: (Left) A model three level system containing three energy levels, $|g\rangle$, $|e\rangle$ and $|f\rangle$ representing the ground state, singly excited state and the doubly excited state respectively. The allowed transitions are shown with gray arrows. (Right) 8 representative Feynman diagrams for the three-level system corresponding to the rephasing signal from a 2DES experiment. The evolution of density matrix elements is shown with the progression of time from the bottom to the top. The arrows represent field interactions with the ket and bra on the left- and right- hand side respectively, exciting or de-exciting the system at each step. Diagrams that survive the rotating-wave approximation (RWA) are highlighted with blue boxes. Pathway 1, 3, and 4 correspond to ground-state bleach (GSB), stimulated emission (SE), and excited-state absorption (ESA) contributions respectively.

Depending on the sequence of interactions involved in the pathway corresponding to each Feynman diagram, its contribution can be differentiated into three relevant types of contributions [80]: ground state bleach (GSB), stimulated emission (SE), and excited state absorption (ESA), shown in Fig. 2.1. These pathways can be defined

using the nomenclature from pump-probe measurements, where a time-delayed probe interrogates the system after it has interacted with a pump pulse. GSB contributions result from depletion of the ground state population as a result of interaction with the pump pulses at the corresponding resonant frequencies. When interacting with a state already excited by the pump, an incoming probe photon may result in the emission of an additional photon from the excited state, corresponding to SE contributions. This effectively reduces the absorption at the excited frequency. Another possibility is the promotion into a higher excited state by the probe, leading to ESA pathways which result in an increased absorption at the frequencies corresponding to the energy difference between the lower ($|e\rangle$) and higher ($|f\rangle$) excited states.

2.2 Excitonic picture

To fully utilize double-sided Feynman diagrams for understanding energy transfer and interactions in a given system using spectroscopy, a knowledge of the energy level structure of the system is useful. In the study of molecular aggregates such as photosynthetic complexes, the excitonic picture is often employed. To illustrate this concept, we consider a simple dimer system of two molecules *1* and *2*, each consisting of a ground state $|g_i\rangle$ and an excited state $|e_i\rangle$, where $i = 1, 2$. Their transition frequencies are given by ω_1 and ω_2 respectively, with $\omega_2 \geq \omega_1$. A coupling J is assumed between the two molecules. The system Hamiltonian can be expressed using the molecular Hamiltonians along with the coupling Hamiltonian:

$$H_{sys} = \hbar\omega_1 |e_1\rangle \langle e_1| + \hbar\omega_2 |e_2\rangle \langle e_2| + J(\sigma_a^+ \sigma_b^- + h.c.) \tag{2.16}$$

where $\sigma_a^+ = |e_i\rangle \langle g_i|$ and $\sigma_a^- = |g_i\rangle \langle e_i|$. The eigenbasis of the individual molecules *1* and *2* is known as the *site* basis, whereas the eigenbasis of the total system Hamiltonian is known as the *exciton* basis [81]. After diagonalization, the Eq. 2.16 can be

written in the exciton basis as

$$H_{sys} = \hbar\omega_e \left|e\right\rangle \left\langle e\right| + \hbar\omega_{e'} \left|e'\right\rangle \left\langle e'\right| + \hbar\omega_f \left|f\right\rangle \left\langle f\right| \tag{2.17}$$

where $|e\rangle$ and $|e'\rangle$ are the single-exciton states whose energies are given by $\omega_{e,e'} = \omega_{av} \pm \Delta \sec(2\theta)$. Here, ω_{av} and Δ are the average and difference of the site energies respectively, $\omega_{av} = (\omega_1 + \omega_2)/2$ and $\Delta = (\omega_2 - \omega_1)/2$. θ is the mixing angle given by $\theta = \arctan(J/\hbar\Delta)/2$ [81]. Thus, coupling between the two molecules leads to a splitting of the molecular energy levels, given by $2\Delta \sec 2\theta$. The exciton basis is given by

$$\left|g\right\rangle = \left|g_1\right\rangle \left|g_2\right\rangle \tag{2.18}$$

$$\left|e\right\rangle = \cos\theta \left|e_1\right\rangle \left|g_2\right\rangle + sin\theta \left|g_1\right\rangle \left|e_2\right\rangle \tag{2.19}$$

$$\left|e'\right\rangle = -\sin\theta \left|e_1\right\rangle \left|g_2\right\rangle + cos\theta \left|g_1\right\rangle \left|e_2\right\rangle \tag{2.20}$$

$$\left|f\right\rangle = \left|e_1\right\rangle \left|e_2\right\rangle \tag{2.21}$$

It can be inferred from the above four expressions that it in the absence of coupling J, $\theta = 0$ and the wavefunctions in the excitonic picture can be written as product states. For example, $|e\rangle = |e_1\rangle |g_2\rangle$. That is, in case of weak coupling, either the site basis or excitonic basis can be used. But if the coupling is non-negligible, we must use the excitonic picture to describe a coupled system. The transition dipoles in the excitonic basis can be expressed in terms of the site basis transition dipoles as:

$$\mu_{eg} = \cos\theta\mu_1 + \sin\theta\mu_2 \tag{2.22}$$

$$\mu_{e'g} = -\sin\theta\mu_1 + \cos\theta\mu_2 \tag{2.23}$$

$$\mu_{fe} = \sin\theta\mu_1 + \cos\theta\mu_2 \tag{2.24}$$

$$\mu_{fe'} = \cos\theta\mu_1 - \sin\theta\mu_2 \tag{2.25}$$

An illustration of the *site* and *excitonic* basis representation is shown in Fig. 2.2

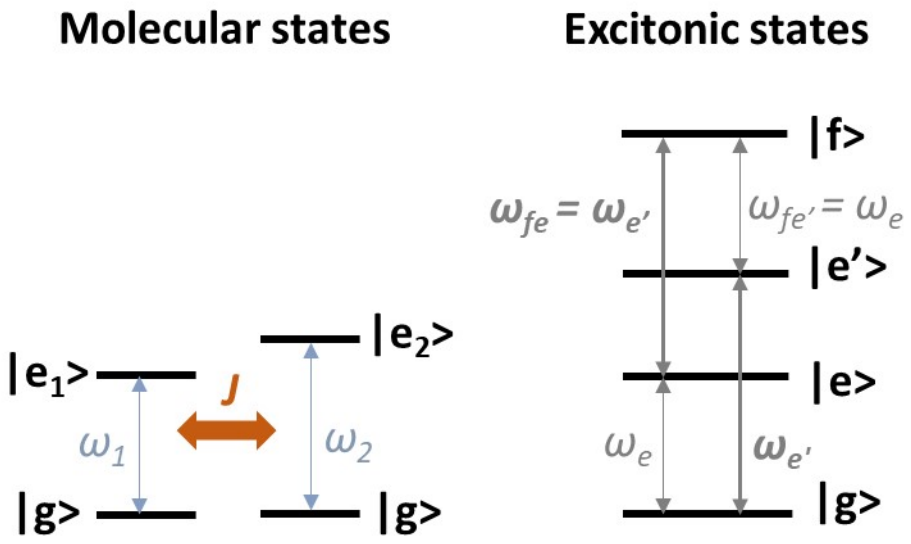

Figure 2.2: Energy level diagrams in the site (left) and excitonic (right) representation for a dimer system with a coupling J. In the excitonic picture, $|e\rangle$ and $|e'\rangle$ represent singly excited states and $|f\rangle$ represents the doubly excited state.

.

2.3 Two-dimensional electronic spectroscopy (2DES)

Most of the conventional linear spectroscopic techniques provide highly averaged information over space and time. To gain better insights into the structural properties and dynamics of complex molecules in condensed phases, a variety of two-dimensional (2D) nuclear magnetic resonance (NMR) techniques like NOESY (nuclear Overhauser enhancement spectroscopy) and COSY (correlation spectroscopy) were developed by early researchers [82, 83]. Later, the optical analog of 2D NMR utilizing ultrafast laser pulses in the infrared to UV-visible frequency ranges was developed [80]. It has since been utilized to study energy and charge transfer dynamics in photosynthetic light-harvesting complexes [58, 84, 85], coherences in multichromophoric sys-

tems [17, 86, 87], exciton dynamics in semiconductors [88–90], and photochemical processes [91, 92], among many more applications [93]. 2D spectroscopy is a better tool for understanding complex systems because it untangles overlapping signals in a single dimension by expressing them as a function of two frequencies, the excitation frequency and the detection frequency. A typical pulse sequence employed in a 2D measurement is shown in Fig. 2.3 (a).

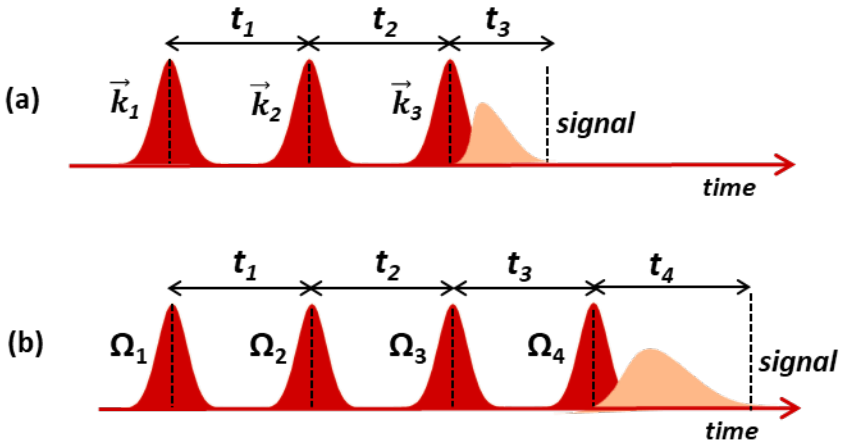

Figure 2.3: Pulse sequence used in (a) Coherently-detected 2DES: The time-delayed three pulses induce a third-order polarization generating a signal in a phase-matched direction according to the incoming wave-vectors $\vec{k}_{1,2,3}$ (b) Incoherently-detected 2DES: An all-collinear geometry is employed, resulting in a signal whose phase is modulated according to the acousto-optic frequencies $\Omega_{1,2,3,4}$. k_i and Ω_i are analogous in the two experiments for the purpose of defining signals of interest.

.

A large number of the implementations of 2D optical spectroscopy are based on 2D Fourier transform (2DFT) spectroscopy which is a direct optical analog of 2D Fourier NMR. Fourier transform spectroscopy in the optical domain was first demonstrated by Lepetit and Joffre [94] to calculate the second-order non-linear optical response of a KDP (Potassium dideuterium phosphate) crystral using a sequence of two time delayed ultrashort pulses. Later, the 2DFT implementation for electronic specteoscopy was demonstrated for the first time by Hybl at al [95]. 2DFT methodology offers a major advantage over pump-probe spectroscopic techniques by proving

both high temporal and spectral resolution. A typical pump-probe measurement employs a narrow band pump pulse with center frequency ω_{pump} to excite the sample. Then, a probe pulse, often broadband (ω_{probe}) and delayed by a time-interval t_2, probes the sample. The signal is recorded as a difference in the probe intensity with and without the pump. Thus, from a single experiment the pump-probe signal is given by $S_{pump}(\omega_{pump}, t_2, \omega_{probe})$, representing broadband detection after excitation at a single ω_{pump}. The limitation of pump-probe technique is that the time resolution depends on the duration of the pump pulse. A narrow band pump pulse is inherently long in the time domain, leading to a trade-off between time and frequency resolutions in case of pump-probe spectroscopy. This problem is circumvented by 2DFT spectroscopy, where two broadband pump pulses are used instead of a single narrow band pump. A time delay t_1 between the two pump pulses is introduced, and is scanned to resolve the excitation axis via a Fourier transform of the signal along t_1 [80]. In this case, the time resolution depends on the pump duration also, but the frequency resolution of the pump excitation axis is determined by the duration of t_1 scanned, and on the molecular system itself. Thus, decoupling the control over time and spectral resolution in 2DFT methods ensures that high temporal and spectral resolution can be simultaneously achieved, limited only by the signal-to-noise ratio (SNR) [96]. Furthermore, the real and imaginary parts of the non-linear signal can be separated using 2DFT, resulting in higher frequency resolution compared to when only the magnitude is measured [97].

In this thesis, we focus mainly on the visible and near IR region implementations of 2DFT spectroscopy, namely 2DES and its variants. 2DES is a valuable tool for probing electronic coupling, energy transfer, charge transfer, and relaxation processes [98]. Typically, a 2DES experiment employs a sequence of three pulses separated by three time delays t_1, t_2, and t_3 (see Fig. 2.3 (a). Time delay t_1 is often called

the coherence time, t_2 is referred to as the waiting or population time, and t_3 is the detection time. The coherent signal field $\mathbf{E}_s(t_1, t_2, t_3)$ emitted as a result of the induced third-order non-linear polarization $P^{(3)}$ is collected as a function of the three time delays. This signal can also be thought of as the scattering of the third pulse off the grating formed by the interference of the first two pulses in the sample [95]. A double Fourier transform of the signal with respect to the time delays t_1 and t_3 at a fixed t_2 yields a 2D spectrum $S_{2D}(\omega_1, t_2, \omega_3)$ which is a correlation map between two frequency axes: the excitation frequency ω_1 corresponding to t_1 and the detection frequency ω_3 corresponding to t_3. In some methodologies, the signal is collected directly in the frequency domain for the detection frequency ω_3 as $\mathbf{E}_s(t_1, t_2, \omega_3)$ and a Fourier transform along just the t_1 axis allows us to retrieve the 2D spectrum $S_{2D}(\omega_1, t_2, \omega_3)$.

2.3.1 Advantages of 2DES

Depending on where they appear on the 2D map, the signal peaks can be distinguished as diagonal peaks at $\omega_1 = \omega_3$ or cross peaks at $\omega_1 \neq \omega_3$ (Fig. 2.4 (a)). A t_2=0 spectrum provides useful information about the degrees of inhomogeneous and homogeneous broadening in a system (Fig. 2.4 (b)), through the ratio of the diagonal to antidiagonal widths of the diagonal peaks. In the context of photosynthetic systems, inhomogeneous broadening reflects the difference in pigment environments, and shows up as a distribution of site energies elongating the peaks along the diagonal. Homogeneous broadening, on the other hand, describes the faster time-scale fluctuations that affect the entire ensemble of pigments uniformly, rendering each molecule an intrinsic linewidth. At later waiting times, as the protein environment fluctuates, leading to changes in the pigment site energies, this process of spectral diffusion shows up in 2D spectral lineshapes as they become more round with increasing waiting time [79]. 2DES spectra also report on the electronic coupling through the presence of

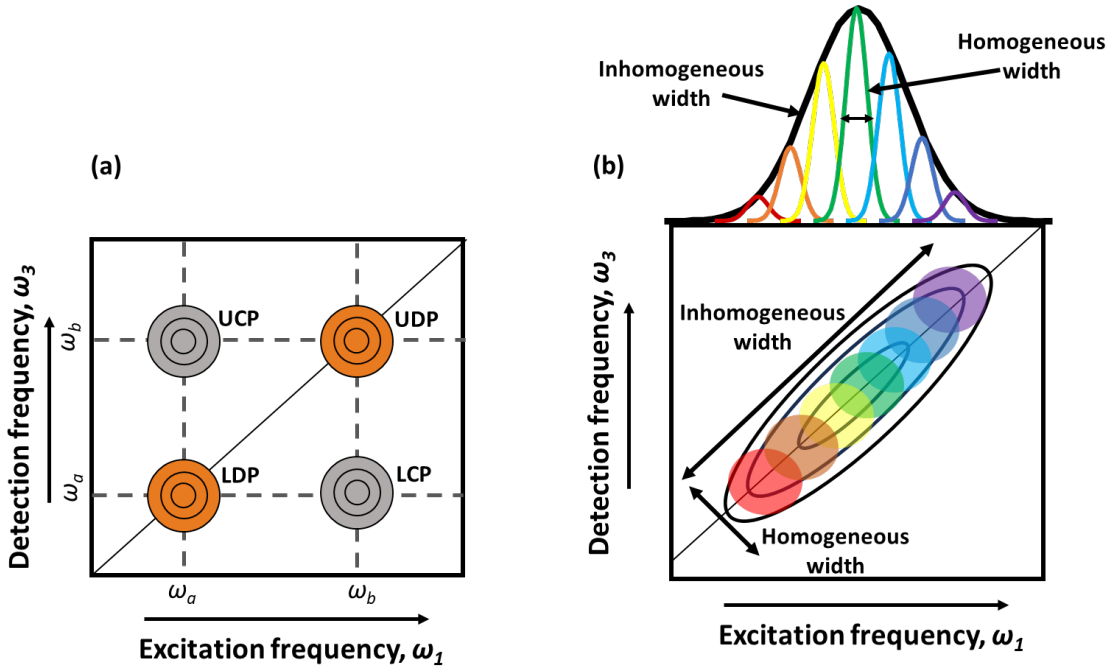

Figure 2.4: Cartoon 2D spectra highlighting the information accessed through 2DES. (a) Upper and lower diagonal peaks UDP and LDP at $\omega_1 = \omega_3$ for two different transitions in a system. Cross peaks LCP and UCP show up at $\omega_1 = \omega_3$. In the case of 2DES spectra, the presence of CPs at t_2=0 implies correlations between the entities corresponding to $\omega_{1,3}$ transitions. At longer t_2, CPs imply energy transfer. (b) Inhomogeneous and homogeneous linewidths can be distinguished at early t_2 times through diagonal and anti-diagonals peak widths respectively. At later times, as the molecules sample different site energies due to disorder, it causes the peaks to become more round (not shown here).

cross peaks at t_2=0, whereas the growth of cross peaks at later waiting times reflects energy transfer [96]. In addition, vibrational, vibronic, and electronic coherences are manifested by the oscillations of diagonal and cross peaks along the waiting time, and the participating states can be deduced in a variety of systems [17, 99, 100].

2.4 Implementations of 2DES

Implementing a 2DES experiment requires creating pulse sequences with variable, yet phase-stable time delays between pulses. Phase stability refers to the variation of the phase of one optical pulse relative to another for a specified time delay. For

a typical interferometer, mechanical instabilities lead to jitter in time delays on the order of the optical period. As a result, experiments employing shorter wavelengths are more susceptible to phase instabilities originating from fluctuations in path length and beam direction. An interferometric precision of $\sim \lambda/100$ is required to obtain a reliable Fourier transform frequencies from the scanned time delays, corresponding to a timing error of 0.026 fs at 800 nm [80]. Since many experiments require collection times of the order of minutes for a single 2D spectrum, mechanisms to ensure phase stability between excitation pulses and precise recording of time delays between them are crucial to 2DES measurements.

2.4.1 Non-collinear geometry

The first 2DES experiment was demonstrated by the Jonas group using a fully non-collinear geometry, where they employed a four-beam interferometer to generate the three excitation pulses, along with a tracer pulse. The additional tracer pulse enabled them to account for the time delay and phase shifts introduced by the post sample optics, in addition to the mechanical instabilities in the interferometers. The time delays between excitation beams were measured to ± 0.04 fs using spectral interference of replica excitation beams at each point where the signal was collected, making the measurement insensitive to mechanical errors in the stage movement as well as vibrations on the table [80]. In Chapter VI, we show a method of precisely tracking the time delays by collecting time-domain interference signals.

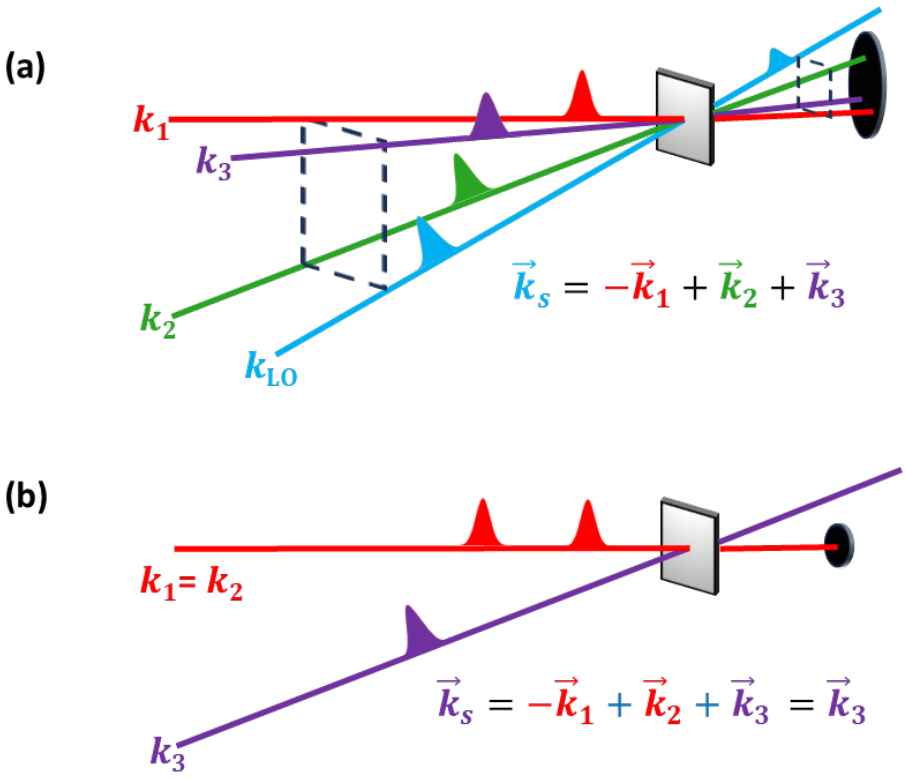

Figure 2.5: (a) Fully non-collinear and (b) pump-probe implementations of 2DES. The signal generated in a phase-matched direction according to $\vec{k}_s = -\vec{k}_1 + \vec{k}_2 + \vec{k}_3$ is collected in a different direction as the incoming beams for the fully non-collinear case. In case of the pump-probe geometry, the signal is emitted in the same direction as the probe and is not backhground-free.

In the non-collinear geometry the signal generated as a result of the three interacting fields $\mathbf{E_1}$, $\mathbf{E_2}$, and $\mathbf{E_3}$, represented by wave vectors $\vec{k}_1$, $\vec{k}_2$, and $\vec{k}_3$ respectively is collected in a phase-matched direction according to $\vec{k}_R = -\vec{k}_1 + \vec{k}_2 + \vec{k}_3$ and $\vec{k}_{NR} = +\vec{k}_1 - \vec{k}_2 + \vec{k}_3$ for the rephasing and non-rephasing signals respectively. When a fully non-collinear geometry is used (see Fig. 2.5 (a)), the four-wave mixing signal is generated in a different direction from the incoming fields. This enables background free collection, ensuring elimination of noise from excitation beams as well as prevention of detector saturation effects from intense excitation beams. The amplitude and phase of this signal is often heterodyne-detected by the use of a well-defined local oscillator field propagating in the direction of the signal, enabling complete retrieval of

the complex time-resolved non-linear polarization. The rephasing and non-rephasing signals generated in the directions defined by $\vec{k}_R$ and $\vec{k}_{NR}$ are summed to yield the absorptive 2D spectrum, free from broadening refractive contributions. 2D spectra can also be collected in the pump-probe geometry, where the two pump pulses are collinear (i.e. $\vec{k}_1 = \vec{k}_2$) and the probe is crossed with the pumps at a small angle (as shown in Fig. 2.5). Thus, the rephasing and non-rephasing signals are both generated in the same direction as the probe beam, which also serves as the local oscillator field [101–104]. Phase-cycling approaches are required to correctly isolate the rephasing and non-rephasing signals in the pump-probe geometry [104, 105].

To maintain phase stability in 2DES experiments, active interferometric stabilization metholodogy based on feedback electronics has been implemented [97, 106]. In the near IR wavelength region, relative phase fluctuations between excitation pulses were suppressed to under 0.01π, while the error in the reference phase was reduced to less than 0.1π during data collection [97]. In addition, passive phase-stabilization techniques, requiring only optical elements, have been used because of ease of implementation and control. For example, diffractive-optics have been used to generate fully non-collinear pulses with common optics, thus making them inherently phase-stable. To control the time delays for 2D measurements, refractive delays using rotating cover slides [107, 108] or the translation of wedges [109, 110] were used. Other approaches using beam splitters [111–113] or pulse-shapers [114–116] to achieve passive phase stabilization have also been demonstrated.

Non-collinear 2DES approaches are limited by the smallest sample size that they can study because a sample volume greater than λ^3, the cube volume of the excitation wavelength, is required for the coherent build up of a macroscopic polarization signal [117], limiting their capability to study smaller ensembles of molecules. Moreover,

since non-collinear pulses are difficult to combine with a microscope, spatially resolved spectroscopic measurements of inhomogeneous samples of interest, such as growth condition-dependent purple bacterial light harvesting complexes[2] or semiconductor samples with defects [118, 119] is challenging. Such structural inhomogeneities in the samples are known to affect the excited state dynamics and warrant detailed studies. Fully collinear implementations of 2DES offer the ability to be coupled with microscopy, enabling a way to correlate structural and energetic inhomogeneities [70].

2.4.2 Fully collinear geometry

The first demonstration of a fully collinear geometry in the optical domain was done by Wagner et al, where they used carrier-envelope phase modulation with an acousto-optic (AO) pulse shaper for the generation of a sequence of three collinear femtosecond pulses. In addition to recording the 2D photon-echo signal of rubidium vapor in transmission mode, they used four pulse-system interactions to retrieve the 2D spectrum in fluorescence mode [117]. The addition of the fourth pulse interaction projects the third-order polarization onto a fourth-order excited-state population. A typical pulse sequence employed in the fully collinear experiments is shown in Fig. 2.3 (b). Owing to the fourth pulse, the resulting observable is an incoherent signal proportional to the excited-state population [120, 121], and is collected as an action-spectrum through different detection modes such as fluorescence [70, 122], photocurrent [123, 124], photoions [125], or photoelectrons [126] emission. With the ability to study ultrafast system dynamics with the help of a measurable property such as photoluminescence or photocurrent generation, these techniques make a powerful tool to examine devices in *operando* conditions [127]. Action-detected spectroscopy has been used to study a wide variety of interesting systems such as photosynthetic systems [70, 122], atomic vapors [74, 128], molecular dimers [72, 129], dyads [130], quantum dots [131], as well as organic [124, 132] and perovskite [133] solar cells.

The nature of the signals originating from the population state can be understood by considering the interacting electric field $E(t)$ which consists of a sequence of four optical pulses given by

$$E(t) = \sum_{i=1}^{4} E_i(t + t_i)e^{-\iota(\omega_i t + \vec{k_i}.\vec{r} + \phi_i)} \tag{2.26}$$

After each successive interaction of the system with the field given by Eq. 2.26, the resulting non-linear optical signals acquire the phase terms $e^{\pm\iota\vec{k_i}.\vec{r}}$ and $e^{\pm\iota\phi_i}$. In a completely non-collinear geometry used in conventional three-pulse coherent measurements (described in the previous section) the signal acquires a net phase-matched direction $\vec{k_{sig}}$, given by $\vec{k_R}$ and $\vec{k_{NR}}$ for rephasing and non-rephasing signals respectively. In the collinear geometry, however, the signal is generated in the same direction $\vec{k}$ as the incoming pulses, and hence a background free detection based on phase-matching is not possible in such cases. However, the generated non-linear signal varies with different combinations of the phase terms ϕ_i. These non-linear signals with their distinct phase-dependence can be isolated using alternative approaches such as phase-cycling [117, 134–137], and phase-modulation [70, 74, 122, 130, 138, 139]. Analogous to the $\vec{k}$ dependence in case of phase-matching, the phase-dependence of the rephasing and non-rephasing signals is given by $\phi_R = -\phi_1 + \phi_2 + \phi_3 - \phi_4$ and $\phi_{NR} = \phi_1 - \phi_2 + \phi_3 - \phi_4$ respectively.

As stated above, the four-pulse collinear measurements do not rely on a 'spectral grating' of dipole oscillators to emit a coherent signal in a phase-matched direction enabling to study samples smaller in size than λ^3. The ability of action-detected spectroscopic techniques to be combined with microscopy [70] or single molecule detection [140] makes them particularly attractive compared to the coherently-detected techniques. Another advantage of action-detected methods is that they are free from

the non-resonant response from the solvent which dominates the signal during pulse overlap and at short waiting times in coherent experiments [141].

2.5 Fluorescence-detected two-dimensional electronic spectroscopy (F-2DES)

The work reported in this thesis focuses on action-detected, and more specifically, fluorescence-detected 2DES. The ease of implementation, and the advantages (discussed in the previous section) offered by this method make it a promising technique for single-molecule spectroscopy and imaging. Different implementations of the F-2DES technique are discussed in the following sections. It must be pointed out that our understanding of the signatures of F-2DES spectra is rather limited compared to its coherently-detected counterpart. Evident differences in the appearance of the spectra obtained from coherently-detected 2DES and F-2DES arise from the fourth pulse interaction which gives rise to additional Liouville pathways in the latter case. Moreover, the excited state population lives orders of magnitude longer than the coherent signal that is detected in coherent experiments, making the method sensitive to processes that occur during the to detection time t_4 (refer to Fig. 2.3) dynamics (discussed in Section 2.7). As demonstrated in Chapters IV and V of this thesis, these factors limit the ability of F-2DES to resolve excited state dynamics in some systems.

2.6 2DES and F-2DES: Complementary but not the same

Even though coherently-detected 2DES (C-2DES) and F-2DES are analogous techniques for elucidating ultrafast dynamics in two dimensions, the measured spectra from the two exhibit clear differences. Recently, there has been an increased interest in the discussion pertaining to the interpretation and origin of the action-

detected spectra [141–146], and the non-trivial contrast in information obtained from C-2DES spectra [71]. Studies comparing the spectra using both coherently and incoherently detected measurements to elucidate the complementary data have been reported [129, 147, 148].

The significant difference between C-2DES and F-2DES arises due to the fourth pulse involved in excitation. This interaction performs the role of generating an excited-state population, leading to an additional signal-generating Liouville pathway [71, 141] as shown in Figure 2.9. In addition to the GSB, SE, and ESA pathways which contribute a negative signal to the spectra, another ESA pathway with population ending in a doubly excited state contributes a positive singal. This doubly excited state may represent a two-exciton state such as in a molecular aggregate or a higher excited state of a system like a molecule or nanocrystal. Typically, the number of relaxation pathways available to the doubly excited state is much larger compared to those available to the singly excited states. Depending on the quantum yield of this pathway (referred to as ESAII) relative to the ESA pathway originating from a singly excited state (referrred to as ESAI), these signals cancel to different degrees, thus changing the appearance of the spectra. In a system with weakly coupled chromophores, such as the B800 and B850 rings in LH2, the ESAII pathway only contributes to cross peaks (Fig. 2.9). Hence, the contrast in the amplitude of cross peaks is more pronounced in case of F-2DES relative to C-2DES. Complete ESA signal cancellation in F-2DES can reveal "clean" GB and SE cross peaks, allowing for a more quantitative study of exciton delocalization and correlation effects. However, it has been noted that the cross peak dynamics can be nontrivial [142].

The delay in detection of incoherent signal (>ns compared to ∼ps for the coherent signal), during which the excited-state population can be affected by several processes,

accounts for an additional dynamic variable in action-detected 2DES. Second-order decay processes such bimolecular recombination, exciton-exciton annihilation (EEA), Auger recombination, and photocarrier scattering can occur in addition to the first-order decay processes, especially in condensed-matter systems [149]. The appearance of cross peaks in F-2DES at early waiting times is attributed to these processes [73, 141] and not necessarily to excitonic delocalization [71, 122], unlike in the C-2DES spectra. Using F-2DES, strong cross peaks at early waiting times have been reported for purple bacterial LH2 [70, 122], in contrast to the observations in C-2DES studies with weak to no cross peak presence [16, 60]. Additionally, the unwanted incoherent mixing of linear responses, originating from non-linear population dynamics such as EEA, Auger recombination, or non-linearities in the detection can occur, contaminating the non-linear signal and hiding spectral dynamics [143, 145, 149, 150].

2.7 Detection time dynamics: Exciton-exciton annihilation, incoherent mixing

It was realized early that dynamics during the detection time can affect the spectral features and hence the information contained in the F-2DES spectra [138]. In multichromophoric systems, the number of excitons created can be more than one but fewer excitons are detected as a result of EEA. EEA is described as a two-step process which is possible when two molecules are simultaneously excited. When the excitons meet, a higher excited state is generated on one molecule leaving the other in the ground state. Rapid internal conversion then brings the excited molecule back to the first excited state, effectively causing the net loss of one exciton [141, 145, 151]. A depiction of the EEA process for a dimer of two three-level molecules (shown in site basis) is given in Fig. 2.6 (Figure is adapted from [73]). Another possibility of the EEA process is the annihilation of both excitons. The cross peaks appearing at early

waiting times in F-2DES may be a result of cancellation of the two ESA pathways (ESAI and ESAII) due to EEA effects [71, 73]. By simulating the F-2DES spectra of multichromophoric LH2 of purple bacteria, Kunsel et al. [71] showed that as long as pathways are present for excitons to annhilate, cross peaks may be present even in case of weak coupling between the chromophores. This contrasts strongly with C-2DES, where the presence of cross peaks at $t_2 = 0$ indicates excitonic coupling. In case of perfect EEA, the two ESA pathways fully cancel out, rendering the spectra ESA-free [122, 142].

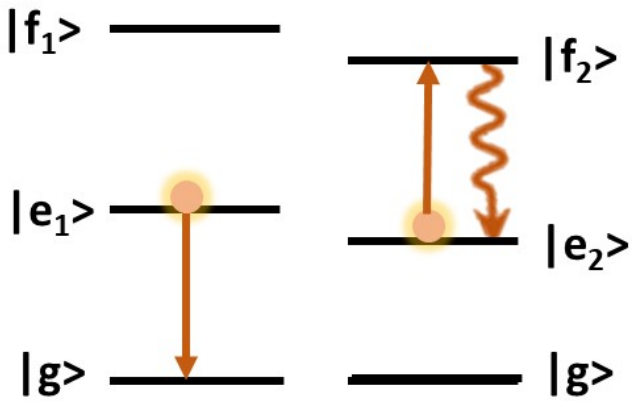

Figure 2.6: A dimer of two three-level molecules, showing exciton-exciton annihilation in the site basis. In the first step of annihilation, one of the molecules is excited to the higher excited state (shown as $|f_2\rangle$ while the other one de-excites from $|e_1\rangle$ to the ground state. The higher excited state molecule then rapidly relaxes by internal conversion to the first excited state ($|e_2\rangle$).

To understand some features of the cross peaks in F-2DES and C-2DES and the effect of EEA in F-2DES, we show the rephasing Feynman diagrams (2.7), corresponding to the lower cross peak (excitation at $\omega_{e'}$ and detection at ω_e) for the dimer system energy level diagram described in Section 2.2.

From Fig. 2.7, we can see that in case of C-2DES, GSB and ESA I (ending in singly excited state $|e'\rangle$ pathways contribute with opposite signs according to $(-1)^m$,

where m is the number of interactions on the bra side. When the molecules are weakly coupled (or independent), site basis treatment of the states and transition dipoles is permissible. This leads to the cancellation of pathways and no cross peak is observed. However, if the coupling is stronger, the transition dipoles are transformed according to Eq. 2.22-2.25 and the weights of the GSB and ESAI pathways no longer remain the same, leading to imperfect mutual cancellation and causing the appearance of cross peaks at early times. In fact, the cross peak amplitude is proportional to J/Δ [73].

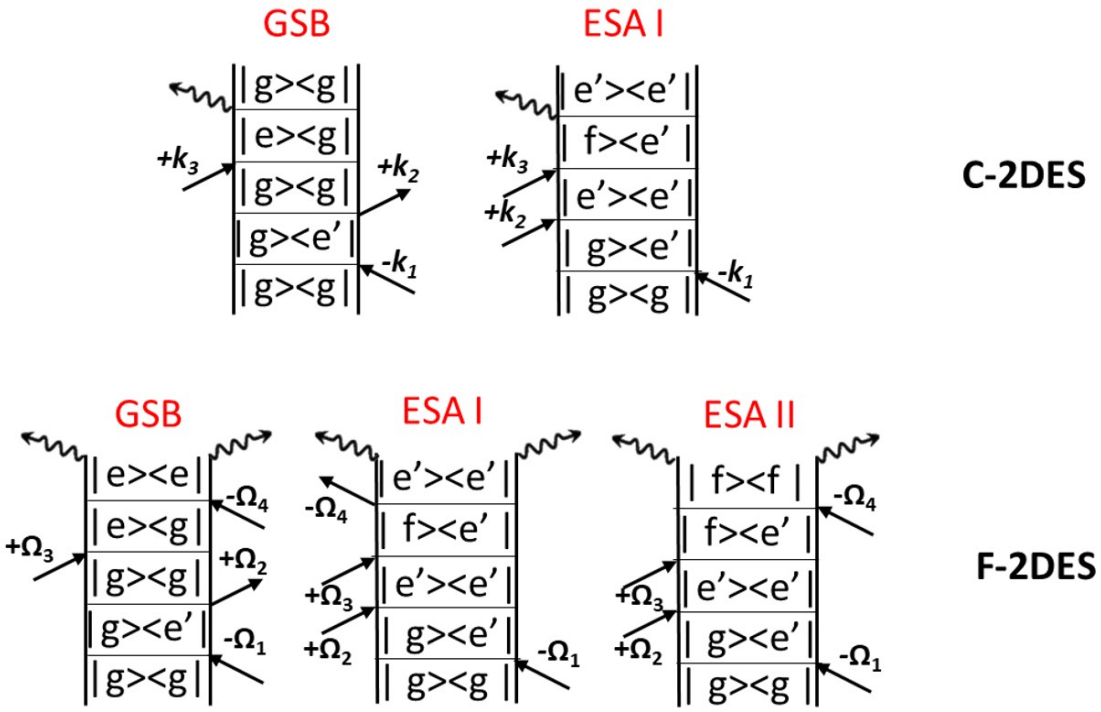

Figure 2.7: Double-sided Feynman diagrams corresponding to rephasing contributions to the the lower cross peak for C-2DES and F-2DES. The dimer model shown in Fig. 2.2 is considered.

In case of F-2DES, three contributing pathways are present - GSB, ESAI, and ESAII, which contributes with an opposite sign to the first two. The weight of the ESAII pathway is determined by the quantum yield of this pathway relative to ESAI pathway. In case of independent molecules (no coupling or energy transfer),

the ESAII pathway contributes two photons, leading to the cross peak cancellation. This is similar to the behaviour in C-2DES, and is basically the case of when no annihilation occurs. Now, let us consider the situation when the molecules are weakly coupled. This would be the case when energy transfer happens, but there is no delocalization. Two possibilities are considered. If the signal emission or detection occurs before annihilation takes place, the relative ESAII pathway contribution is lower than two photons when the two molecules have different oscillator strengths, leading to imperfect cancellation and appearance of a cross peak. On the other hand, for molecules with similar oscillator strength, the cross peak disappears [73]. If annihilation does take place, the ESAII pathway contribution is again lower and cross peaks appear. A factor $\Gamma \in [1, 2]$ can be used to account for the yield of the ESAII pathway, or equivalently, the amount of annihilation happening in a system [72], such that the F-2DES spectrum signal can be expressed as:

$$S \propto -\mathrm{GSB} - \mathrm{SE} + (\Gamma - 1)\mathrm{ESA} \tag{2.27}$$

$\Gamma = 2$ corresponds to the case of no annihilation, and the signal is the same as C-2DES (amplitude given by $S \propto \mathrm{GSB} + \mathrm{SE} - \mathrm{ESA}$). When $\Gamma = 1$ (perfect annihilation), only the GSB pathway contributes, and cross peaks appear. This is interesting, since the cross peaks appear even in the case of independent molecules as long as the two excitons annihilate and one photon is contributed from ESAII. In case of strong coupling, delocalization and annihilation collectively contriubute to the cross peaks.

Incoherent mixing, on the other hand, can hide spectral features corresponding to the non-linear coherent response [150] and special care needs to be taken in order to avoid such effects in F-2DES measurements. Incoherent mixing occurs when excited-state populations produced by each pair of the four-pulse sequence are correlated in

a measurement. The phase-signature of such signals, which involve two linear signals that become correlated during the detection time, is the same as the signal stemming from four-light matter interactions. Bargigia et al [149] have pointed out that frequency dependent impedance and interface-parasitic capacitance can make unoptimized devices highly non-linear in nature. Thus, the mixing of non-linear signals can be due to not just the material under study but also the device architecture and electronics. In cases where some such contributions are experimentally unavoidable, a quantified distinction of incoherent mixing contributions from true non-linear signals is necessary [143, 149].

In a recent work, Bruschi et al. [145] reported an interesting result for a system with weakly interacting units, stating that the origin of cross peaks at early waiting times can be equivalently attributed to incoherent mixing as well as EEA due to detection time dynamics. In another work by the same group [124], they focused on identifying the origin of incoherent mixing in weakly coupled multichromophoric systems. Using a probabilistic approach to describe the light-matter interactions, they determined that the cross peaks resulting from incoherent mixing are dominated by GSB over the SE contributions. They also suggested that in addition to direct interactions such as EEA and Auger recombination, *indirect* interactions may also contribute to incoherent mixing. Analogous to the treatment of contributions in C-2DES [152], they distinguished the GSB, SE, and ESA contributions into self-population (resulting from interactions of all four laser pulses with the same chromophore) and cross-population (resulting from interactions of different pulse pairs with different chromophores) pathways and highlighted that information about energy transfer dynamics is contained only in the self-population SE contributions. These contributions are often dominated by the cross-population contributions in systems with a large number of chromophores, leading to difficulties in the identification of energy transfer

dynamics contained in SE along the waiting time t_2. Double-sided Feynman diagrams for the GSB, SE, ESAI and ESAII pathways classified as self- and cross- pathways are shown for dimer system shown in Fig. 2.8 (adapted from [6]) in the weak coupling limit. In the case of no annhilation, only GSB and SE self-population pathways contribute to the spectrum. But the situation changes when $\Gamma \neq 2$. For example, in the case of efficient annihilation ($\Gamma = 1$), ESAI and ESAII cross-population pathways cancel, leaving the GSB cross-population pathways adding up to the GSB self- and SE self-population pathways. In such cases, the GSB cross-population pathway is analogous to the phenomenon of incoherent mixing [150][6]. That is, the source of incoherent mixing in this case are the cross-population pathways.

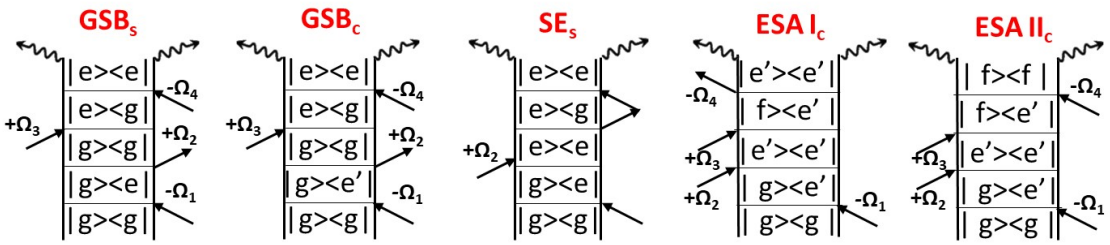

Figure 2.8: GSB, SE, ESAI, and ESAII rephasing pathways, classified into self- and cross-population pathways, if all four pulses interact with the same molecule (self-population pathways, subscript "s") or if each pulse pair interacts with different molecules (cross-population pathways, subscript "c"). $|e\rangle$ and $|e'\rangle$ represent the first-excited states of the two different molecules. Figure adapted from [6].

2.8 Appendix

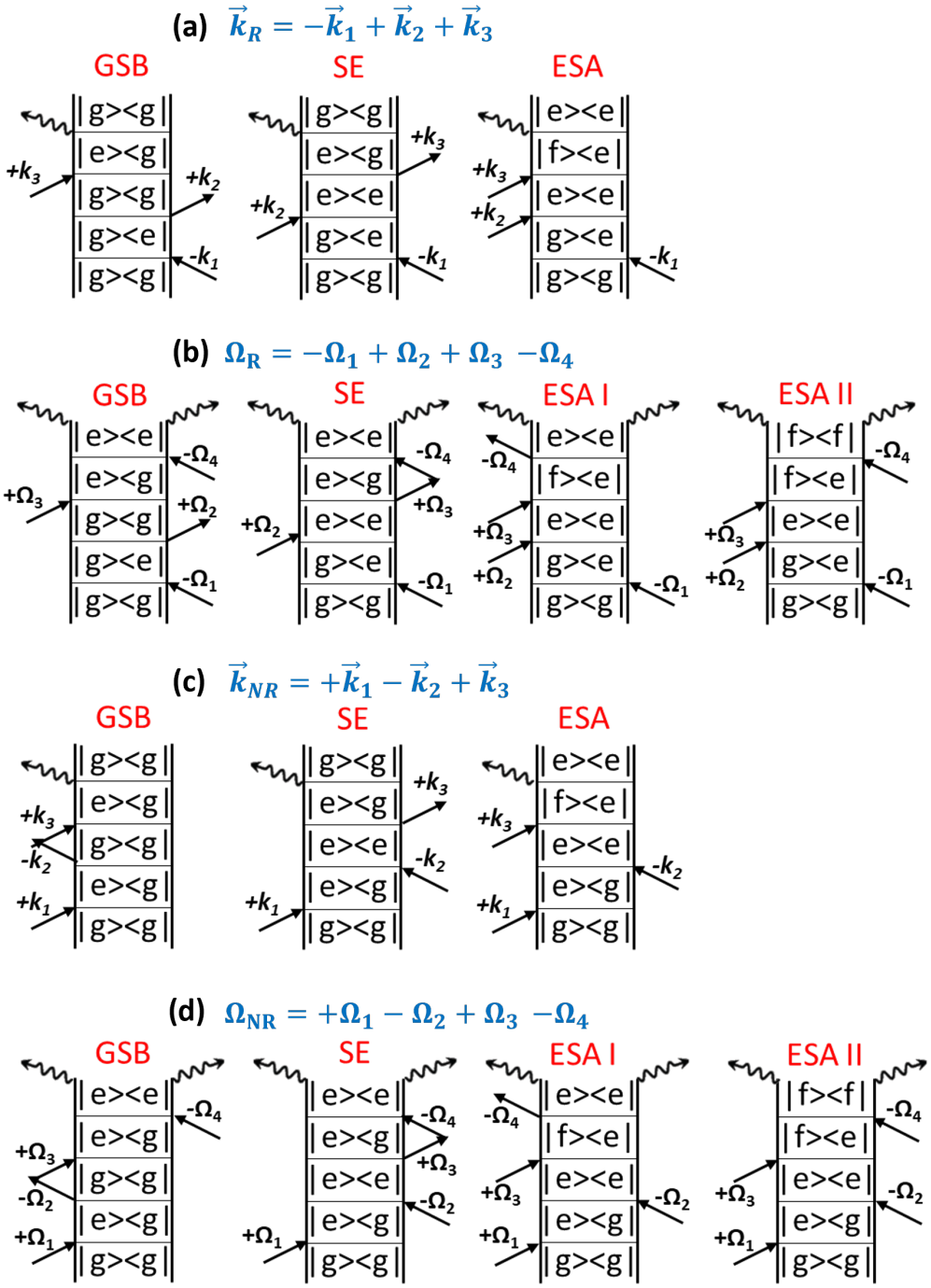

Figure 2.9: Double-sided Feynman diagrams for the rephasing and non-rephasing contributions in C-2DES ((a) and (c)) and F-2DES ((b) and (d)) experiments. Diagrams drawn for the model system shown in Fig. 2.1 are shown. Each pathway contributes with a sign given by $(-1)^m$, where m is the number of interactions on the bra side. Thus, in case of C-2DES, the ESA pathway contributes with a negative sign

and the GSB and SE pathways contribute with a positive sign. In case of F-2DES experiments, the additional interaction due to a fourth pulse gives rise to an ESA II pathway, corresponding to emission from the second-excited state $|f\rangle$. ESA II contributes with an opposite sign to the ESA I pathway. Partial or complete cancellation of the two ESA pathways in F-2DES results in different looking spectra as compared to C-2DES.

CHAPTER III

Fluorescence-Detected Two-Dimensional Electronic Spectroscopy (F-2DES)

This chapter discusses the experimental implementations of F-2DES using phase-cycling and phase-modulation. The experiments reported in Chapters IV and V are conducted with the help of a lock-in detected phase-modulation based F-2DES setup, which is detailed in this chapter. Using the capabilities of the lock-in, we perform phase-sensitive detection with respect to a reference signal. The reference signal enables physical undersampling of the signal, allowing for longer time steps during the scan. The signal is filtered against a large background, minimizing white noise. In addition, lock-in detection minimizes $1/f$ noise from laser and mechanical vibrations by effectively placing a narrow bandpass filter around the modulation frequency at which the signal oscillates. We also report detector non-linearity tests that we performed prior to our experiments as a way to make sure that the detector responds linearly to the input intensity. We also checked our spectra for incoherent mixing contributions that could arise from detector and other electronic non-linearities using a methodology described by Bargigia et al [149].

3.1 Implementations of F-2DES

3.1.1 Phase-cycling based approaches

Controlling the interpulse phases in order to extract the desired signal forms the basis of the phase-cycling procedure. In phase-cycling, we repeat an experiment using pulses with multiple career-envelope phase (ϕ_i) combinations for each time delays. A careful linear combination of the phase dependent data is then used to extract the optical signal of interest [93, 153]. The theory of phase-cycling in optical spectroscopy was first introduced by Keusters et al [154], where they pointed out the analogy between directional phase-matching and phase-selective phase-cycling procedures and proposed a 16 step phase-cycling procedure to yield a two-pulse 2D photon-echo optical spectrum. They later demonstrated the procedure using a grating based AO pulse shaper by acquiring the 2D optical spectra of rubidium vapor in fluorescence and transmission mode [117, 134]. A benefit of employing an AO pulse shaper, as highlighted by Wagner et al [117] is that its rapid update rate can be exploited to form a sequence of pulses separated by arbitrary delays with required phase combinations with each shot. With no limitations on the electronics, this means that unqiue data points can be collected at a repetition rate of 100 kHz [117]. More recently, F-2DES was demonstrated using a 27 step phase-cycling approach for isolating the nonlinear signal [129, 135–137]. Each of the 27 phase cycles were performed by either an AO pulse-shaper (Dazzler, Fastlite) [129, 136], or a spatial light modulator (SLM) based pulse shaper [135, 137]. AO pulse shaping using Dazzler (Fastlite) has been achieved at a repetition rate of up to 1 KHz [155]. However, the maximum delay is limited by the time delay window of the pulse shaper. In a recent work by our group [156], the rephasing and non-rephasing signals in a broadband detected F-2DES were separated using a mixed AO pulse-shaping and frequency filtering scheme. In SLM phase-cycling, the refresh time (or the maximum repetetion rate) for the waveforms

is of the order of a few milliseconds, which can lead to extended data acquisition times, making the measurements more susceptible to laser noise and increased sample photobleaching.

3.1.2 Phase-modulation based approaches

Tekavec et al [74] proposed the first phase-modulation based implementation of F-2DES as an alternative to the phase-clycling approaches. Previously, they had studied a first-order process using a phase-related collinear optical pulse pair and demonstrated quantum state reconstruction of atomic Rubidium vapor [69]. Their experiment used the phase-modulation approach and synchronous lock-in detection with respect to an appropriately constructed reference oscillating at the signal frequency. As highlighted in the previous sections, the pulse electric field oscillates on sub-fs time scales and as a result, small fluctuations of the temporal envelope can lead to significant errors in the signal phase, necessitating the need for active or passive phase-stabilization techniques. In their work, Tekavec et al showed that phase-modulation effectively decouples the time delay of an optical pulse pair from its relative phase [69, 74]. Phase-modulation of the pulses is achieved by imparting a distinct career-envelope phase to each pulse using AO modulators (also called Bragg cells) operating in the Bragg regime [157, 158]. The use of AO modulators enables operations at high repetition rates ($\sim$ tens of MHz) [70]. The excited-state population created by the phase-modulated pulse pairs contains interference contributions that modulate at different linear combinations of the AO frequencies imparted on the excitation pulses [69]. The modulated population gives rise to a time-varying incoherent signal, which can be detected using phase-selective detection schemes to learn about the excited state properties of systems. This has formed the basis of phase-modulated action-detected [123–126], and in particular, F-2DES studies [70, 122, 130]. In this thesis, We will be reporting F-2DES measurements with the aim to better under-

stand the potential applications of action-detected 2DES for investigating dynamics in multichromophoric systems.

The ease of implementating F-2DES in an all-collinear geometry, as mentioned before, offers a particular advantage in that it can be readily combined with a microscope for imaging purposes. Using the phase-modulation and lock-in detection [74] pioneered by Tekavec et al, our group performed a spatially resolved F-2DES study of purple photosynthetic bacteria [70]. We studied spatially inhomogeneous mixtures of low-light and high-light grown whole cells as well as LH2 complexes from *Rhodopseudomonas palustris* and identified the low- and high-light character of the 2D spectra from different spatial locations on the sample. In another work from our group, energy transfer dynamics in a strongly coupled bacteriochlorin dyad were reported using the phase-modulated F-2DES approach [130]. A coherence map analysis revealed that the main frequency observed is consistent with a vibrational frequency in bacteriochlorin monomers, and no frequency signatures corresponding to the excited state electronic energy gap were observed. This thesis builds upon the work described in the two aforementioned papers [70, 130]. We explore the system dependence in influencing kinetics revealed through F-2DES and compare the results with coherently-detected 2DES. We report on an implementation to improve the signal-to-noise and acquisition times, in addition to proposing a broadband detection scheme for F-2DES.

3.2 Phase-modulation based F-2DES experiment

The experimental setup used for the F-2DES measurements discussed in Chapters IV and V of this thesis is based on the acousto-optic phase modulation and lock-in detection scheme demonstrated first by Tekavec at al [74]. Acousto-optic modulation enables the use of high modulation frequencies. The resulting signals, modulated at different linear combinations of the high frequencies, help to minimize $1/f$ noise in

the measurements. Lock-in detection provides the advantage of high sensitivity over a wide dynamic range and minimizes white noise by enabling the selection of specific frequencies against a noise background.

A layout of the setup is shown in Fig. 3.1. The pulse train from a 1 MHz ytterbium amplified laser (Spectra Physics Spirit-HE) is focused into an 8 mm thick Yttrium Aluminum Garnet (YAG) crystal using a focusing lens (L1, focal length 5 cm), resulting in white-light generation (WLG) [159]. The power input into the YAG crystal is kept at 0.9 W. Re-collimation of the beam to a 3.7 mm diameter ($1/e^2$) is perfomed using a 4 cm focal length lens (L2). A short pass (SP 950 nm OD4, Edmund) filter is used to reject the residual fundamental light.

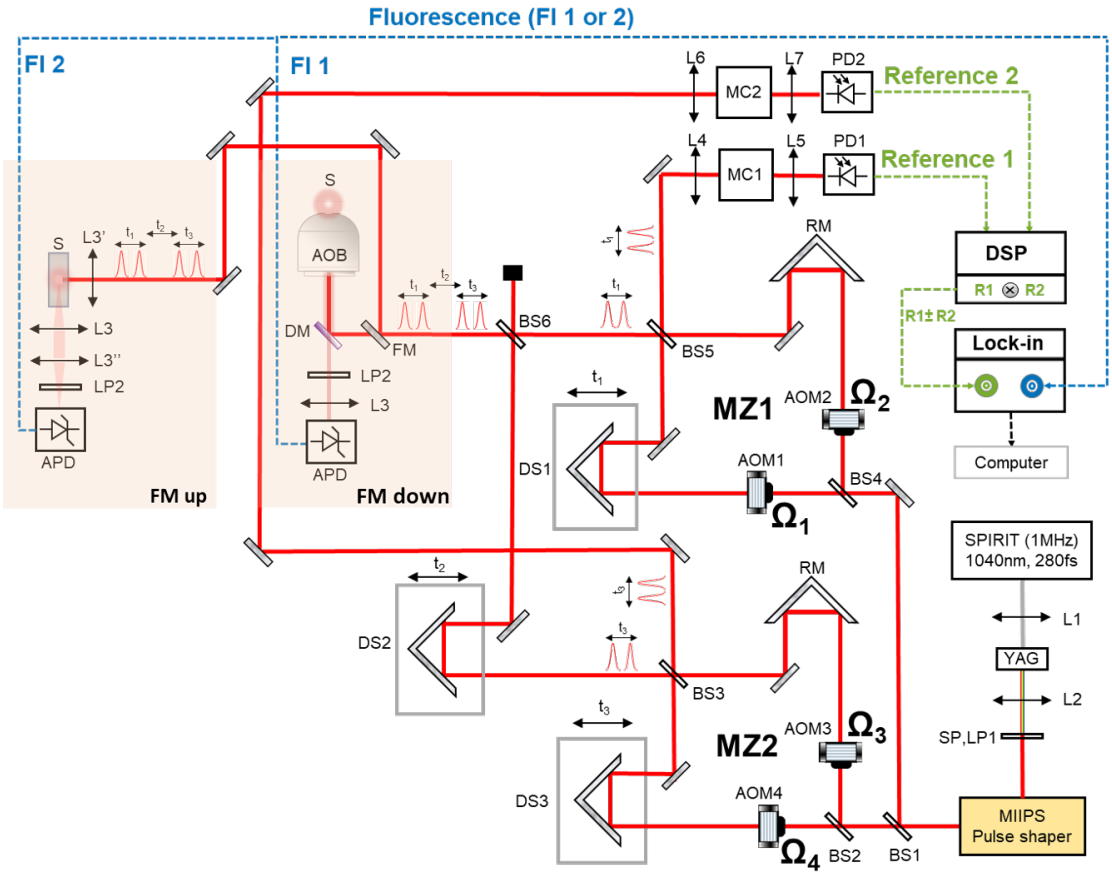

Figure 3.1: Experimental setup of the phase-modulated fluorescence-detected 2D

spectrometer: Lens (L), beam splitter (BS), acousto-optic modulator (AOM), SLM-based 4F pulse shaper, Mach–Zehnder (MZ) interferometer, Digital signal processor (DSP) , delay stage (DS), retroreflector mirror (RM), monochromator (MC), avalanche photodiode (APD), variable gain photodiode (PD), short pass optical filter (SP), long pass optical filter (LP), dichroic mirror (DM), flip mirror (FM), sample (S), air objective (AOB).

To ensure that the pulses are Fourier-transform-limited at the sample position, the beam is routed to a SLM-based 4F pulse shaper [160] (MIIPS 640P, Bio-photonic Solutions) for dispersion pre-compensation and further bandwidth reduction. After the pulse shaper, a 50/50 beam splitter (BS1, Newport, 10B20BS.2) splits the pulse energy equally and directs it to two Mach–Zehnder interferometers (MZ1 and MZ2) in order to generate the excitation and detection pulse pairs.

At the entrance of each interferometer, beam splitters (BS2 and BS4) divide the pulse energy equally along the fixed and moving arms in each MZ. An acousto-optic modulator (AOM, Isomet, M1142-SF80L) inserted in the optical path of each arm modulates each pulse at a particular radio frequency Ω_i, imparting a time-varying phase shift to the consecutive pulses of the pulse train [69]. All four AOMs are driven by the same RF signal generator (Novatech, 409B), which uses a common internal clock for generating the modulation signals $\Omega_{1,2,3,4} = (80.110, 80.103, 80.000, 79.975)$ MHz. Each pair of the modulated pulses is recombined on a beam splitter (BS3 and BS5) at the interferometer outputs, with the interpulse delay within each interferometer (t_1 and t_3), varied using a mechanical delay stage (DS, Newport, M-VP25XL). While the time delays t_1 and t_3 correspond to the coherence and detection times, respectively, the waiting time t_2 is controlled by an additional delay stage (DS2, Newport, ILS150). All three mechanical stages are controlled using a motion controller (Newport, XPS-Q4). The recombined outputs from BS3 and BS5 oscillate at the difference frequency of the AOMs, that is, $\Omega_{12} = 7$ kHz and $\Omega_{34} = 25$ kHz respectively. One of the outputs from BS3 and BS5 is routed to a monochromator

(MC, Dynacil, MC1-05G, 50 μm slit) to spectrally narrow the pulse pair at a center wavelength ω_{ref} = 825 nm with a FWHM bandwidth of 4 nm. The spectrally narrowed reference signals R1 and R2 from MZ1 and MZ2 respectively are collected by variable-gain photodiodes (PD, Thorlabs PDA36A, set at 20 dB gain) and sent to a 24 bit digital signal processor (DSP, Analog Devices, ADAU1761). The DSP mixes the two reference signals R1 and R2 to generate the reference signals corresponding to rephasing and non-rephasing frequencies at $\Omega_R = -\Omega_{12} + \Omega_{34} = 18$ kHz and $\Omega_{NR} = \Omega_{12} + \Omega_{34} = 32$ kHz respectively. These references are sent to the lock-in for detection of the fluorescence signal relative to the reference wavelength, ω_{ref}, enabling physical undersampling [74] of the signal to be collected. This means that the signal centered at ω_{eg} corresponding to the electronic energy gap of the material can be sampled at a lower frequency $\omega_{eg} - \omega_{ref}$. Thus, undersampling makes the measurement insensitive to phase noise resulting from mechanical delay fluctuations. The other outputs from BS3 and BS5 are recombined at BS6 to form a collinear four-pulse train that is used to excite the sample. The other half from BS6 is dumped.

Prior to the experiments, the pulses are first compressed to 17 fs using MIIPS (multi-photon intrapulse interference phase scan) [161, 162] algorithm in a 20 μm thick β-barium borate (BBO) crystal at the sample position. The four-pulse sequence interacts with the sample in two detection modes labeled as flip mirror (FM) up and FM down in Fig. 3.1. FM up shows the illumination of the sample (S) using a microscope air objective (AOB) with a beam spot size of $\sim$1 μm and collection of fluorescence in the epi-detection geometry. A dichroic mirror (Semrock) with cutoff at 875 nm is used to filter out the laser and let the fluorescence through. Additional long-pass (LP2) filters are used to reject the residual laser. The fluorescence is then focused onto an avalanche photodiode (APD, Hamamatsu C12703-01) using a lens (L3) of focal length 5 cm. FM down shows a 90 degree detection scheme, where the

four collinear pulses are focused with a lens (L3') of focal length 5 cm to a spot size of ∼16 μm at the sample position. The total power at the sample position is 22 μW, corresponding to an energy of 22 pJ at 1 MHz. The fluorescence is collected in the 90 degree direction using a large aperture collimating lens (L3, Thorlabs LA1401-AB, 2" diameter) with a focal length of 6 cm, and then focused onto the APD using a lens with a focal length of 10 cm (Thorlabs LA1442-B, 2" diameter). Long pass (LP2) filters are used to prevent any laser scatter from entering the APD.

Signal from the APD is split into two channels and sent to the lock-in for detection of rephasing and non-rephasing signals. Step-scanning of the time delays is used for the measurements reported in Ch. V. At each t_2, a 2D grid is recorded as a function of t_1 and t_3. In our collection scheme, t_1 takes the shortest time to measure while t_2 delay takes the longest. A lock-in time constant of 100 ms is used and the signal at each combination of the three delays t_1, t_2, and t_3 delays is averaged over 80 acquisitions.

3.3 Principles of lock-in detection

The phase-modulation based approach relies on lock-in detection of the signals of interest against a noisy background. A lock-in amplifier performs a multiplication of its input with two replicas of a reference signal, one of them shifted by 90°, also sometimes called down-mixing or heterodyne/homodyne detection, and then applies an adjustable low-pass filter to the result [7]. This process effectively "demodulates" the signal of interest, resulting in phase-sensitive detection and isolation of the frequencies of interest from all other frequency components. Fig. 3.2, adapted from [7], depicts the working principle of a lock-in amplifier. The reference signal can either be generated in the lock-in amplifier itself or provided as an external input. As highlighted in the last section, we generate the references by sending the other output from each Mach-Zehnder interferometer through a monochromator. This signal is

essentially a two-pulse interference signal evaluated at the set monochromator frequency. It has a phase that oscillates at the difference AO frequency and varies with the interpulse delay t_{ij} at the monochromator frequency. Since the time dependence of the reference phase is known, the relative phase of the fluorescence signal can be determined for different delays. Thus, the in-phase and in-quadrature components of the fluorescence signal relative to the reference signal are obtained [69].

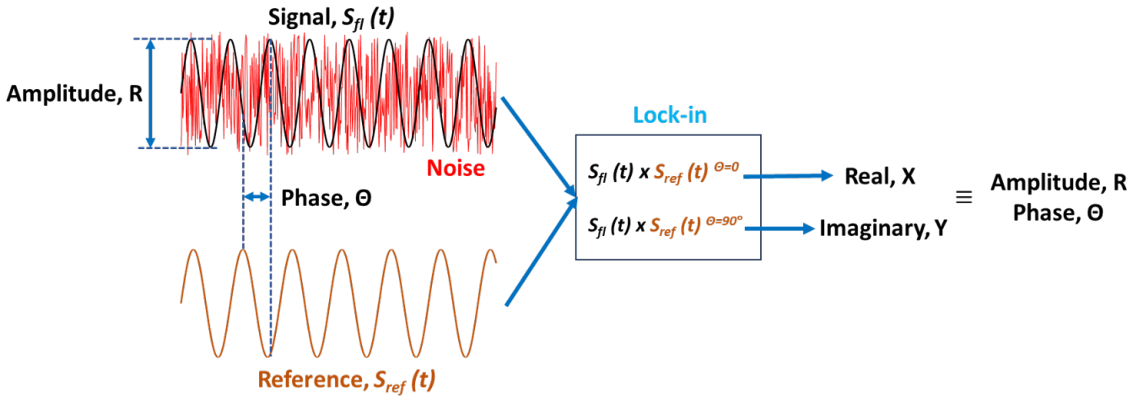

Figure 3.2: Working of a lock-in amplifier: The input contains the signal of interest against a large noise background. It is mixed with two phase-shifted copies of a reference signal oscillating at the frequency of interest for phase-sensitive detection, yielding the signal amplitude and phase. Figure adapted from [7].

3.4 Incoherent mixing test

Bargigia et al [149] pointed out the incoherent mixing contributions to the nonlinear F-2DES signal can originate from the material as well as the detection architecture. Therefore, it is extremely important to investigate the linear signals in the time domain to look for the presence of incoherent mixing of the linear signals. Following the methodology outlined by Bargigia et al[149], we measure the linear signals oscillating at $\Omega_{12} = 7$ kHz and $\Omega_{43} = 25$ kHz as a function of t_1 and t_3 with the setup given in Fig. 3.1. LH2 suspended in Tris-HCl buffer is used for the measurements while flowing at a flow rate of 110 mL/min. The sample is excited with 22 pJ pulse energy. The signal modulating at Ω_{12} is expected to oscillate along t_1 for a fixed t_3

delay and remain constant as a function of t_2 for a fixed t_1. Fig. 3.3 (a) and (b) show 2D plots of the linear signals oscillating at Ω_{12} and Ω_{34} respectively recorded as a function of t_1 and t_3. For (a), linear cuts are taken along t_1 at t_3=0 and along t_3 at $t_1 = 0, 21, 56$ fs. Cuts along the t_3 axis are shown by green, magenta, and blue dashed lines respectively. The corresponding cuts are shown in Fig. 3.4 (a). Similarly, for (b) linear cuts are taken along t_3 at t_3=0 and along t_1 at $t_3 = 0, 21, 56$ fs. Cuts along the t_3 axis are shown by green, magenta, and blue dashed lines respectively. The corresponding cuts are shown in Fig. 3.4 (b). As would be expected in the absence of incoherent mixing, we see that MZ1 signal cuts along t_3 and MZ2 signal cuts along t_1 are mostly noise.

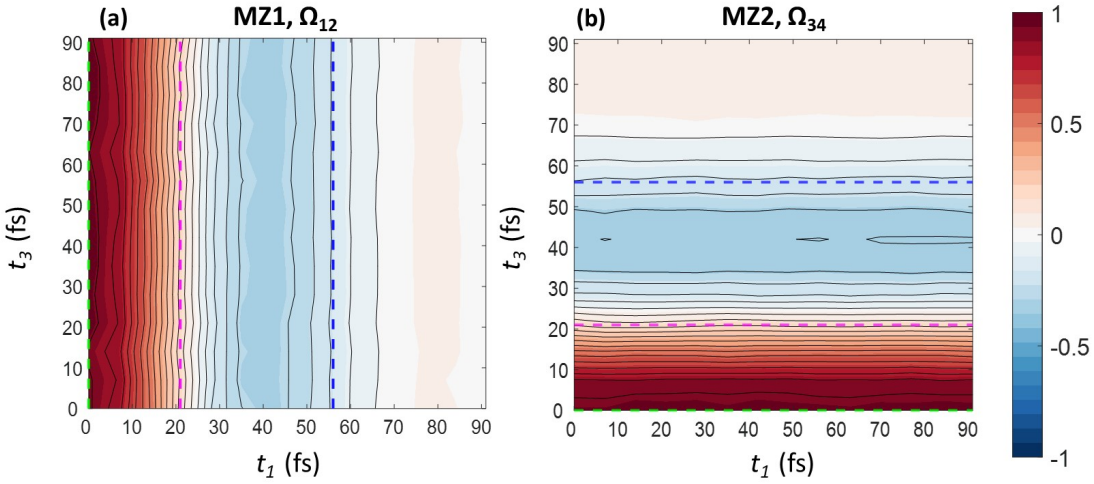

Figure 3.3: Linear signals oscillating at (a) Ω_{12} and (b) Ω_{34} recorded as a function of the time delays t_1 and t_3.

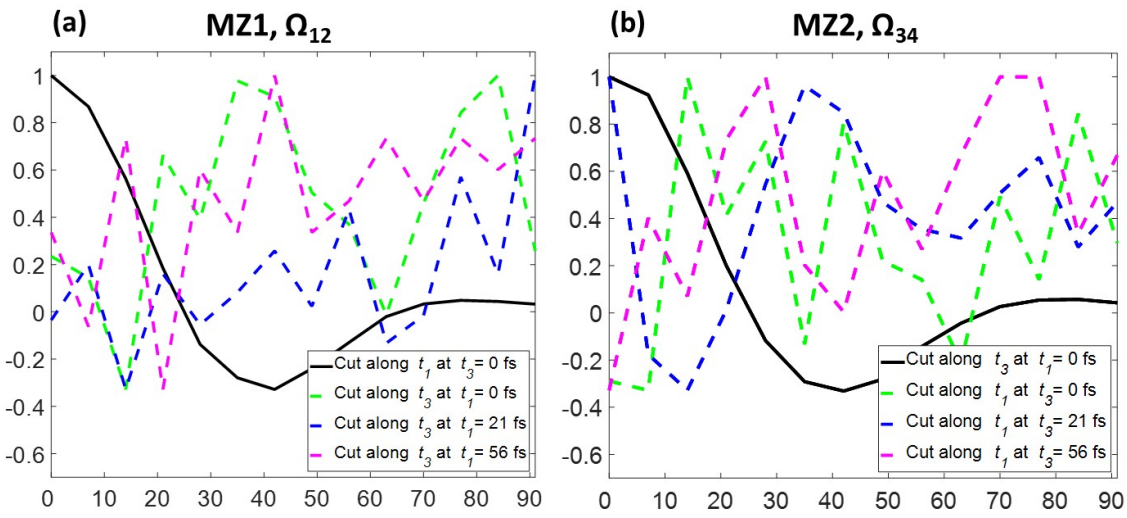

Figure 3.4: (a) Linear cuts taken along t_1 at t_3=0 (black) and along t_3 at $t_1 = 0, 21, 56$ (green, magenta, and blue respectively) (b) Linear cuts taken along t_3 at t_1=0 (black) and along t_1 at $t_2 = 0, 21, 56$ (green, magenta, and blue respectively).

3.5 Detector non-linearity test

The most suitable photo-diodes for detecting in the near infrared region corresponding to the fluorescence signals for the samples studied in this thesis use Silicon (Si) as their material of choice. In the work presented in this thesis, two Si-based detectors were used. The first one, a PIN photodiode (FEMTO Messtechnik GmbH, OE-200-SI), provides the advantage of low levels of noise in detection. PIN photodiodes are made up of an intrinsic layer of semiconductor sandwiched between two heavily doped p-type and n-type semiconductor layers. The other type of detector used in our fluorescence detection measurements is an avalanche photodiode (Hamamatsu C12703-01). The electron-hole pair generated due to the incidence of a photon on the detector is subjected to a large reverse bias. Due to large acceleration under the high bias the charge carriers generate even more charge carriers due to impact ionization in the material, creating an avalanche effect and hence, high gain values. Avalanche photodiodes provide higher sensitivity compared to the PIN photodiodes,

but also generate noise at a higher level. Therefore, while the PIN photodiodes offer lower responsivity they are useful when low levels of noise are required.

Although Si is the most commonly used option for detectors, it is known to exhibit a plethora of non-linearities with respect to the incident light intensity [77] and can lead to unwanted effects and noise in measurements if the response is not characterized properly. Ideally, an undistorted signal response would mean that the output voltage scales linearly with the input light intensity to ensure accurate quantification of the intensity of the spectral features. When non-linearities persist, the dependence on the incident field can change over time, resulting in signal drifts. Higher harmonics are often observed in the presence of detector non-linearities. As described by Silva and co-workers [150], non-linearities in detection, due to the detector material or other electronic origins, can lead to incoherent mixing of linear signals observed during the detection time. In addition, saturation effects can be observed when the detector response plateaus in case of intense incident fields. In order to make sure that non-linear detector response does not contribute to signal distortion in our fluorescence measurements, we performed the following basic tests to characterize the linearity. Fig. 3.5 (a) shows the tests done on the detector FEMTO Messtechnik GmbH, OE-200-SI set at Low Noise setting at a gain of 10^7 V/W and an operating bandwidth of 50 kHz. The AO modulation frequencies were chosen such that the signals of interesting fall well under this limit. Fig. 3.5 (b) shows the power dependence of Hamamatsu C12703-01 set at a gain of 1.5 x 10^8 V/W and an operating bandwidth of 100 kHz.

For the tests shown here, a 1 kHz output from a degenerate optical parametric amplifier (DOPA) centered at 800 nm with a 120 nm bandwidth, is incident on a beam sampler (BSF05-B, Thorlabs). The reflected beam from the beam sampler, which is

$\sim$1 % of the input light is focused onto the detector. A power diode placed in the transmitted arm after the beam sampler is used to measure the powers shown on the x-axis in Fig. 3.5. The output signal from the detectors is recorded as a peak-to-peak voltage on a digital acquisition board (National Instruments, PCIe-6321). The aim behind using this source is to access a larger dynamic power range as compared to the 1 MHz source we use for fluorescence detection-based measurements as the highest power we can achieve from our F-2DES setup is limited by AOM throughput. The inset shows a zoomed-in range of the power-voltage curve for levels relevant to our measurements, with typical highest voltage (peak-to-peak) values from Hamamatsu C12703-01 and FEMTO Messtechnik GmbH, OE-200-SI recorded at 80-120 mV and 30-55 mV. As can be seen from Fig. 3.5, the output regime where we operate for both the detectors is linear in input powers. Both the curves in the inset are fitted to a linear curve with R values of 0.9985 and 0.9996 for FEMTO Messtechnik GmbH, OE-200-SI and Hamamatsu C12703-01 respectively.

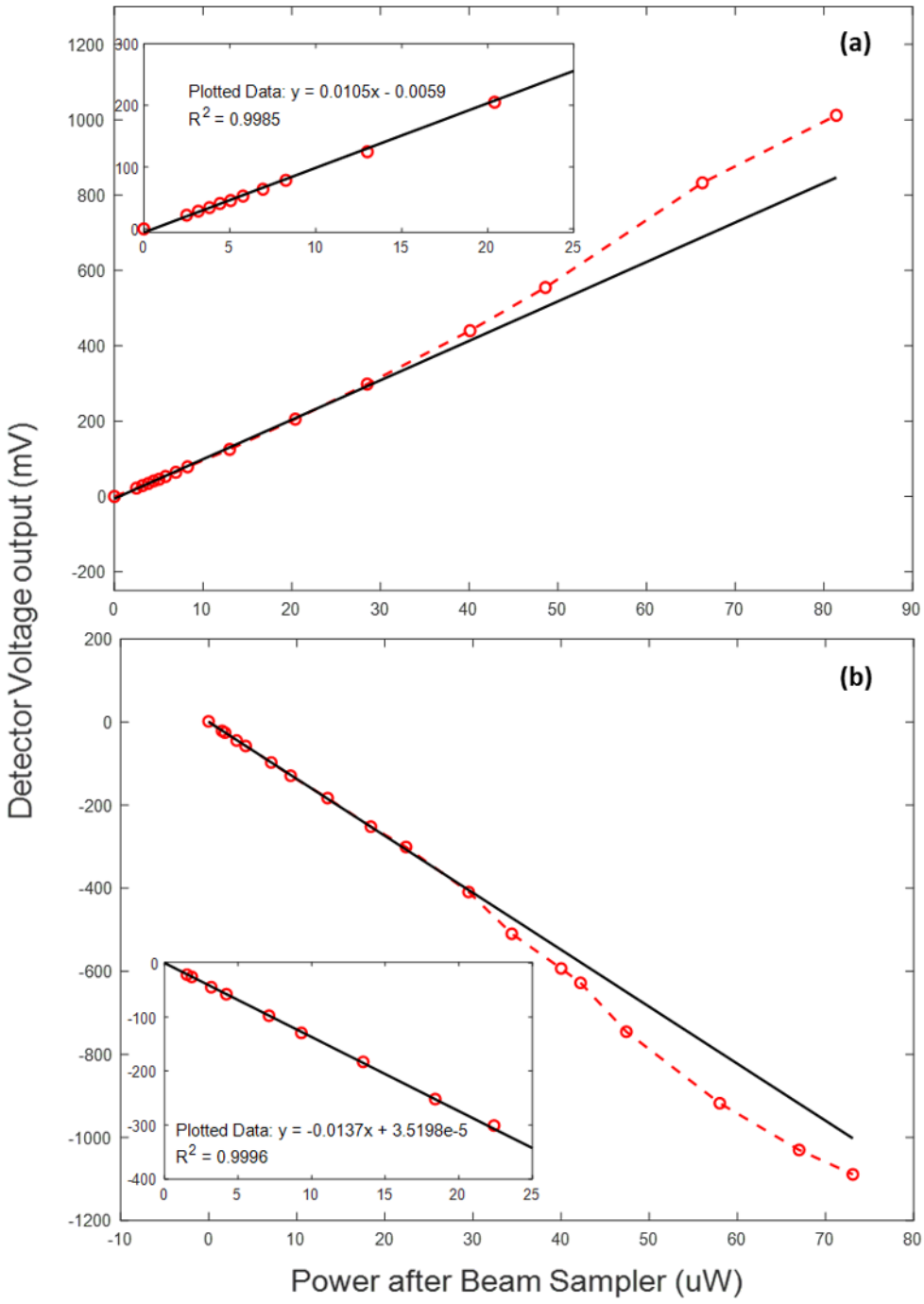

Figure 3.5: Linearity tests for (a) FEMTO Messtechnik GmbH, OE-200-SI detector and (b) Hamamatsu C12703-01 detector. The insets show the the power-voltage curves zoomed in on the levels used in our measurements. The zoomed-in data are fit to straight lines with very low residuals.

CHAPTER IV

Photosynthetic Energy Transfer: Missing in Action (Detected Spectroscopy)

This chapter is adapted from a manuscript in preparation, entitled "Photosynthetic energy transfer: missing in action (detected spectroscopy)," by Ariba Javed, Julian Lüttig, Kateřina Charvátova, Stephanie Sanders, Rhiannon Willow, Muyi Zhang, Alastair T. Gardiner, Pavel Malý, and Jennifer P. Ogilvie.

4.1 Abstract

In recent years, action-detected ultrafast spectroscopies have gained popularity. These approaches offer some advantages over their coherently-detected counterparts, enabling spatially-resolved and *operando* measurements with high sensitivity. However, the excited-state populations that are detected in these experiments have lifetimes that are orders of magnitude longer-lived than excited-state coherences resulting in fundamental differences in the observed signals between the two techniques. Here we F-2DES of the LH2 complex from purple bacteria. We demonstrate that the B800-B850 energy transfer process in LH2 is barely discernable in F-2DES, representing $\sim$3 of the total signal. This is in stark contrast to measurements using C-2DES. We develop a simple model that reproduces the main features of our F-2DES data, show-

ing that the energy transfer kinetics are obscured by excited-state-lifetime-limited contributions that arise from the multichromophoric and excitonic nature of LH2. Our work shows that careful consideration of the system characteristics is needed in choosing between coherent and action-detected spectroscopies for dynamical studies.

4.2 Introduction

2DES has emerged as a powerful tool for studying electronic structure and dynamics in systems ranging from photosynthetic complexes [84, 163] to liquids [164] and solid-state materials [165, 166]. Both high temporal as well as spectral resolution can be achieved using Fourier-transform 2DES, providing a significant advantage over lower dimensional approaches such as pump-probe spectroscopy. In addition, by expressing the signal as a 2D map correlating the excitation and detection frequencies, 2DES effectively decongests the spectral information available from conventional linear spectroscopies, enabling a better understanding of a wide variety of systems. The most common implementation of 2DES utilizes a sequence of three time-delayed pulses that interact with the sample, generating a macroscopic third-order polarization that radiates a coherent signal field. Phase-matching is typically used to detect the coherent signal in a specific direction, requiring a sample volume greater than $\sim \lambda^3$ (where λ is the excitation wavelength) to attain the coherent build-up of a macroscopic signal [134]. This limits the use of C-2DES to studies of extended samples containing large numbers of molecules, making it ill-suited for single molecule studies and for combining with microscopy.

In recent years, motivated by the desire to make spatially-resolved measurements and to correlate optical excitation with a broad range of observables, action-detected variants of 2DES and pump-probe spectroscopy have been developed that employ a fully collinear geometry, relying on phase-cycling or phase-modulation to extract the

signals of interest. These approaches overcome some of the limitations of coherent 2DES and have employed fluorescence [70, 74, 122], photocurrent [120, 123, 124, 132], photoelectron [126, 128, 167], or photoion [125, 168] emission as experimental observables. Fluorescence-detection, in general, has enabled single molecule sensitivity and spatially-resolved measurements, while photocurrent, photoion and photoelectron detection have enabled *operando* device studies [127]. Numerous interesting systems including photosynthetic complexes [70, 122], atomic vapors [74, 167], molecular dimers [72, 129], dyads [130], semiconductor nanostructures [120, 123, 131, 133], as well as photovoltaic devices [127, 132, 169] have been studied using action-detected 2DES techniques. However, there are significant fundamental differences between action-detected and coherent techniques, and the interpretation of the spectra obtained from action-detected 2DES still remains an active research topic [71, 124, 141–145]. Studies comparing the spectra of coherently and action-detected measurements have been reported [129, 147, 148], but to date there have been relatively few studies of excited state dynamics with action-detected methods. In this work, we focus F-2DES to highlight the similarities and differences between coherent and action-detected 2DES techniques for studying multichromophoric systems.

Compared to coherent C-2DES, in which a sequence of three pulses interact with the sample, action-detected 2DES adds a fourth pulse, projecting the third-order polarization onto a fourth-order excited-state population. The resulting observable is an incoherent signal proportional to this excited-state population [74]. The nontrivial difference between coherent and F-2DES arises due to the fourth pulse which leads to an additional signal-generating Liouville pathway [71, 72, 141]. The double-sided Feynman diagrams corresponding to these pathways were discussed in Chapter III. In C-2DES, three contributions make up the spectra - GSB, SE and EA pathways with the ESA pathway contributing with an opposite sign relative to the GSB and

SE pathways. In F-2DES, in addition to GSB and SE pathways, two distinct and oppositely-signed ESA pathways exist, arising from either the singly or doubly excited states. Depending on the relative quantum yields of the singly and doubly excited-states, the ESA pathways may partially or fully cancel, dramatically changing the appearance of action-detected 2DES relative to C-2DES [71, 72].

In addition to differences in the Liouville pathways for coherent and action-detected 2DES, the excited-state populations that are measured in action-detected experiments have lifetimes that are orders of magnitude longer-lived than excited-state coherences, often lasting ns. This delay in detection opens up additional opportunities for excited-state populations to interact and become correlated over longer timescales. Second-order decay processes such as bimolecular recombination, exciton-exciton annihilation (EEA), Auger recombination, and photocarrier scattering can occur in addition to the first-order decay processes [149]. The appearance of cross peaks in F-2DES at early waiting times is attributed to these processes [73, 141] rather than to excitonic coupling [71], unlike in C-2DES. Using F-2DES, strong cross peaks at early waiting times have been reported in multichromophoric systems [70, 122], in contrast to the observations in C-2DES studies with weak to no cross peak presence [16]. Additionally, the unwanted incoherent mixing of linear responses, originating from nonlinear population dynamics such as EEA, Auger recombination, or nonlinearities in the detection can occur, contaminating the nonlinear signal and obscuring spectral dynamics [143, 145, 149, 150]. F-2DES has revealed clear excited-state dynamics in small systems such as molecular dyads [72, 129, 130] and Rb atoms [168]. However, there have been relatively few reports of excited-state dynamics in extended multichromophoric systems, with the exception of weak kinetic signatures reported in photocurrent-detected 2DES studies of an organic photovoltaic device [124]. Recent theoretical work suggests that action-detected 2DES is poorly suited for this task [6].

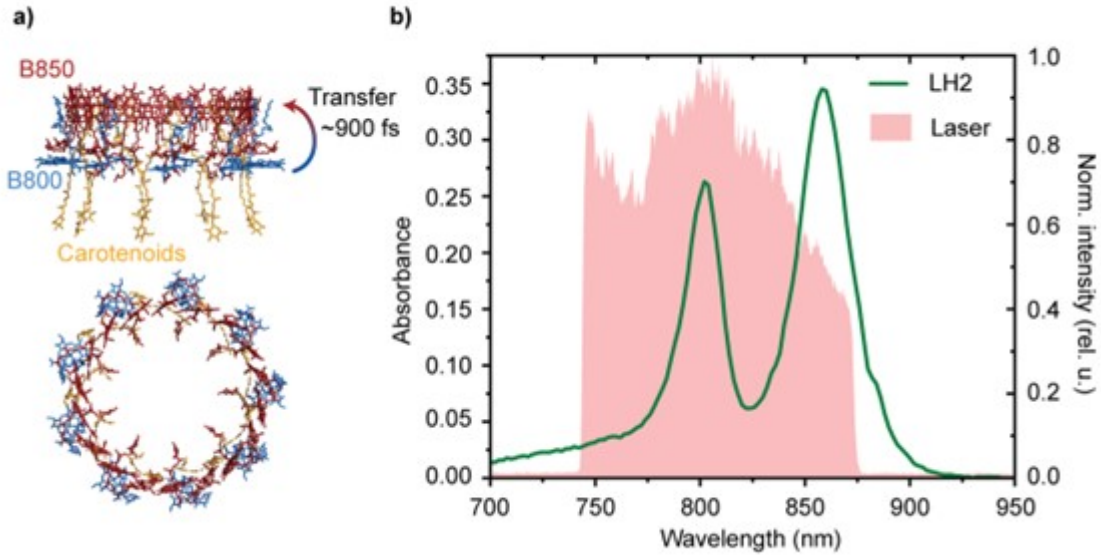

Figure 4.1: a) Crystal structure of LH2 showing the arrangement of carotenoids and BChl *a* pigments in the B800 and B850 rings. Figure obtained from Protein Data Bank file 1NKZ [8] using PyMOL. b) The linear absorption spectrum of LH2 from *Rbl. acidophilla* (green) in 20 mM Tris-Cl buffer (pH 8.0) with 0.1 % LDAO detergernt, taken at room temperature. The laser spectrum used for the measurements is shown in solid pink.

Here we study the LH2 complex from the purple bacterium *Rbl. acidophilla* using C-2DES and F-2DES to compare their relative ability to resolve excited-state dynamics in multichromophoric systems. The well-characterized structure and the extensive previous ultrafast studies [8, 27, 39, 44, 53], of LH2 make it an excellent model system for this purpose. The structure of LH2 from *Rbl. acidophilla* [27] is shown in Fig. 4.1. It is comprised of two BChl *a* rings, B800 and B850. The B800 ring consists of 9 monomeric BChl *a*, which are weakly coupled to each other giving rise to an absorption peak at ∼800 nm. The B850 ring consists of 18 strongly coupled dimeric BChl *a* units, producing to a peak absorption at ∼850 nm. Fig. 4.1 shows the structure and orientation of the B800 and B850 rings in LH2, and depicts the process of energy transfer between them. Many previous experimental studies have used C-2DES to probe the excited state dynamics within LH2, and have reported timescales ranging

from ∼700 fs to 1 ps for the B800→B850 energy transfer [53, 59, 60, 170, 171]. Previous F-2DES studies of LH2 focused on understanding the origin of the prominent cross-peaks between B800 and B850 transitions, which arises due to the complete cancellation of the oppositely-signed ESA signals [71]. These studies showed spectra at $t_2 = 0$ but did not report any waiting-time-dependent F-2DES measurements.

4.3 Modeling of F-2DES on LH2

We thank our collaborators, Kateřina Charvátova and Pavel Malý, for doing the simulations to support the experimental dynamics data. Here, we report preliminary results from them to show the qualitative agreement of the waiting time traces for different peaks, and acknowledge that this is still a work in progress.

We take the transition dipole moments of BChl *a* molecules from the X-ray structure of LH2 (Protein data bank 2FKW [172]). The couplings have been calculated by the dipole-dipole approximation. The site energies are set to 12320 cm^{-1} and 12520 cm^{-1} for B850 dimers and 12520 cm^{-1} for B800 monomers. Gaussian energetic disorder is considered for the site energies. Diagonalization of the disordered Hamiltonian gives the excitonic states. The average excitonic state energies and oscillator strengths are shown in Fig. 4.2 (a). To calculate the spectra, we take each BChl *a* with 200 cm^{-1} wide Gaussian lineshape, which form the excitonic lineshapes when taking into account the redistribution of oscillator strength and exchange narrowing. The calculated absorption spectrum is shown in Fig. 4.2 (b).

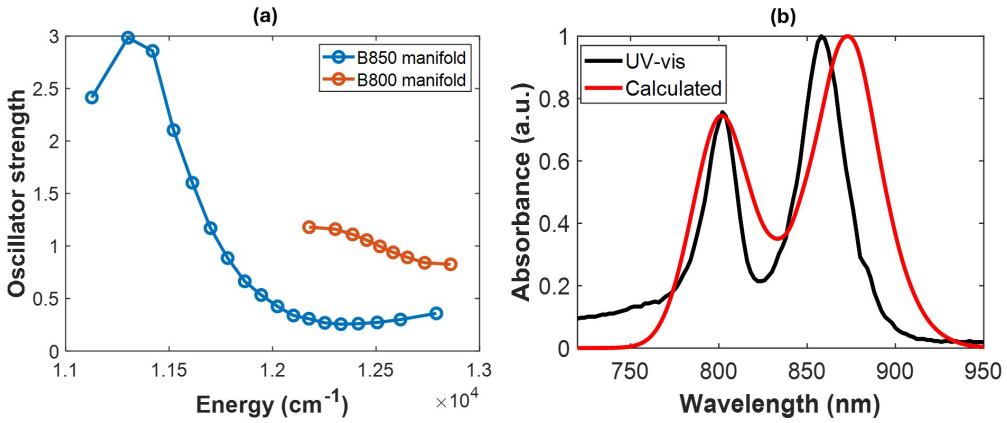

Figure 4.2: (a) Simulation data showing the average excitonic energies calculated using a disordered Hamiltonian and distribution of oscillator strength within the B850 (blue) and B800 (orange) manifolds, reflecting the effect of delocalization within each ring. It can be seen that the splitting leads to a more substantial variation in the oscillator strength of some states versus the others in the B850 band compared to the B800 band. (b) Calculated absorption spectrum (red) plotted along with the UV-visible absorption spectrum (black) of LH2 suspended in 20 mM Tris-Cl buffer(pH 8.0) with 0.1 % LDAO detergent.

For the calculation of the F-2DES spectra, we take the individual downhill exciton relaxation step time within the B800 manifold to be 100 fs and within the B850 band to be fast ∼30 fs. These rates agree with the observed rates [173], and justify the fact that a number of steps contribute to the relaxation withing the rings. Inter-ring transfer is accounted for with a time constant of 830 ps. The following coupling parameters are used for modeling: inter-neighbor coupling is 200 cm^{-1} and 12 cm^{-1} in B850 and B800 respectively. Disorder is taken to be 380 cm^{-1} in B850, and 230 cm^{-1} in B800, while disorder is represented by a Gaussian with a linewidth of 200 cm^{-1}. The simulated F-2DES spectra and time traces are shown in Fig. 4.3 and Fig. Fig. 4.5.

4.4 Results

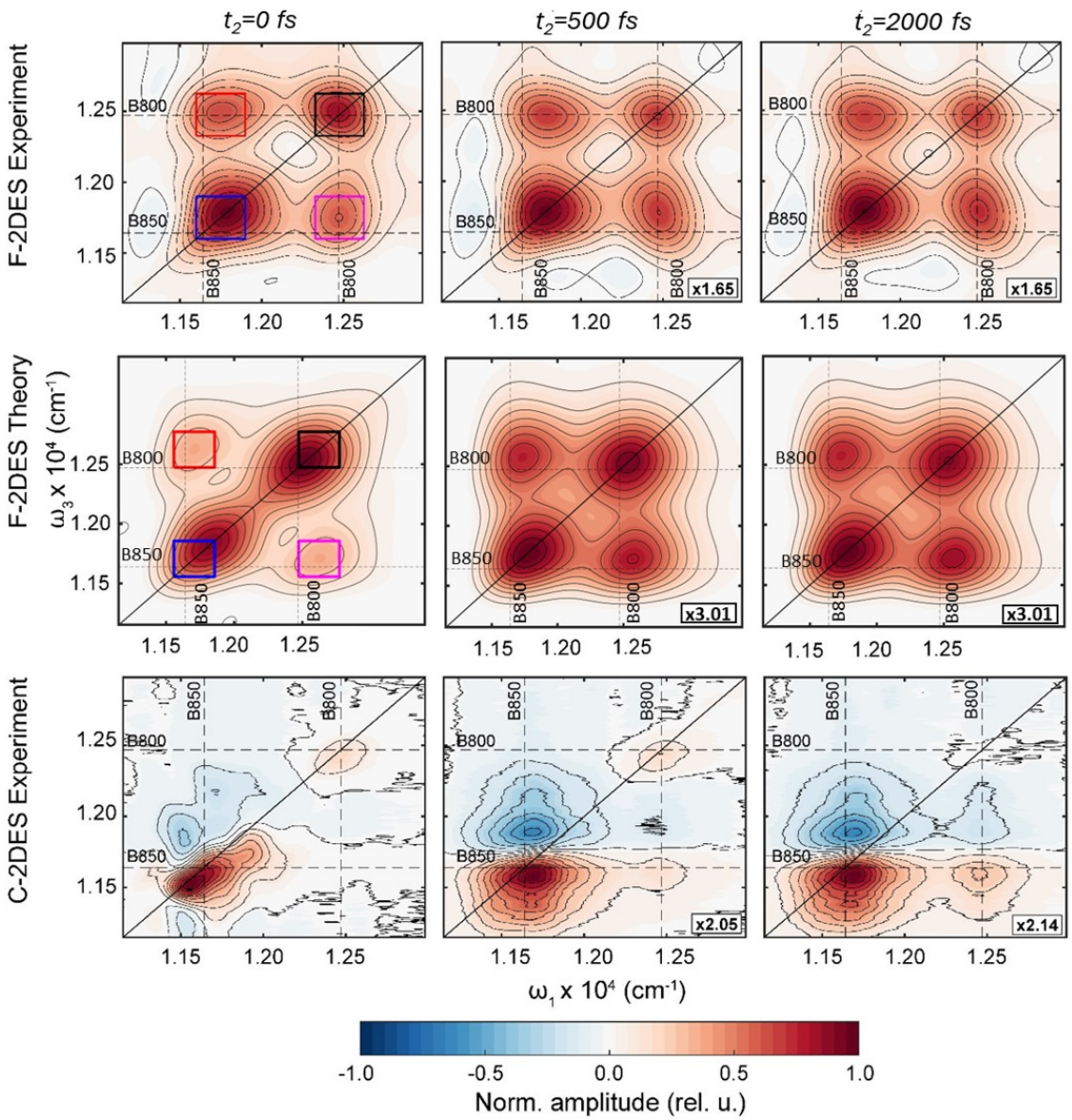

Figure 4.3: (a) F-2DES spectra of LH2 at waiting times t_2=0 fs, 500 fs, and 2000 fs. The colored squares indicate the region over which the kinetic traces shown in Fig. 2 were averaged. b) Simulated F-2DES spectra of LH2 at waiting times t_2=0 fs, 500 fs, and 2000 fs. c) Coherent 2DES spectra of LH2 at waiting times t_2=0 fs, 500 fs, and 2000 fs.

The absorptive F-2DES spectra of LH2 are shown in Fig. 4.3 (top row) at waiting times t_2=0 fs, 500 fs and 2 ps. The t_2=0 fs spectra show strong B800 and B850 diagonal peaks and prominent cross-peaks, consistent with previous work [70, 122]. By

500 fs, all of the peak amplitudes have diminished, and the relative amplitudes have changed, with the upper diagonal peak (UDP) from B800 losing intensity relative to the lower diagonal peak (LDP) from B850, and the ratio of cross-peak/diagonal peak amplitude increasing. Overall, the F-2DES spectra show little evolution in peak amplitudes or shapes as a function of waiting time, with the lower cross-peak (LCP) showing the largest evolution in peak shape. The simulated F-2DES spectra are shown in Fig. 4.3 (middle row), displaying good agreement with the experimental measurements. In contrast to the F-2DES spectra, Fig. 4.3 (bottom row) shows the C-2DES spectra of LH2 at the same waiting times, revealing dramatic evolution from $t_2 = 0$ fs to later times.

Fig. 4.4 shows the waiting-time dependence of the F-2DES diagonal and cross-peak amplitudes. The colored squares overlaid on the $t_2 = 0$ fs F-2DES spectrum in Fig. 4.3 indicate the region over which the signal was integrated to obtain the kinetic traces shown in Fig. 4.4. All four peak amplitudes show a dramatic drop within the pulse overlap region, followed by very small amplitude changes within the first 2 picoseconds. These small changes are more apparent in the panels below each kinetic trace, where the vertical scale is expanded to more readily visualize the peak kinetics within the first 2 ps. The UDP shows a small rise within the first ∼400 fs followed by a slow decay. An exponential fit of the decay reveals a time constant of 1480 ± 375 fs with ∼5% decay in the UDP signal. The LDP shows a rapid decay within the first ∼200 fs followed by a roughly constant signal level. The upper cross-peak (UCP) shows little evolution during the first 2 ps. The LCP is fit to an exponential rise which yields a time constant of 1345 ± 575 fs, amounting to ∼6% of the signal amplitude. The corresponding waiting-time dependence of the C-2DES diagonal and cross-peak amplitudes is shown in Fig. 4.9. In contrast to F-2DES, the peak amplitude changes in C-2DES are much more apparent. In particular, the LCP, which is negligible at

early waiting times, shows an exponential rise with a time constant of 825 ± 10 fs, amounting to ∼100% of the cross-peak amplitude.

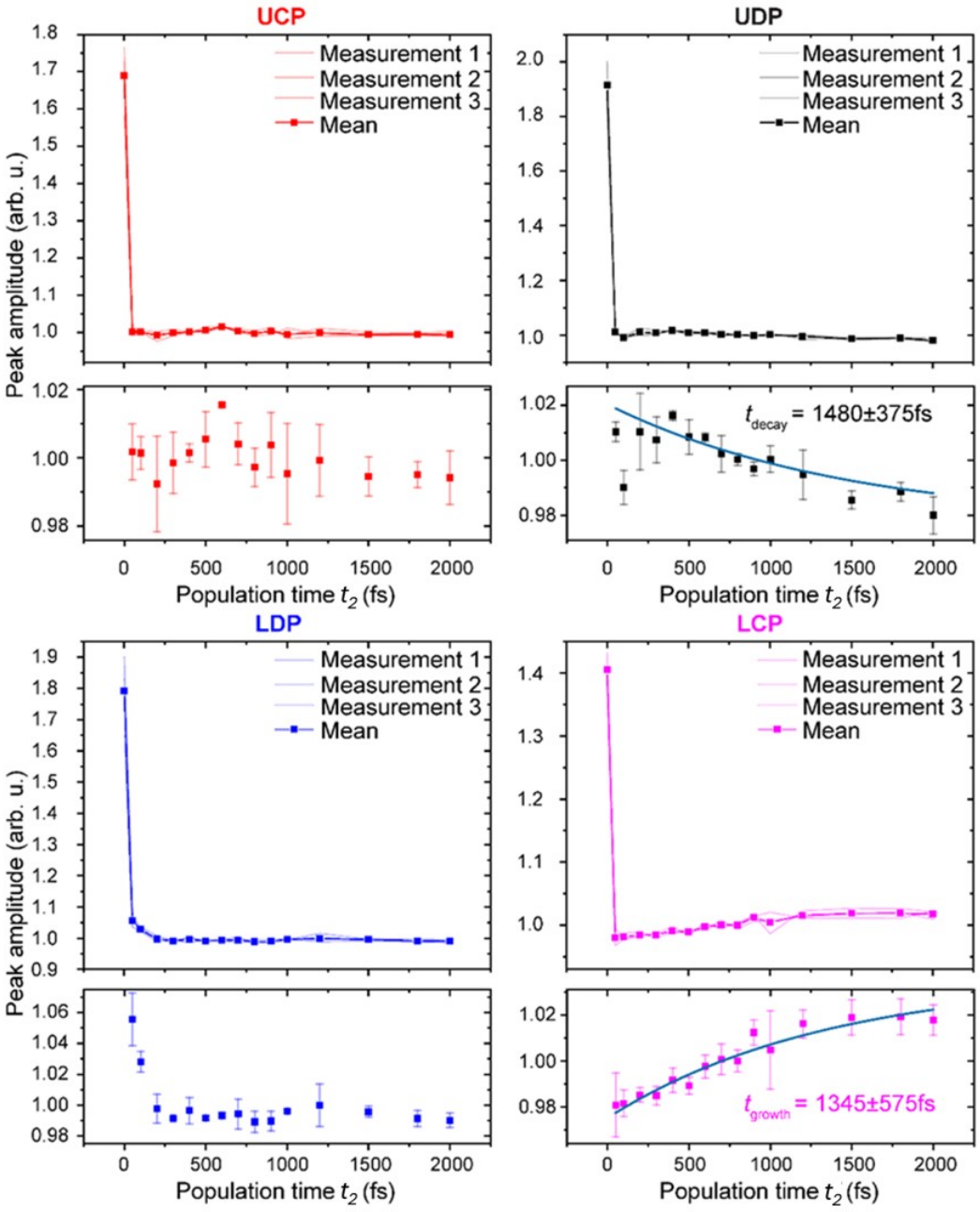

Figure 4.4: Kinetic traces as a function of waiting time t_2 at the diagonal and cross-peak positions locations, obtained by averaging over the regions indicated by colored squares in Fig. 4.3. Below each kinetic trace, an expanded vertical scale excludes the $t_2 = 0$ fs peak to more clearly visualize the weak kinetic signatures. Error bars are derived from three distinct measurements. Exponential fits to the upper diagonal peak

(UDP) and lower cross-peak (LCP) are shown. A time constant $t_{decay} = 1480 \pm 375$ fs is obtained for the UDP with ∼5% decay, and for the LCP, $t_{growth} = 1345 \pm 575$ is obtained with the signal rising by ∼6%.

For comparison with the experimental F-2DES data, Fig. 4.3 shows the simulated F-2DES spectra and the waiting time dependence of the diagonal and cross-peaks. Consistent with the data, the simulations also show a dramatic decrease in signal amplitude of all of the peaks after $t_2 = 0$ fs. Quantitatively, the fraction of signal change as a function of waiting time t_2 for both the UDP and LCP obtained from the simulations is slightly higher ∼8%, as compared to the experiments (∼5% for the UDP decay and ∼6% for the LCP rise). We attribute these differences to the differences in the lineshapes in the experimental and simulated data. We also note that the choice of the integration areas for each peak (shown in the first column of Fig. 4.3) may affect the fits to our data.

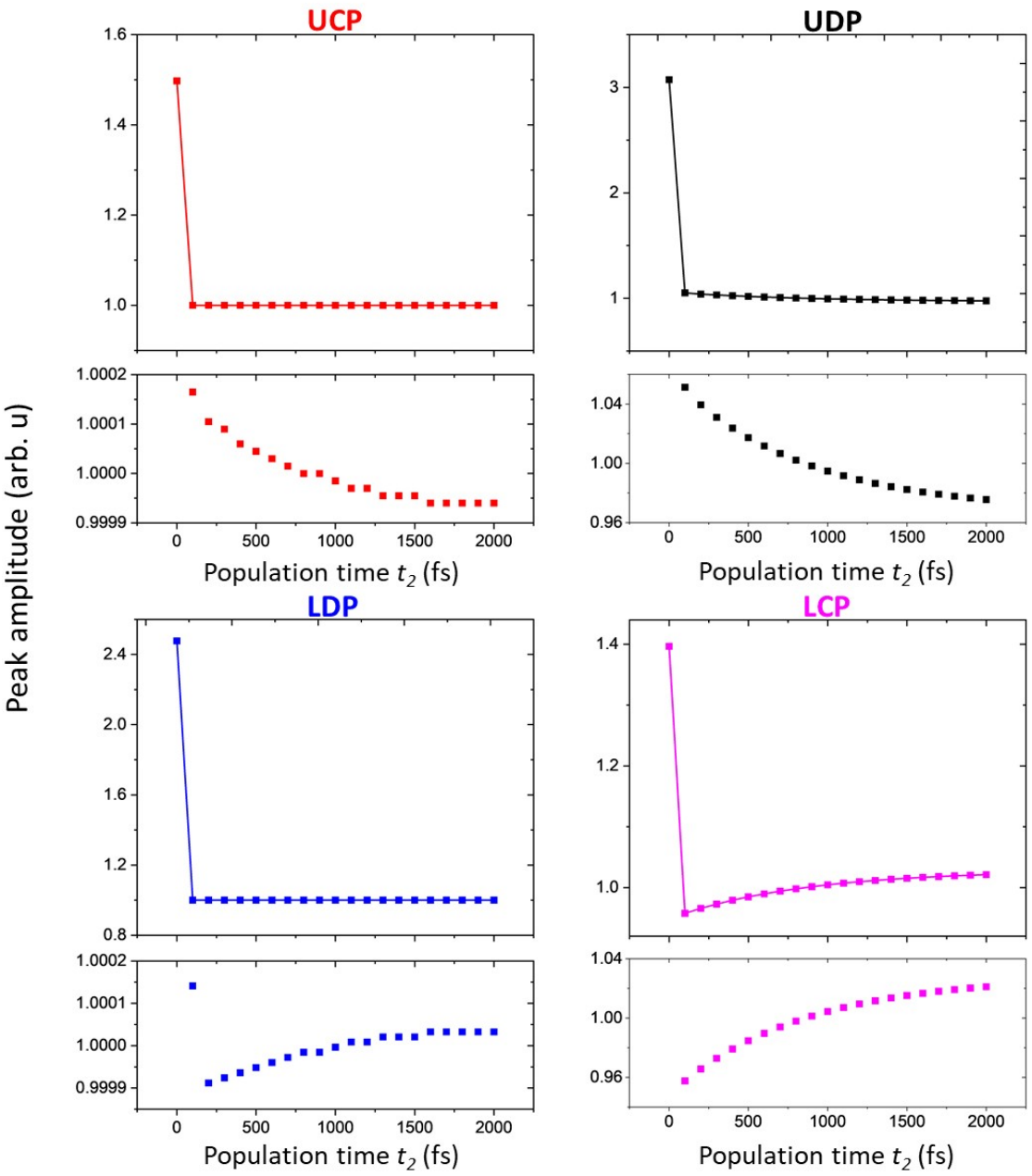

Figure 4.5: Time traces calculated from the simulated F-2DES spectra shown in Fig. 4.3 (b) by integrating the signal within the squares marked on the t_2=0 fs plot. The intitial drop from t_2=0 is in agreement with the experimental data. The weak rise and decay of the LCP and UDP respectively are also qualitatively similar to the experimental data.

4.5 Discussion

The data presented in Fig. 4.4 clearly illustrate that, in contrast to C-2DES, F-2DES of LH2 shows very little spectral evolution as a function of the waiting time. In particular, the kinetics of energy transfer from B800 to B850 are difficult to discern in F-2DES, constituting a $\sim$5 % change in the signal level of the LCP, compared to $\sim$100 % in C-2DES. The rise in the LCP in the F-2DES data occurs with a time constant of 1345 $\pm$ 575 fs, consistent with the B800-B850 energy transfer process reported in prior work [58] and with our C-2DES measurement of 825 $\pm$ 10 fs. The substantially smaller relative kinetic signals in F-2DES compared to C-2DES means that high signal averaging and a stable experimental setup is required for resolving LH2 energy transfer kinetics with F-2DES.

Bolzonello et al. recently presented theoretical studies of action-detected 2DES of molecular assemblies [6], finding that the information about excited-state dynamics is reduced as the number of chromophores increases. This is a consequence of the output signal intensity not being proportional to the number of excitations generated in the system, which can arise from exciton-exciton annihilation or indirect effects in the signal generation or detection. Bolzonello et al. present a compelling combinatoric argument that clearly demonstrates that the SE signal, which reports on the excited-state dynamics, scales unfavorably compared to the GSB signal with increasing system size. In Fig. 4.6 we present double-sided Feynman diagrams that depict the signals that contribute to the UDP and LCP, the features sensitive to the

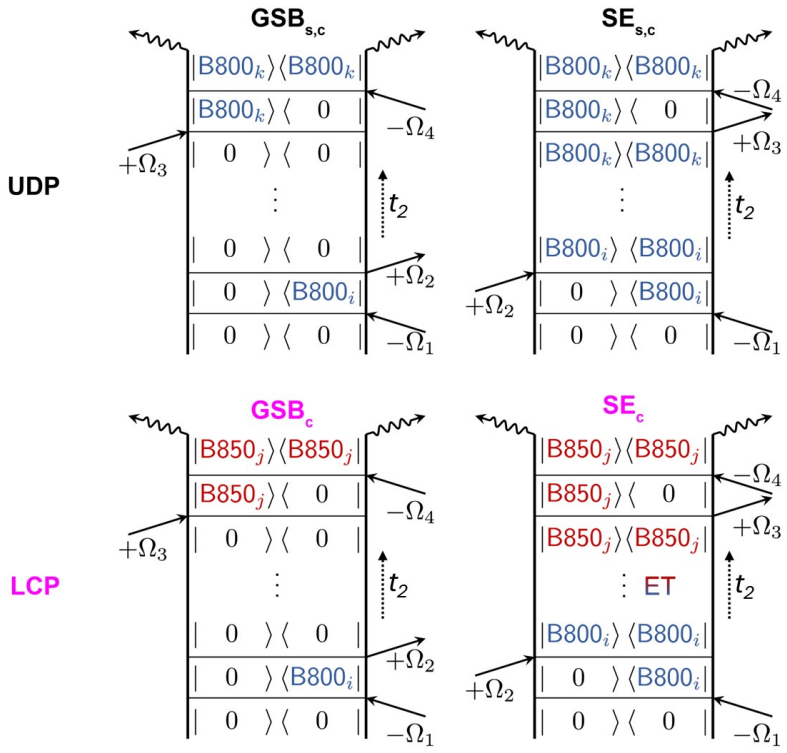

Figure 4.6: Double-sided Feynman diagrams depicting the signals that contribute to the upper diagonal peak (from B800) and the lower cross peak (LCP) which exhibits B800 to B850 energy transfer (ET) during waiting time T. The subscripts "s" refers to "self" diagrams in which the first pulse pair and the last pulse pair both interact with the same state. In contrast, the "c" refers to "cross" diagrams in which the first and last pulse pairs interact with different states

B800-B850 energy transfer, of the F-2DES spectrum. We ignore the two oppositely-signed ESA contributions (shown in the appendix, Fig. 4.7 and Fig. 4.8) because our prior work showed that these cancel in LH2 [71] due to the long fluorescence lifetime and efficient exciton-exciton annihilation. Following the terminology and combinatorial reasoning of Bolzonello et al. we distinguish between "self"-population pathways "s", in which the four pulses interact with the same state, and "cross"-population pathways "c", in which each pair of pulses interacts with different states. For this simple combinatoric argument we consider the system to be weakly coupled, such that the site basis is appropriate. We later discuss the implications of excitonic coupling. The ratio of SE pathways to GSB pathways is of particular importance, as only the

SE pathways contain information about the dynamics (assuming ESA cancellation).

The UDP has contributions from GSB and SE as shown in Fig. 4.6 (top). In the SE_s and GSB_s pathways, both pulse pairs interact with the i^{th} B800 pigment ($i = k$), leading to a total of $N_{B800} = 9$ SE_s and GSB_s pathways each (where N_{B800} is the number of pigments on the B800 ring). In the SE_c and GSB_c pathways ($i \neq k$), the initial pulse pair interacts with the i^{th} B800 pigment, while the second pulse pair interacts with the k^{th} B800 pigment. In the case of the UDP, SE_c is indicative of intraband energy transfer. The spectroscopic signatures of interband energy transfer, i.e., a rise of the LCP and a decay of the UDP, are connected only to the SE pathways since only these pathways include an excited state population during the waiting time t_2. In the case of SE_c, interband energy transfer can occurs during waiting time t_2. However stimulated emission must occur from whichever pigment is in the excited state at the time of the third light-matter interaction (the k^{th} pigment), therefore there are still only 9 SE pathways. In contrast, in all GSB diagrams the system remains in the ground state during t_2, leading to $N_{B800} * (N_{B800} - 1) = 9 * 8 = 72$ GSB_c pathways. Assuming equal contributions from all pathways, for the UDP, the ratio of SE/GSB = 9/(9+72) = 11 %.

The LCP consists of diagrams in which the first pulse pair interacts with the i^{th} pigment on the B800 ring, while the second pulse pair interacts with the j^{th} pigment on B850 ring as shown in Fig. 4.6 (bottom). Since all "self" pathways produce signals on the diagonal, we only need to consider the SE_c and GSB_c contributions for the LCP. The SE_c pathways clearly exhibit interband energy transfer from B800 to B850 during the waiting time t_2, resulting in a rise in the LCP amplitude. In addition to the SE_c pathways, an even larger number of GSB_c pathways exist that contribute to the LCP. In the limit of negligible coupling, where we consider inde-

pendent excitations on the pigments of the B800 and B850 rings, the number of SE_c pathways would be $N_{B800} = 9$. In contrast, the number of GSB_c pathways would be $N_{B800} * N_{B850} = 9 * 18 = 162$ where N_{B850} is the number of pigments on the B850 ring. If all pathways are equally weighted, the fraction of signal showing kinetics would be given by $SE_c/GSB_c = 9/162 = 0.056 = 5.6$ % of the signal. This is in quite good agreement with the data shown in Fig. 4.4 (d) in which the exponential rise due to B800-B850 energy transfer constitutes ∼6 % of the signal.

In LH2, rather than independent pigment excitations, non-negligible electronic coupling results in the manifold of B800 and B850 exciton states. The vastly higher oscillator strength of a small number of exciton states means that the different pathways need to be weighted differently (Fig. 4.2 (a). This changes the effective number of excitons since only the bright excitons would participate in energy transfer. Thus, the ratio of SE to GSB pathways discussed above becomes dependent on the levels of delocalization within a system.

Given the difficulty in observing kinetics in multichromophoric systems with F-2DES, the question arises as to what, if any, systems and questions are better-suited to action-detected spectroscopies compared to their coherent counterparts. This issue has also been discussed by Bolzonello et al. [6]. We note that F-2DES may offer some advantages in studies of systems with broad ESA signals, such as the bacterial reaction center or the D1D2-cytb559 photosystem II reaction center. Separated from their antenna complexes, these systems contain a small number of pigments. Understanding their excitonic structure in the low energy Q_y region has been challenging due to a combination of disorder and spectral overlap of constituent pigments. Attempts to leverage distinct Q_x signatures of the pigments to untangle the Q_y excitonic structure have been complicated by the broadband ESA signals in the Q_x region [174]. We have

demonstrated that the oppositely-signed ESA pathways in F-2DES essentially cancel for LH2, revealing clean GSB signatures [71]. Such ESA suppression may make broadband F-2DES measurements useful for probing excitonic structure.

In conclusion, using LH2 as an illustrative example, our study demonstrates the need for careful consideration of the system characteristics and the questions of interest in selecting between coherent and action-detected modalities. For observing energy transfer in LH2, C-2DES offers a clear advantage over F-2DES. Future experimental advances, such as time-gating the fluorescence signal in F-2DES [71, 73] could allow for isolation of the SE signals, as could the recently-proposed 2D-FLEX method [175].

4.6 Materials and Methods

The LH2 samples from *Rbl. acidophilla* were prepared following established protocols [176] that are described in detail in the Appendix. Our experimental setup for the F-2DES measurements is based on the acousto-optic phase modulation and lock-in detection scheme first demonstrated by Tekavec et al [74], and used previously by us [70, 130]. The implementation is described in Chapter III and the setup layout shown in Fig. 3.1 with the "FM up" geometry. The pulse energies used were 22 pJ and spot sizes were 16 μm, exciting 10 % of the sample at each laser shot. Sample OD used was ~ 0.33. The sample was flowed at 96 mL/min to reduce photobleaching effects. The t_1 and t_3 delays were scanned from 0 to 91 fs, in steps of 7 fs, while t_2 was scanned from 0 to 2000 fs. A lock-in time constant of 100 ms was used in the measurements and the signal at each combination of the three delays was averaged over 60 acquisitions corresponding to an acquisition time of 8 min per spectrum. The C-2DES measurements were made in the pump-probe geometry as reported previously [104]. The pump pulses had a total pulse energy of 7.3 nJ and were focused

to 190 μm at the sample position, whereas the probe pulse had a pulse energy of 2.5 nJ and was focused to 180 μm. The t_1 delay was scanned from 0 to 180 fs, in steps of 5 fs, in the partially rotating frame with $0-\pi$ phase cycling. For the B800-B850 energy transfer kinetics, t_2 was scanned from -100 to 5000 fs in 100 fs steps. Each t_2 spectrum was collected in ∼1.5 min, requiring ∼90,000 total laser shots. More details about the C-2DES setup are provided in the Apprendix.

4.7 Appendix

4.7.1 F-2DES: Double-sided Feynman Diagrams

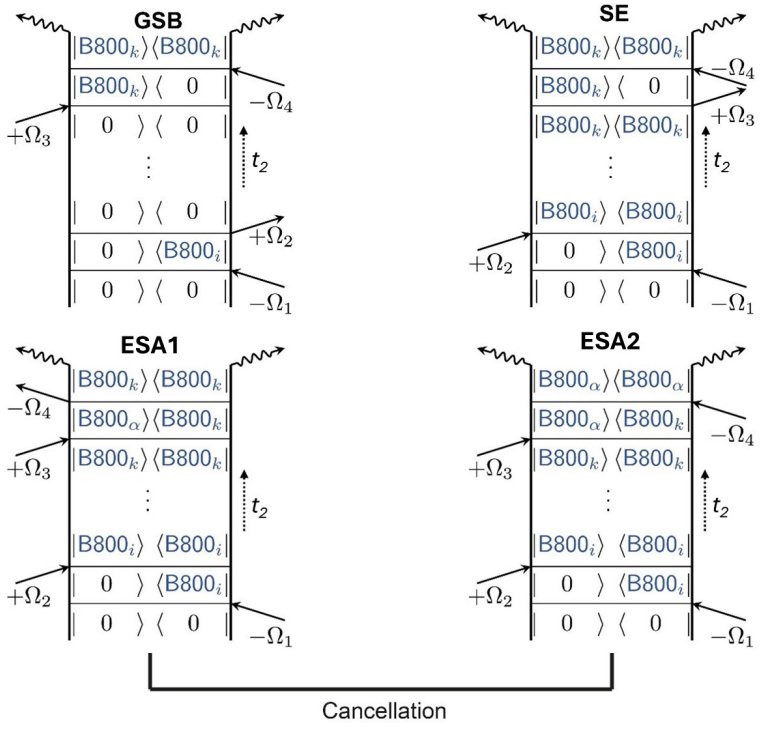

Figure 4.7: All the double-sided Feynman diagrams corresponding to the UDP for rephasing pathways are shown. The pathways with coherences during the waiting time t_2 are not shown. ESA2 pathway corresponds to the signal emitted from the second excited state of B800 ($|B800_\alpha\rangle$) and contributes with an opposite sign to the ESA1 pathway, which originates from the singly excited state $|B800\rangle$. In case of LH2, ESA1 and ESA2 cancel out due to efficient EEA, revealing GSB and SE pathways.

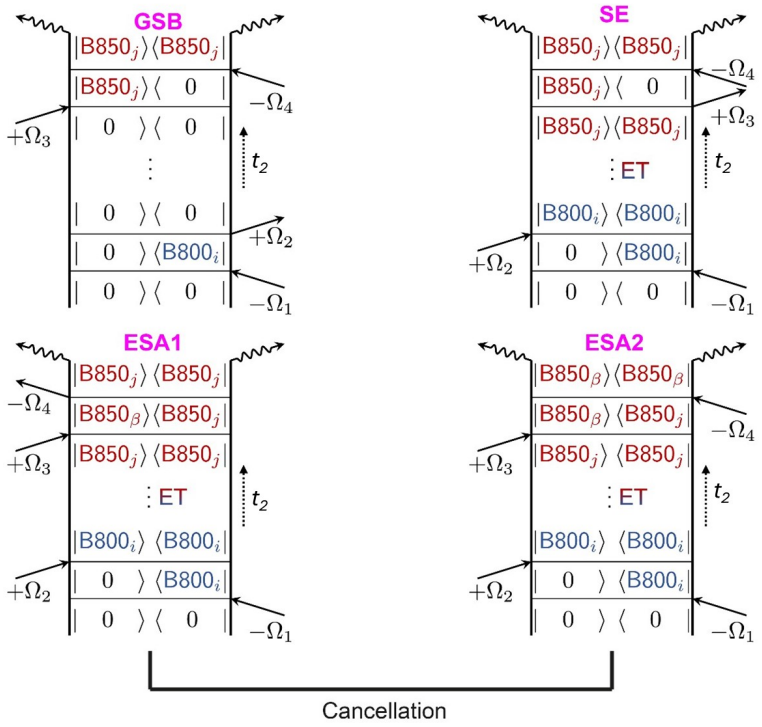

Figure 4.8: All the double-sided Feynman diagrams corresponding to the LCP for rephasing pathways are shown. The pathways with coherences during the waiting time t_2 are not shown. ESA2 pathway corresponds to the signal emitted from the second excited state of B850 ($|B850_\beta\rangle$) and contributes with an opposite sign to the ESA1 pathway, which originates from the singly excited state $|B850_\mathrm{J}\rangle$. Efficient EEA leads to complete cancellation of ESA1 and ESA2 pathways.

4.7.2 C-2DES experimental setup

For the C-2DES experiments, a Ti:Sapphire regenerative amplifier (Spectra Physics Spitfire Pro, 1kHz, 35fs pulse duration) was used to pump a home-build degenerative optical parametric amplifier (DOPA), generating near-infrared pulses from 700-930 nm. The output of the DOPA is split 80/20 into the pump and probe, which are partially compressed with chirped mirrors (pump: -3000fs^2, 700-900nm, Femto Optics; probe: -280fs^2, 570-1040 nm, Layertec). The pump is coupled into an acousto-optic pulse shaper (Dazzler, Fastlite), which is used to fully compress the pump to 11 fs and generate the pump pulse pair with controllable time delay t_1 and relative carrier envelope phase (ϕ_{12}). The Dazzler also enables the time delay t_1 to be scanned in

the rotating frame by applying a time dependent carrier envelope phase. The probe was fully compressed to 11 fs with an SLM-based pulse shaper (Bio-photonics solutions). To vary the waiting time t_2, the pump pulse pair traveled through a delay stage (Thorlabs DDS220). The pump and probe pulses were focused onto the sample in the pump-probe geometry using a curved mirror (f=250 mm). At the sample position, the pump and probe spot sizes were 190 μm and 180 μm respectively. The probe was coupled into a monochromator (Horiba iHR320, grating: 600 g/mm) and focused onto a CCD camera (Princeton Instruments Pixis 100). To ensure the C-2DES experiments were collected in the annihilation free regime, we measured the pump-probe signal vs pump power. The pump and probe energy used were 7.3 nJ (at t_1=0) and 2.5 nJ, respectively. The time delay t_1 was scanning in the partially rotating frame with a reference wavelength of 1000 nm from 0 to 180 fs in 5 fs such that the Nyquist sampling condition was met. To resolve the initial fast decay of the B850 diagonal peak (LDP), the waiting time t_2 was scanned from -100 to 500 fs in 10fs steps. To resolve the energy transfer from the B800 diagonal peak (UDP) to the B800-B850 cross peak (LCP), the waiting time t_2 was scanned from -100 to 5000 fs in 100 fs steps. All the C-2DES data was collected with all parallel polarizations. The same LH2 sample was used for the C-2DES and the F-2DES measurements. However, the concentration was increased for the C-2DES measurements such that the OD was 0.38 in a 0.2 mm pathlength flow cell. During the experiments, the sample was flowed with a peristaltic pump to prevent photobleaching. No photobleaching over the experiment was observed by comparison of the absorption spectrum before and after the C-2DES experiments.

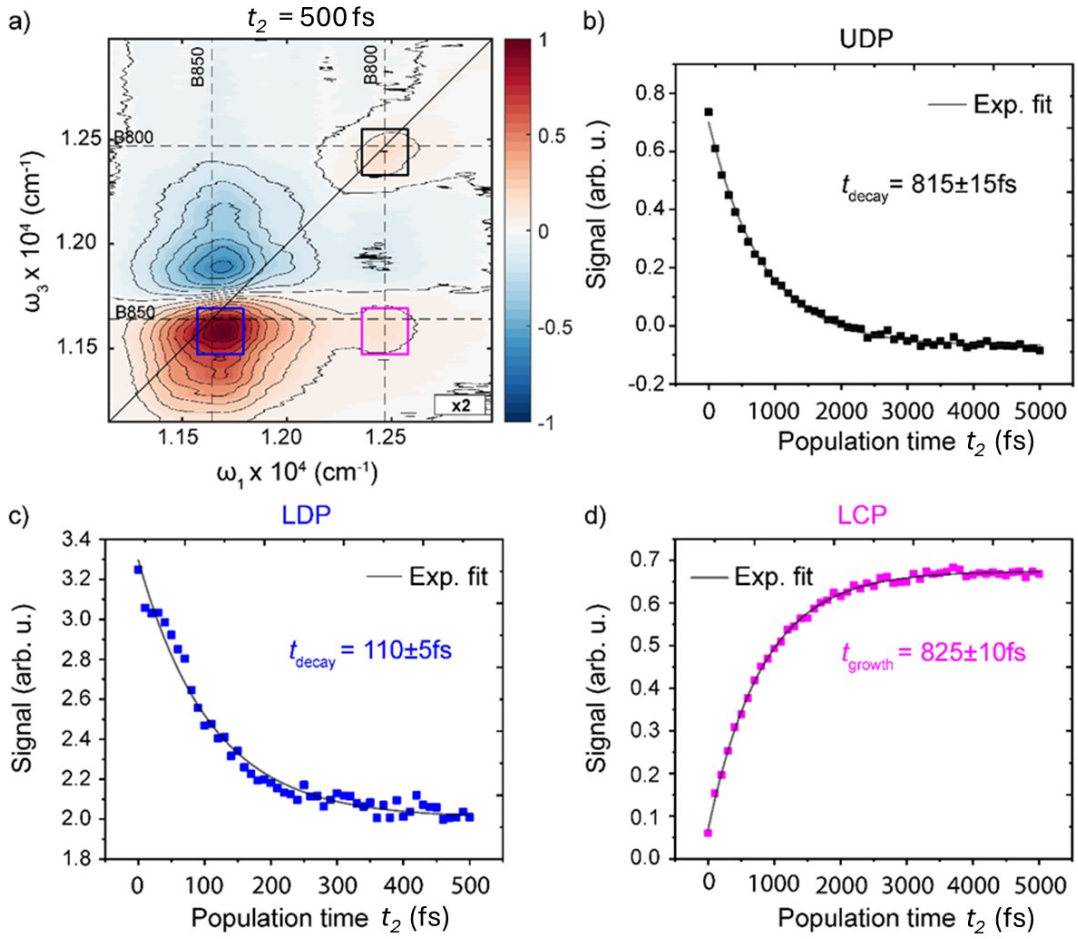

Figure 4.9: C-2DES of LH2. a) C-2DES spectrum at a population time of 500 fs. The squares mark the areas for averaging to obtain the corresponding traces. b) Decay and exponential fit (solid) of the UDP. A decay time constant $t_{decay} = 815 \pm 15$ fs is obtained. c) Exponential decay of the LDP and exponential fit (solid blue line). A fast decay time constant of 110 ± 5 fs is obtained. d) Exponential rise and exponential fit (solid magenta line) of the LCP. The fit yields a time constant $t_{growth} = 825 \pm 10$ fs.

4.7.3 Sample preparation

Cells of *Rbl. acidophilla* strain 10050 were grown anaerobically in C-succinate media at 30°C under anaerobic conditions at a light intensity of ∼100 μmol photons $s^{-1}m^{-2}$. The fully grown culture was pelleted, washed once with 20 mM MES, 100 mM KCl, pH 6.8 to remove media traces and the cell pellet either used immediately or flash frozen until required. The *Rbl. acidophilla* cells were re-suspended in 20 mM

Tris-Cl pH 8.0, homogenized thoroughly with a few grains of DNAse and a few mg of $MgCl_2$. The cells were broken by passage three times through an Emulsiflex-CS cell disrupter and the sample immediately ultra-centrifuged (180,000 $\times$ g, 90 min, 4°C) to pellet the membranes. The supernatant was discarded and the membranes gently re-suspended with 20 mM Tris-Cl pH 8.0 and adjusted to an optical density (OD) at the Q_x maxima (approx. 580 nm) of 50 cm^{-1}. The membrane suspension was solubilized at room temperature with gentle stirring for 1 h with 1% N, N-dimethyldodecylamine N-oxide (LDAO) and then centrifuged (100,000 x g, 30 min) to remove any un-solubilized material. The solubilized, supernatant fraction was fractionated using stepwise sucrose density centrifugation (150,000 $\times$ g, 4°C, 16 h). The LH2 complex band was gently removed from the gradient, loaded on an anion-exchange gravity column with ToyoPearl 650S resin (Tosoh) and eluted with increasing concentrations of NaCl in TL buffer (20 mM Tris-Cl, 0.1% LDAO, pH 8.0). The resulting fractions were assayed spectrophotometrically for purity and the best pooled, concentrated and run on a Sephacryl S-300 (GE Healthcare) size-exclusion column. The best fractions (Abs_{858nm} nm/Abs_{275nm}) = 3.2 were pooled, concentrated and flash frozen until required.

CHAPTER V

Excitation Energy Transfer in the dLH-RC Complex from *Gemmatimonadetes phototrophica* Using Fluorescence-Detected Two-Dimensional Electronic Spectroscopy

5.1 Introduction

G. phototrophica or AP64 is the first phototrophic member of the phylum Gemmatimonadetes, only recently discovered in 2011 from a freshwater lake in the Gobi desert, China [19]. It has been revealed that AP64 acquired its phototrophic nature as a result of horizontal gene transfer from purple bacteria through a mechanism that is not yet clear to the photosynthesis community [25]. Therefore, like purple bacteria, it is an interesting system that can help us gain insights into the mechanims of energy and charge transfer during the process of photosynthesis. Furthermore, it is a remarkable system from an evolutionary standpoint and could be a helpful system to potentially reprogram heterotrophic bacteria for light-powered metabolic processes [65]. So far, only one spectroscopic study focusing on energy transfer within the photosynthetic core complex dLH-RC of AP64 has been reported [5]. In this chapter, we report F-2DES meaurements on the dLH-RC complex and provide a comparative

outlook with the results on LH2 discussed in Chapter IV. Due to the difficulties with resolving kinetics using F-2DES, these results are preliminary and will be complemented by future C-2DES measurements.

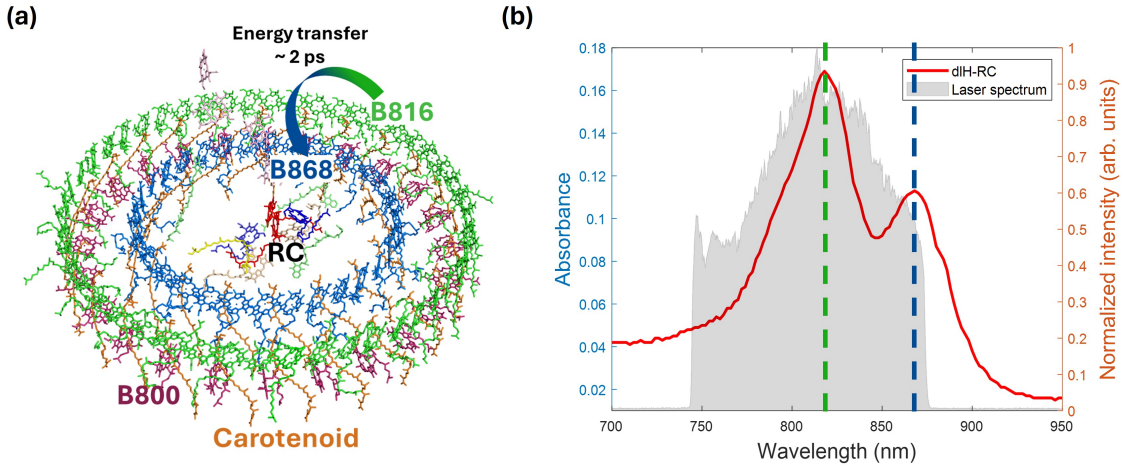

Figure 5.1: (a) Crystal structure of the dLH-RC complex from *(a) Gemmatimonadetes phototrophica* (strain AP64). It is made up of two concentric rings. The outer ring, named LHh consists of 24 subunits, with 24 dimeric BChl *a* units in the B816 ring and 24 monomeric BChl *a* units in the B800 ring. The inner ring is LH1, consisting of 16 subunits in the B868 ring, containing a total of 32 BChl *a* molecules. The energy transfer, with a reported time of ∼2 ps, from B816 to B868 is depicted. Together, LHh and LH1 make up the antenna component of the dLH-RC complex. Figure obtained from Protein Data Bank Library 7o0u [5] using PyMOL. (b) Room temperature UV-Visible absorption (red line) of dlH-RC complex suspended in 20 mM Tris-Cl buffer mixed with 0.02 % β-DDM (*n*-dodecyl β-D-Maltoside). The two absorption peaks corresponding to B816 and B868 are marked with green and blue lines respectively. The absorption corresponding to B800 is barely evident. The laser spectrum used to conduct the measurements is shown in gray.

The crystal structure of dLH-RC from AP64 (shown in Fig. 5.1 (a)) was reported in a recent study [5]. It consists of an RC at the center and is surrounded by two concentric rings. The inner LH1 ring consists of 16 pairs of $\alpha\beta$ heterodimers and is found to be similar to the LH1 found in LH1-RC complexes [67, 68]. It contains a total of 32 BChl *a* pigments. The outer LHh ring is made up of 24 heterodimeric $\alpha\beta$ subunits and performs a similar role to LH2 in the dlH-RC complex. Two distict rings form

LHh complex - B816 consisting of 24 BChl *a* dimers and B800 consisting of 24 BChla *a* monomers. Fig. 5.1 (b) shows a room-temperature UV-visible absorption spectrum of dlH-RC complex suspended in 20 mM Tris-Cl buffer mixed with 0.02 % β-DDM (*n*-dodecyl β-D-Maltoside). The B868 and B816 absorption peaks are marked at the corresponding positions with green and blue lines. We note that the B800 absorption does not show up prominently because of overlap with the B816 band.

The B800 in dLH-RC complex lies 18.5 Å from the B816 ring, similar to the distances found between B800 and B850 in the LH2 complexes from purple bacteria [27, 28]. Distance between the LHh and LH1 rings is 24 to 26 Å, enabling fast energy transfer to B868. From their transient absorption studies on the dLH-RC complex, Qian et al [5] found an energy transfer timescale of ∼2 ps between the B816 and B816 rings, much faster than the 3-5 ps energy transfer between LH2 and LH1 rings in purple bacteria [14].

5.2 Experimental methods and materials

We received the AP64 dlH-RC complexes from our collaborator Alastair T. Gardiner. The *G. phototrophica* cells were cultivated and purified by them, as outlined in [5]. The AP64 cells were streaked on agar plates. To optimize the expression of photosystem complexes, the inoculated plates were incubated under microaerophilic conditions with 10% O_2 + 90% N_2 at 28 ± 1°C under dark light conditions for 2 weeks. The resulting grown cells were scraped from the plates and stored at ∼20°C for future use.

The harvested cells were suspended in 20 mM tris-Cl and 50 mM NaCl (pH 8). A few grains of deoxyribonuclease and a few milligrams of $MgCl_2$ were used to homogenize the suspension. An Emulsiflex-CS cell disrupter was used to break the

cells by passage three times. The unbroken cells were removed by centrifuging at 12000g, 4°C for 10 min. The membranes were then pelleted with the help of an ultracentrifuge (180000g, 4°C) in 120 min and then resuspended jn 20 mM tris-Cl (pH 8). After this, they were adjusted to an optical density of 10 cm^{-1} at the Q_x band. Then, they were solubilized in 2% β-DDM and 0.2% Triton X-100 by stirring at room temperature for 60 min, followed by centrifuging to remove non-solubilized materials. The solubilized sample was layered on a stepwise sucrose gradient to run for 16 hours (208000g, 4degC). The RC-dLH band was carefully removed from the sucrose gradient and transferred into a sintered-glass gravity column with ToyoPearl 650S anion-exchange resin (Tosoh). The RC-dlH complex was eluted with the help of increasing NaCl concentrations in TD buffer and assayed spectrophotometrically to increase purity.

Gel filtration was preceded with pooling and concentration of the best fractions. Gel filtration was done with the help of TD buffer using a Knauer Azura system equipped with UV-visible-NIR diode array detector and a Superdex S-300 (1 m XK-16 column, GE Healthcare) column at a flow rate of 0.5 mL/min at 10 °C. A816/A260 absorption ratio ∼1.4 to 1.3 was used for pooling and concentration of the collected fractions of dLH-RC. The purity was analyzed using SDS-polyacryladmide gel electrophoresis. For our experiments, purified and concentrated dlH-RC complexes are suspended in 20 mM Tris-Cl buffer mixed with 0.02 % β-DDM, and diluted to an optical density of ∼0.17, measured in a 1 mm cuvette.

The experimental setup is shown in Fig. 3.1 and described in detail in Section 3.2 of Chapter III is used for the measurements. Similar settings were used as described for LH2 measurements in Chapter IV. The pulse energies used were 22 pJ and spot sizes were ∼16 µm, exciting∼6 % of the sample at each laser shot (assuming a similar

extinction coefficient as LH2). Sample was flowed at 96 mL/min to reduce photobleaching effects, and the temperature of the sample is maintained close to 0°C using an ice bath. The t_1 and t_3 delays were scanned from 0 to 91 fs, in steps of 7 fs, while t_2 was scanned from 0 to 3000 fs for the shorter measurement (Fig. 5.2 and Fig. 5.3) and from 0 to 10000 fs for the longer one (Fig. 5.4). A lock-in time constant of 100 ms was used in the measurements and the signal at each combination of the three delays was averaged over 60 acquisitions, corresponding to an acquisition time of ∼8 min per t_2 spectrum. The laser spectrum used in the measurements is shown in gray in Fig. 5.1 (b).

5.3 Energy transfer dynamics in dLH-RC

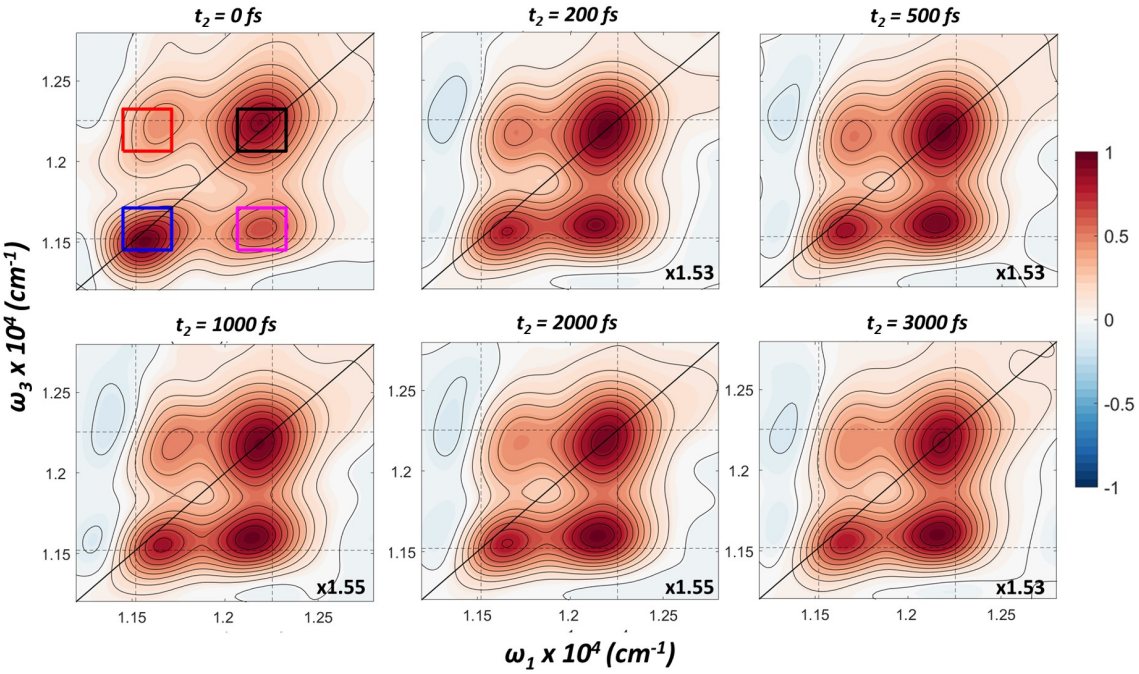

Figure 5.2: F-2DES spectra of the dLH-RC complex from AP64 at different waiting times, $t_2 = \{0, 200, 500, 1000, 2000, 3000\}$ fs. Each spectrum is normalized to the maximum amplitude of t_2=0 fs, and then scaled by an appropriate factor to normalize the amplitude in [-1, 1]. The t_2=0 spectrum is also overlayed with squares color-coded to the t_2 time traces shown in Fig. 5.3. Each square marks the area used for signal integration to yield the waiting time traces corresponding to each peak: Upper diagonal peak, UDP (black), Upper cross peak, UCP (red), Lower diagonal peak,

LDP (blue), Lower Cross Peak, LCP (magenta).

We investigate the evolution of the four different peaks on the 2D spectra through the waiting time t_2 to resolve the ultrafast energy transfer between B816 and B868. The upper cross peak (UCP), corresponding to excitation at 816 nm and detection at 868 nm is expected to grow on the timescale of energy transfer between B816 and B868. Concurrent to this rise, there should be a decay in the upper diagonal peak (UDP) at 816 nm. Time traces from a measurement where t_2 is scanned from 0 to 3000 fs, are shown in Fig. 5.3. In Chapter IV, we showed with experiments and theory that the evidence of energy transfer during t_2 can be strongly suppressed in F-2DES measurements compared to C-2DES due to detection-time t_4 (refer to Fig. 2.3 (b)) dynamics, since the timescale for fluorescence emission ($\sim$ns) is much longer compared to the coherent signal emission ($\sim$ps). In addition, the fourth pulse interaction leads to an additional ESA II pathway, which largely cancels the ESA I pathway in systems like LH2 due to effective EEA. Surprisingly, the LCP amplitude rise in case of AP64 is more evident than what we observed in LH2. We believe that the basic structural differences between LH2 and dLH-RC (consiting of both LHh and LH1 rings) may be responsible for this contrast. We fit the LCP and UDP with single exponentials. All the traces shown in Fig. 5.3 are normalized to their maximum peak amplitude among the $t_2 > 0$ points. The LCP is fit to an exponential of the form $y = y_1 - A_1 e^{-t_2/t_{growth}}$. Approximately 11.5 % rise (compared to $\sim$5 % in case of LH2), given by A_1/y_1, is observed and a time-constant of 890 $\pm$ 340 fs is obtained for the growth of the CP. The UDP is fit to an exponential function of the form $y = y_2 + A_1 e^{-t_2/t_{decay}}$. The decay, given by A_2/y_2, is $\sim$7 % (compared to $\sim$3 % for LH2) and determined decay time-constant is $t_{decay=}$ 1260 $\pm$930 fs. With the uncertainty in the determined time-constant, the results seem to agree with the reported time constant of 2 ps reported by Qian et al [5]. Similar to the decay in the first 400 fs

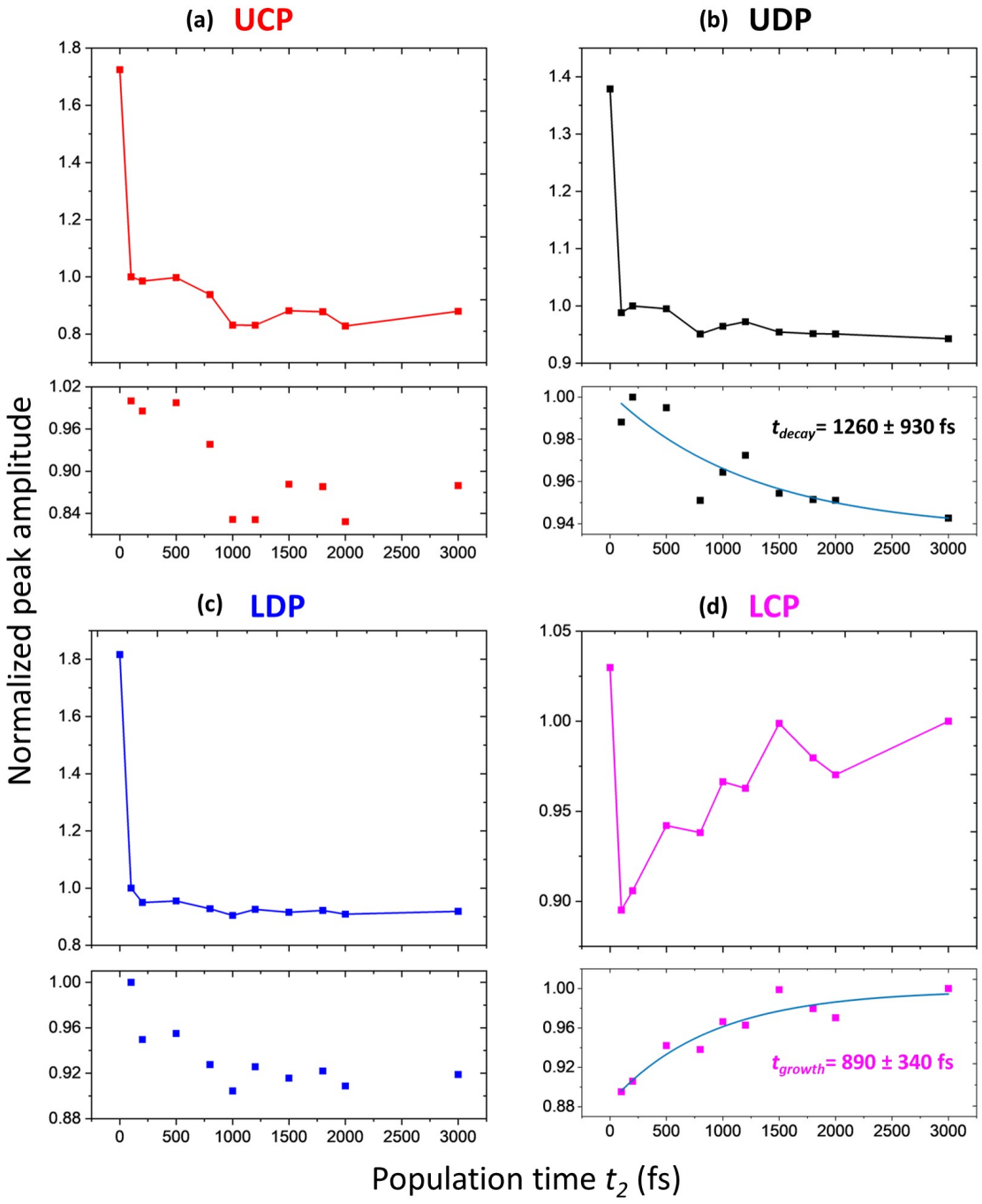

Figure 5.3: Traces corresponding to the four peak positions marked with color-coded squares on the t_2=0 fs spectrum in Fig. 5.2. The top panels in each of the figures (a)-(d) show the full traces from t_2=0 to 3000 fs. The lower panels show the traces from the upper panels, plotted only from t_2=100 to 3000 fs to highlight peak dyanamics. (a) The UCP exhibits a decay in the first 1000 fs, in contrast to no dynamics observed for the case of LH2. (b) The LDP shows fast decay in the first 500 fs, which we attribute to fast relaxation within the B868 ring. Exponential fits for the (b) UDP

and (c) LCP are shown, with a decay time constant of $t_{decay} = 1260 \pm 930$ fs for the UDP and a growth time constant of $t_{growth} = 890 \pm 340$ fs for the LCP. Each peak trace was normalized to the maximum peak amplitude for $t > 0$ fs.

of the lower diagonal peak (LDP) corresponding to B850, we observe that the B868 peak shows a fast decay under 500 fs, implying that fast relaxation occurs in the strongly coupled B868 manifold. We see a decay in the upper cross peak (UCP), as opposed to the expected trend and observed UCP dynamics from LH2 where after the initial drop in the amplitude from t_2=0, the peak amplitude stays more or less constant, while only exhibiting slow lifetime decay. The reason behind the apparent fast LCP decay is not obvious, although we see a faster decay in all the peaks after about 2 ps. This might mean a faster lifetime decay, contributing to the observed LCP amplitude decay.

Traces from a longer scan (t_2 =0 to 10000 fs) are shown in Fig. 5.4 to highlight the lifetime decay. Much longer scans (over a ns) are required to quantitatively determine the lifetime decay, but due to longer measurement times (and hence noisier data) and mechanical stage length limitations (going only up to 800 ps), the required measurements were not successful.

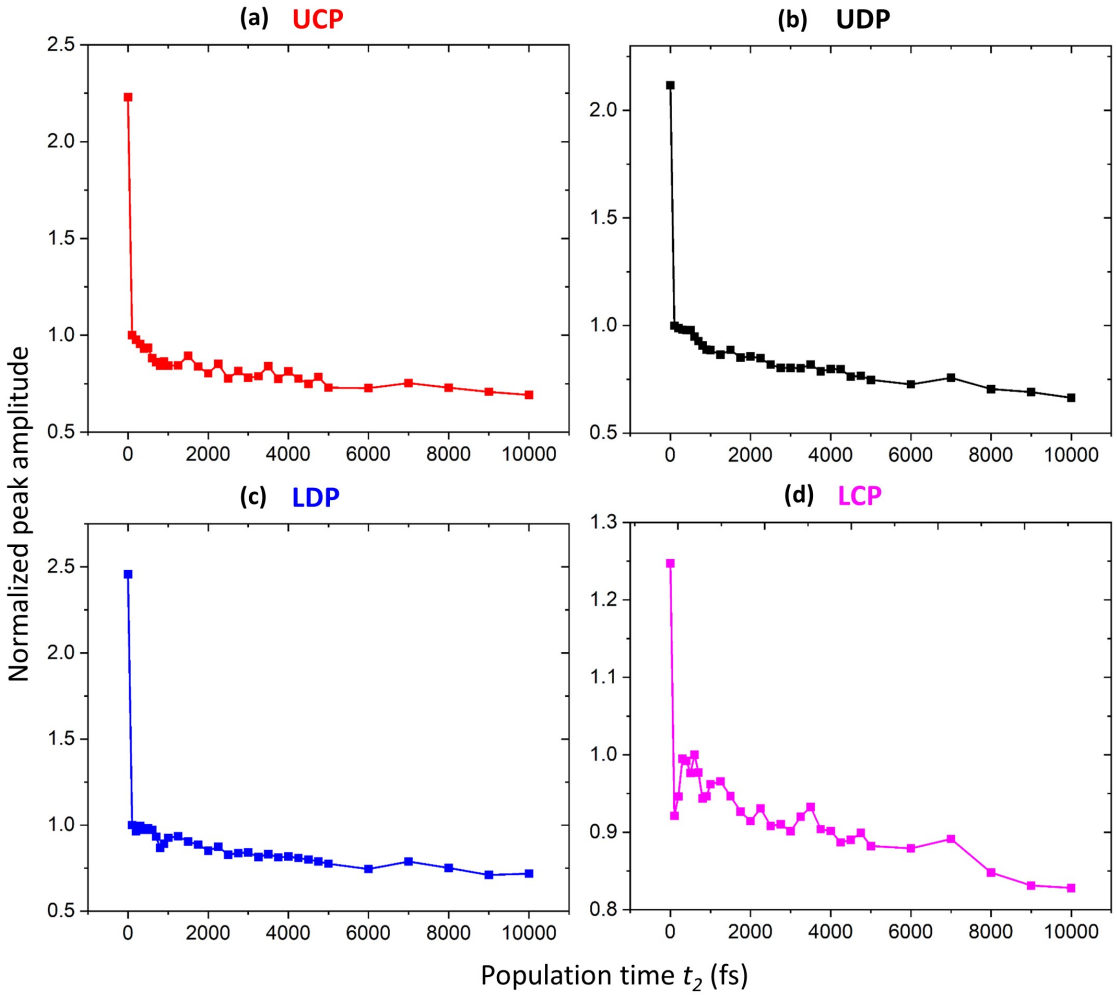

Figure 5.4: Peak traces for a long scan, measured from t_2= 0 to 10000 fs. The shorter time dynamics shown in Fig. 5.3 are also evident in the longer scans. An overall decrease in the signal over a longer span highlights the lifetime decay. Traces from a single measurement are shown. Each peak trace was normalized to the maximum peak amplitude for $t > 0$ fs.

5.4 Discussion and conclusion

The more evident rise in the LCP and decay in the UDP from dLH-RC compared to LH2 is quite interesting. For the LCP one would expect a further decrease in the SE contributions relative to GSB according to $1/N_{B868} \sim 3.1$ % in the extreme case of no delocalization in the B868 ring (N_{B868} =32). However, we observe a rise almost thrice (∼11%) this predicted limit. This may be explained by a higher level of exci-

tonic delocalization in B868 which would reduce N_{B868}, where N_{B868} is the number of excitonic units participating in energy transfer. For the UDP, the lower limit is close to 2 %, given by $1/N_{B816}$, where N_{B816} =48. From our results, we observe an amplitude decay also at thrice ($\sim$7 %) the limit. These preliminary results indicate that the kinetics of energy transfer are more readily observed in F-2DES measurements of dLH-RC compared to LH2. The underlying reason for this difference is unclear and requires further investigation. Indeed, different levels of delocalization will arise from different orientations and distances between the pigments in the participating rings. Future work will examine the LHh to LH1 energy transfer in AP64 and compare this to the LH2 to LH1 in purple bacteria.

We recognize that our preliminary results need to be supported by further modeling of the AP64 excitonic structure and futher experimental measurements. Spectroscopic methodologies like C-2DES will be a non-ambiguous way to quantify the energy transfer and relaxation timescales. As we showed in Chapter IV, the energy-transfer signatures show up more strongly with C-2DES and are therefore less prone to noise over a t_2 scan. Alternatively, rapid-scanning F-2DES measurements, enabling less accumulation of noise over a single t_2 scan, along with higher averaging could improve the signal-to-noise ratio of the measurements. A methodology for faster 2D measurements (for a single t_2) along t_1 and t_3 is presented in the next chapter, and could be easily extended to rapid scanning along all three delays, with the limitation of being computationally time-consuming [177].

CHAPTER VI

Phase-Modulated Rapid-Scanning Fluorescence-Detected Two-Dimensional Electronic Spectroscopy

This chapter is adapted from our published articles, entitled "Phase-Modulated Rapid-Scanning Fluorescence Detected Two-Dimensional Electronic Spectroscopy," by Damianos Agathangelou, Ariba Javed, Francesco Sessa, Xavier Solinas, Manuel Joffre, and Jennifer P. Ogilvie [177, 178].

6.1 Abstract

We present a rapid-scanning approach to fluorescence-detected two-dimensional electronic spectroscopy (F-2DES) that combines acousto-optic phase-modulation with digital lock-in detection. This approach shifts the signal detection window to suppress 1/f laser noise and enables interferometric tracking of the time delays to allow for correction of spectral phase distortions and accurate phasing of the data. This use of digital lock-in detection enables acquisition of linear and nonlinear signals of interest in a single measurement. We demonstrate the method on a laser dye, measuring the linear fluorescence excitation spectrum as well as rephasing, non-rephasing, and absorptive fluorescence-detected two-dimensional electronic spectra.

6.2 Introduction

Two-dimensional Fourier transform spectroscopy is now a widely used tool for probing structure, dynamics, and fluctuations that are obscured in linear optical spectroscopies, enabling new insights into the structure and function of complex molecules, aggregates, and materials [80]. The approach borrows from early multidimensional Fourier transform nuclear magnetic resonance (NMR) spectroscopies [179]. The most commonly used Fourier transform approaches use time-delayed pulse pair replicas created with interferometers. For multidimensional Fourier transform spectroscopic measurements at optical frequencies, this requires interferometric precision with path length stabilities of ~$\lambda/100$ to obtain reliable frequency axes and the separation of complex signal components with high signal-to-noise ratios [80]. To meet these challenges, a variety of approaches have been employed [96], including passive [107, 110] and active-phase stabilization [180] in various geometries ranging from fully noncollinear [80, 107, 110] to partially [103, 104] and fully collinear [72, 74, 117]. Other approaches have been developed to enable measurements in the rotating frame that reduce the Nyquist frequency and sensitivity to phase instability. Here, we demonstrate a phase-modulation-based approach to fluorescence-detected 2D Fourier transform spectroscopy using rapid scanning and digital lock-in detection. The approach enables simultaneous detection of complex linear and multidimensional signals and can be readily integrated into a microscope for spatially resolved measurements.

The phase-modulation approach was pioneered by Marcus and co-workers and used for wave packet interferometry [69] as well as fluorescence-detected [72, 74] and photocurrent-detected [123] two-dimensional electronic spectroscopy (2DES). Their approach has been adopted by a number of other groups for fluorescence-detected 2DES [70, 130, 181] and other action-based 2D measurements [120, 127, 168].

The phase-modulation approach, which has also been termed dynamic phase-cycling [120], is closely related to phase-cycling, which has been widely used in multidimensional spectroscopy [96, 101, 103, 104, 116, 117, 134, 182]. In phase-cycling, a pulse shaper is typically used to create a pulse sequence with the desired inter-pulse delays and relative phases. Multiple measurements recorded with an appropriate set of delays and phases are then combined to isolate the signal of interest. In contrast, in the phase-modulation approach, an Acousto-Optic Modulator (AOM) imparts a distinct radio frequency shift that modulates the pulse-to-pulse carrier–envelope phase shift. Linear and nonlinear spectroscopic signals of interest can then be isolated by detecting signals that are modulated at the appropriate frequency combination, through lock-in detection [69, 74], super-heterodyne mixing [183], or direct digitization followed by signal selection via Fourier transform analysis [181]. Phase-modulation and phase-cycling provide an alternative to phase-matching approaches that are commonly used to enable "background-free" detection of nonlinear signals. These approaches have the advantage that collinear pulses can be used, and since the coherent build-up of the signal is not required, the sample size can be small compared to the excitation wavelength [134]. This makes these methods appealing for spatially resolved measurements and studies of dilute samples.

The origins of phase-modulation-based Fourier transform spectroscopy can be traced back to the early work of Scherer et al. using phase-locked pulse pairs for fluorescence-detected wavepacket interferometry [184]. In their experiments, a piezo-mounted mirror was used in combination with a phase-locked-loop to maintain a fixed relative phase between pulse pairs while varying the inter-pulse time delay. This step-scan approach effectively transforms the measurement into the rotating frame, eliminating the high (optical) frequency modulation to isolate the rovibrational molecular

dynamics in molecular iodine. In contrast to the piezo-driven mirror approach of requiring a fixed relative pulse pair phase, the AOM-based phase-modulation method varies the relative pulse pair phase continuously at a well-defined frequency (see Fig. 6.1), avoiding the need for phase-locking or stabilization and enabling rapid scanning. By operating in the rotating frame, this approach to multidimensional spectroscopy reduces the necessity for high phase-stability interferometers.

To date, most AOM-based phase-modulation approaches to multidimensional spectroscopy have used step-scanning and lock-in detection referenced to carefully constructed frequency references to extract the signals of interest [69, 70, 72, 74, 120, 123, 127, 130, 181]. Karki et al. demonstrated that an AOM-based phase-modulation combined with the digital lock-in approach enables simultaneous detection of multiple multidimensional signals [181]. An alternative to step-scanning, in which the signal of interest is recorded at discrete delay times, is the continuous or rapid-scan approach. Both methods have widely been used in Fourier transform spectroscopy, and their relative benefits have been discussed in some contexts and depend strongly on the application and experimental implementation [185–187]. A continuous-scanning AOM-based phase-modulation approach to multidimensional spectroscopy was recently implemented by Autry et al. to simultaneously acquire multiple multidimensional spectra [183], employing a super-heterodyne mixing approach to isolate the signals of interest and a reference laser for interferometric tracking of the delays.

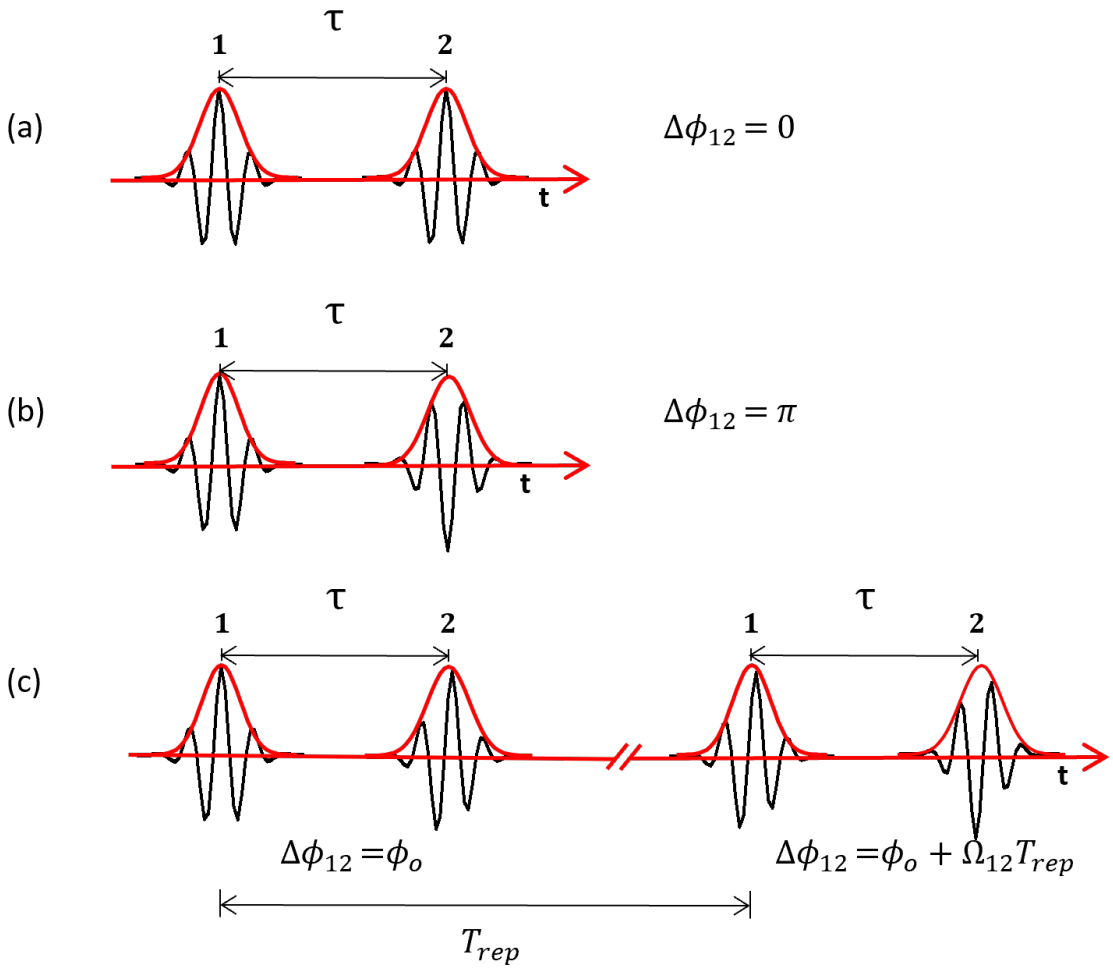

Figure 6.1: Pulse sequences used in Fourier transform spectroscopic measurements.(a) Standard approach employing a pulse pair generated by using an interferometer, resulting in two time-delayed pulse replicas with an identical carrier–envelope phase. (b) Pulse pair generated by using a pulse shaper, which can impart an arbitrary relative phase between the pulses (illustrated here with a π phase shift). (c) Phase-modulated approach in which the pulse pair is generated by using a Mach–Zehnder interferometer (MZ) with AOMs operating at distinct frequencies Ω_1 and Ω_2 in each arm, yielding a pulse pair with a relative phase that is modulated at $\Omega_{12} = \Omega_1 - \Omega_2$. Thus, the phase difference between the pulse pairs changes dynamically for consecutive pulses in steps of $\Omega_{12}T_{rep}$, where T_{rep} is the repetition rate of the laser

Here, we combine continuous-scanning with digital lock-in detection to acquire linear excitation, rephasing and non-rephasing F-2DES simultaneously with interferometric tracking of the delays, and accurate phasing in a single scan. In addition, we record the interferometric autocorrelation (AC), enabling us to characterize the

power spectrum and simultaneously obtain the fluorescence excitation spectrum.

6.3 Phase-Modulation and Continuous Scanning

In the phase-modulation approach to F-2DES, the phases of the four collinear pulses are modulated by using individual AOMs at four respective frequencies, Ω_1, Ω_2, Ω_3, and Ω_4. As a result, each pulse is tagged with a unique radio frequency Ω_i, which replaces the unique wavevectors, k_i, of a standard fully non-collinear 2DES experiment [72, 74]. In this case, the rephasing and non-rephasing signals arise from the four-wave mixing (FWM) populations, which modulate at the linear combination of radio frequencies of the individual pulses. Particularly, the frequency combinations $\Omega_R = -\Omega_1 + \Omega_2 + \Omega_3 - \Omega_4 = -\Omega_{12} + \Omega_{34}$ and $\Omega_{NR} = \Omega_1 - \Omega_2 + \Omega_3 - \Omega_4 = \Omega_{12} + \Omega_{34}$ correspond to rephasing and non-rephasing signals, respectively, where $\Omega_{12} = \Omega_1 - \Omega_2$ and $\Omega_{34} = \Omega_3 - \Omega_4$.

In the implementation of Tekavec et al. [74], the rephasing and non-rephasing signals are detected in parallel via phase-sensitive lock-in detection with respect to appropriate reference signals to select the signals of interest while rejecting other oscillatory and stationary fluorescence signals. The reference signals for lock-in detection are constructed by recording spectrally narrowed interference signals from MZ1 and MZ2, which modulate at Ω_{12} and Ω_{34}, respectively. Through detection relative to the reference wavelength, the signal is physically undersampled, making the measurement insensitive to phase noise caused by mechanical delay fluctuations in the interferometer arms, thus avoiding the need for active-phase stabilization.

In contrast to the approach of Tekavec et al. [74], rather than lock-in detection combined with step-scanning, we take a digital signal acquisition approach in combination with rapid scanning. Upon Fourier transformation of the time domain

fluorescence signal in post-processing, the signals of interest can be distinguished by their distinct modulation frequencies imparted by the AOMs. In addition to recording the phase-modulated fluorescence signal, we record other signals to enable interferometric determination of the time delays and accurate phasing of the spectra, and to retrieve the pulse power spectrum. We record a total of five signals while continuously moving the t_1 and t_1 delay stages: the four-pulse fluorescence signal $S_{4PF}(t)$, the two mixer signals $M_{12}(t)$ and $M_{34}(t)$, the four-pulse reference signal $S_{4Pref}(t)$, and the four-pulse interference (autocorrelation) signal $S_{4PAC}(t)$. The reference signal $S_{4Pref}(t)$, obtained after spectrally narrowing the four-pulse interference signal in a monochromator centered at frequency ω_{ref}, is used for the interferometric determination of t_1 and t_3. The two mixer signals $M_{12}(t)$ and $M_{34}(t)$ measure $\Omega_{12}(t)$ and $\Omega_{34}(t)$ respectively, and are generated by mixing appropriate signals from the AOM driver, enabling the tracking of any drifts in the AOM frequencies. Processing the linear components of $S_{4PF}(t)$ enables measurement of the linear fluorescence excitation spectrum, accurate determination of $t_1 = 0$ and $t_3 = 0$, and determination of the unknown spectral phase differences $\phi_{12}(\omega)$ and $\phi_{34}(\omega)$, which could result from minor misalignments or path length differences through the AOMs in the two arms of MZ1 and MZ2 respectively. Details of the data processing for determination of the interferometric delays t_1 and t_3, as well as $t_1 = t_3 = 0$, $\phi_{12}(\omega)$ and $\phi_{34}(\omega)$, are given in the Appendix (Sec. 6.9). These parameters are then used for the processing and accurate phasing of the F-2DES signals.

6.4 Experimental Methods

The experimental setup, shown in Fig. 6.2, is based on the original design by Tekavec and co-workers [69]. The pulse train from a 1 MHz ytterbium amplified laser (Spectra Physics Spirit-HE) is focused into a 4 mm thick Yttrium Aluminum Garnet

(YAG) crystal using a 5 cm focusing lens (L1), resulting in white-light generation (WLG). Re-collimation of the beam to a 3.7 mm diameter ($1/e^2$) is obtained using a 5 cm focal length lens (L2). A pair of short pass (SP 950 nm OD4, Edmund) and long pass optical filters (LP 650 nm OD4, Edmund) are used in order to spectrally narrow the pulse and reject the residual fundamental light. To ensure that the pulses are Fourier-transform-limited at the sample position, the beam is routed to a SLM-based pulse shaper (MIIPS 640P, Bio-photonic Solutions) for dispersion pre-compensation and further bandwidth reduction. After the pulse shaper, a 50/50 beam splitter (BS1, Newport, 10B20BS.2) splits the pulse energy equally and directs it to two Mach–Zehnder interferometers (MZ1 and MZ2) in order to generate the excitation and detection pulse pairs.

At the entrance of each interferometer, beam splitters (BS2 and BS4) divide the pulse energy equally along the MZs fixed and moving arms. An AOM (Isomet, M1142-SF80L) inserted in the optical path of each arm, modulating at a particular radio frequency Ω_i, imparts a time-varying phase shift to the consecutive pulses of the pulse train [69]. All four AOMs are driven by the same RF signal generator (Novatech, 409B), which uses a common internal clock for generating the modulation signals $\Omega_{1,2,3,4} = (80.110, 80.103, 80.000, 79.975)$ MHz. Although referenced to a common clock, small frequency drifts can result in phase errors observed when processing the data. Simultaneous recording of the waveforms used to drive the AOMs allows for the correction of such errors. To track the time-dependence of the difference frequencies $\Omega_{12}(t)$ and $\Omega_{34}(t)$, the difference frequency output of two frequency mixers (M1 and

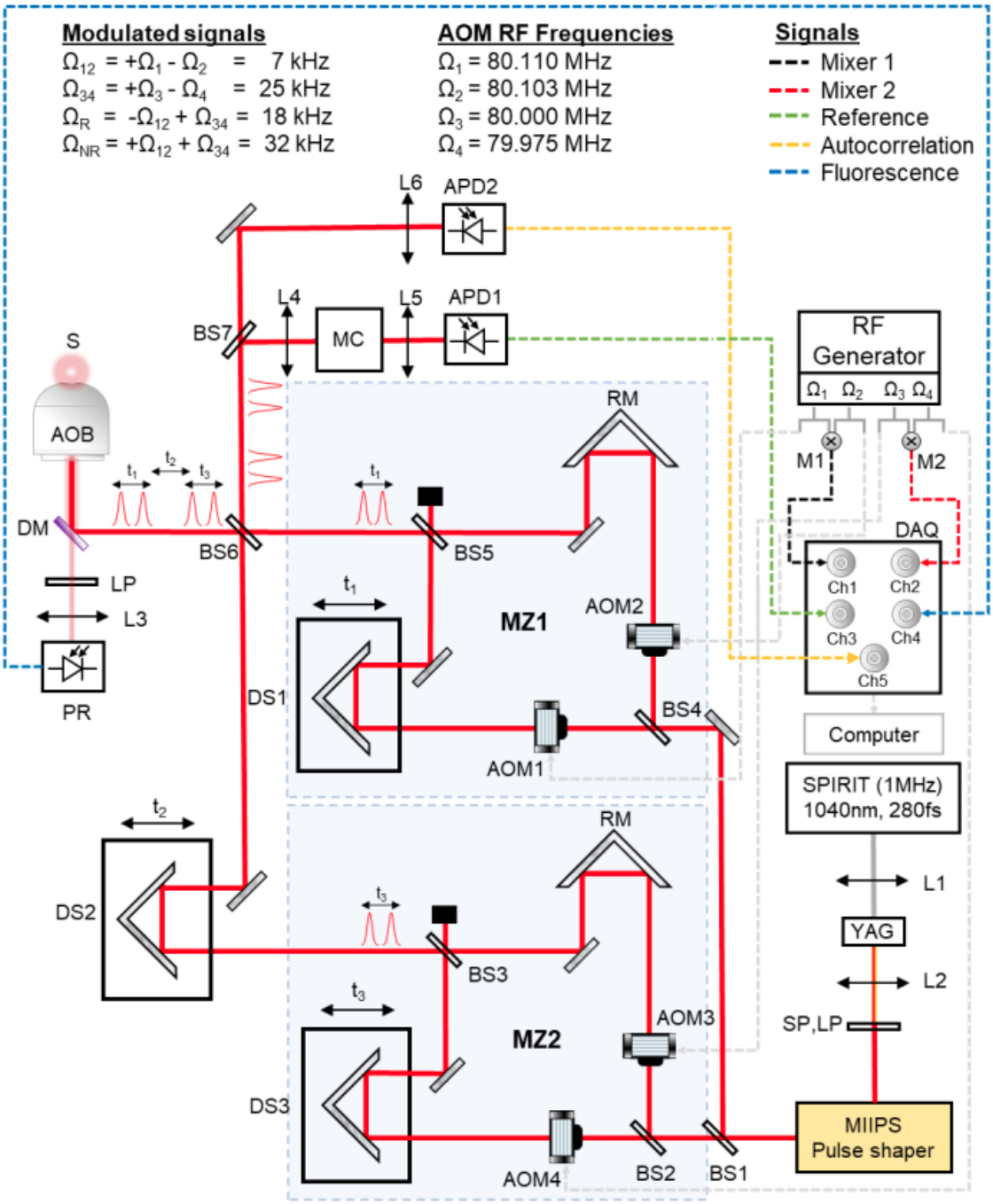

Figure 6.2: Experimental setup of the continuous-scanning phase-modulated fluorescence-detected 2D spectrometer: beam splitter (BS), acousto-optic modulator (AOM), Mach–Zehnder (MZ) interferometer, radio frequency mixer (M), delay stage (DS), retroreflector mirror (RM), monochromator (MC), avalanche photodiode (APD), variable gain photoreceiver (PR), short pass optical filter (SP), long pass optical filter (LP), dichroic mirror (DM), sample (S), air objective (AOB), and data acquisition card (DAQ).

M2, Mini-Circuits, ZAD-1-1+) yields $M_{12}(t)$ and $M_{34}(t)$.

Each pair of the modulated pulses is recombined on a beam splitter (BS3 and BS5) at the interferometer outputs, with the interpulse delay within each interferometer (t_1 and t_3), varied using a mechanical delay stage (DS, Newport, M-VP25XL). While the time delays t_1 and t_1 correspond to the coherence and detection times, respectively, the waiting time t_2 is controlled by an additional delay stage (DS2, Newport, ILS150). All three mechanical stages are controlled using a motion controller (Newport, XPS-Q4).

Finally, both pulse pairs are recombined to form a collinear four-pulse train at BS6 with half of the energy used for interacting with the sample. The other output from BS6 is equally divided at BS7. The reflected beam is spectrally narrowed around 825 nm (4.2 nm FWHM bandwidth) by using a monochromator (MC, Dynacil, MC1-05G, 300 µm slit size) and detected using an avalanche photodiode (APD1, Thorlabs, APD120A) to provide the spectrally narrowed four-pulse reference signal $S_{4Pref}(t)$. A neutral density filter is placed before the MC to avoid detector saturation and nonlinear effects. The transmitted beam is used to record the four-pulse interference signal $S_{4PAC}(t)$, also detected using an avalanche photodiode (APD2, Thorlabs, APD130A2) after reducing the intensity using a neutral density filter.

The four-pulse sequence is directed to a stage-scanning inverted microscope (Olympus 1X51). An 875 nm dichroic mirror (DM, Shemrock) reflects the incoming beam toward an air objective NA 0.6 (AOB, Olympus, LUCPlanFLN 40x), which focuses the beam into a flowcell of 200 micron path length (Starna, 48-Q-0.2/UTWA-2).

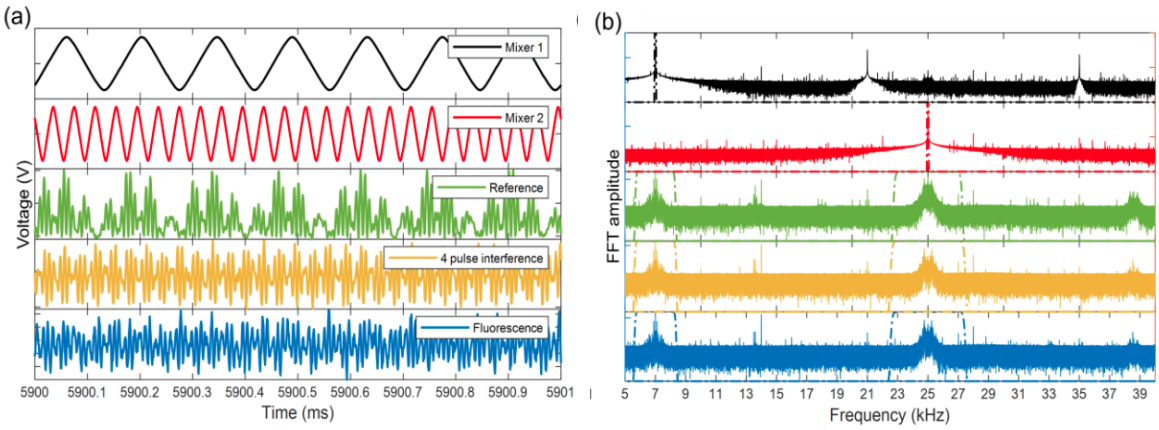

Figure 6.3: Signals acquired in the time domain for phase-modulated rapid-scanning FD-2DES experiment. These signals are frequency mixer signals $M_{12}(t)$ and $M_{34}(t)$ for MZ1 and MZ2 respectively, the four-pulse reference signal $S_{4Pref}(t)$ for tracking the time delays interferometrically, the four-pulse interference (autocorrelation) signal $S_{4PAC}(t)$ for measuring the pulse power spectrum, and the four-pulse fluorescence signal $S_{4PF}(t)$. The signals are shown over a small window of the total acquisition time and have been offset for clarity. (b) Fourier-transform of the time domain signals shown in (a), plotted on a logarithmic scale, indicating the different frequencies at which the signals appear. The window functions used to spectrally filter the signals of interest are also shown.

Prior to the experiments, the pulses are first compressed to 17 fs using MIIPS in a 20 m thick β-barium borate (BBO) crystal at the sample position. The emitted fluorescence is collected by the same objective. After being filtered by two long pass optical filters (AVR optics, TLP01-887 and Edmund optics, OD4-850 nm), it is focused on a low-noise photoreceiver PR (FEMTO Messtechnik GmbH, OE-200-SI) using a 5 cm focal length lens (L3). For a fixed waiting time t_2, the F-2DES data are acquired by continuously scanning t_3 back and forth at an average speed of 0.1 mm/s (and acceleration of 100 mm/s^2) between -80 and 80 fs while slowly scanning t_1 in a single direction from +80 to -80 fs at 0.0002 mm/s. The signals - $S_{4PF}(t)$, $M_{12}(t)$, $M_{34}(t)$, $S_{4Pref}(t)$, and $S_{4PAC}(t)$ - are digitized and recorded simultaneously using a 16-but data acquisition card (DAQ, National Instruments, NI-USB 6366) synchronized to the laser's repetition rate (1.0128334 MHz). All the figures reported in this chapter

correspond to the dataset acquired in 120 s, except Fig. 6.7 corresponding to the one acquired in 10 s.

6.5 Results

Fig. 6.3 (a) shows the time domain signals (zoomed over a 1 ms window of acquisition time) of $M_{12}(t)$, $M_{34}(t)$, $S_{4Pref}(t)$, $S_{4PAC}(t)$, and $S_{4PF}(t)$. $S_{4PF}(t)$ that are simultaneously digitized, enabling measurement of the linear excitation spectrum, rephasing and non-rephasing F-2DES signal. The Fourier transforms of these signals (taken from the full 2D dataset in which MZ1 and MZ2 are scanned as described above) are shown in Fig. 6.3 (b). The Fourier transform of the mixer signals $M_{12}(t)$ and $M_{34}(t)$ display the expected peaks at the AOM difference frequencies Ω_{12} and Ω_{34} for MZ1 and MZ2, respectively. The Fourier transform of the fluorescence signal shows the strongest peaks at Ω_{12} and Ω_{34}, arising from the linear excitation signal generated by the two-pulse sequence from MZ1 and MZ2, respectively. Similar peaks are also observed for the autocorrelation and the reference signal. We attribute the spectral broadening of these peaks to the fact that the time-dependence of the time delay significantly differs from a linear variation due to fluctuations of the path length in the interferometers. Due to the smaller amplitude of the nonlinear signals, the Fourier transform of the fluorescence signal does not show clear peaks at $\Omega_R = -\Omega_{12} + \Omega_{34}$ and $\Omega_{NR} = \Omega_{12} + \Omega_{34}$ for the respective rephasing and non-rephasing signals prior to correction for these fluctuations. The retrieval of interferometric time delays and the phasing of the F-2DES signals are achieved as detailed in Fig. 6.4.

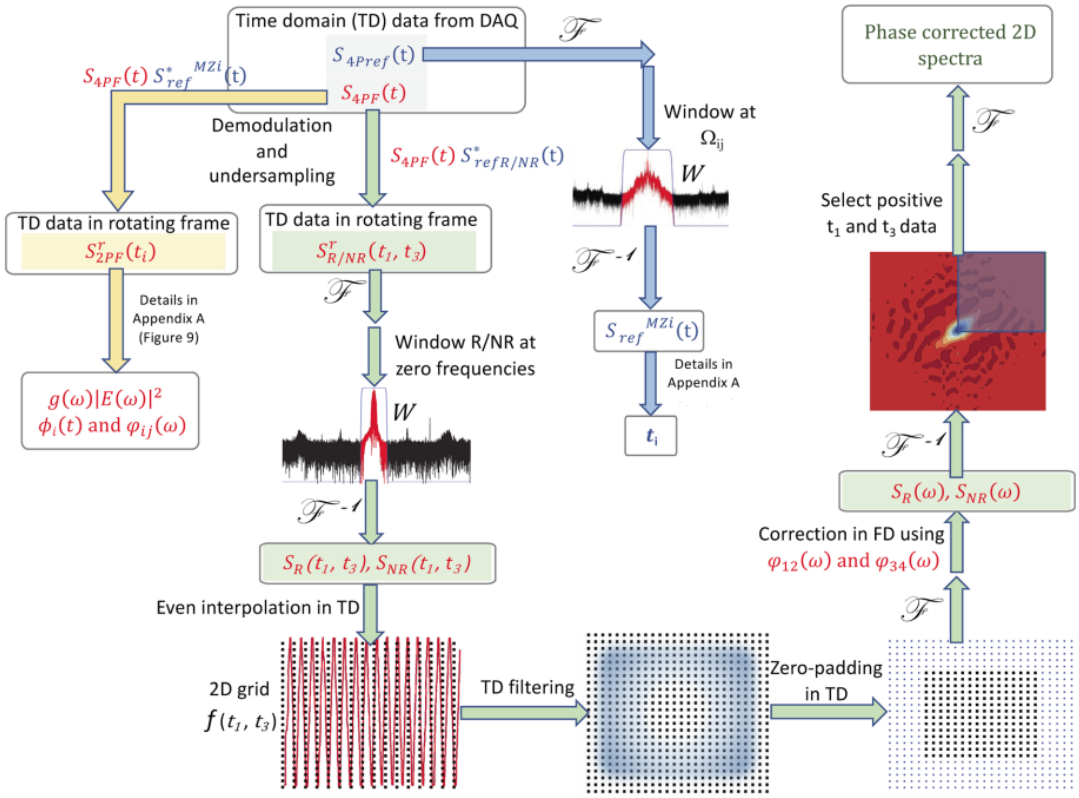

Figure 6.4: Flowchart depicting the processing of fluorescence data in order to obtain the phase-corrected rephasing and non-rephasing F-2DES spectra (green branch). The blue branch shows how the two MZ reference signals $S^{MZ1}_{ref}(t)$ and $S^{MZ2}_{ref}(t)$ and interferometric time delays t_i can be extracted from the four-pulse reference signal $S_{4Pref}(t)$ (more details have been outlined in Sec. **??**, Fig. 8...). These two MZ references are used for the demodulation and undersampling of the fluorescence signal $S_{4PF}(t)$ to get $S^{r}_{2PF}(t_i)$, as shown in the yellow branch. The four-pulse interference signal $S_{4PAC}(t)$ is demodulated and undersampled using the same treatment as done with $S_{4PF}(t)$ in the yellow branch and is not shown here. Note that the two MZ reference signals are also used in appropriate combinations to construct the rephasing $[S_{refR}(t) = S^{*MZ1}_{ref}(t)S^{MZ2}_{ref}(t)]$ and non-rephasing reference signals $[S_{refNR}(t) = S^{MZ1}_{ref}(t)S^{MZ2}_{ref}(t)]$. The reference signals $S_{refR/NR}(t)$ are then used to perform the demodulation of $S_{4PF}(t)$ to obtain $S^{r}_{R/NR}(t_1, t_3)$, shown in the green branch. Correction of the fluorescence signals for spectral phase imbalances in the MZs is made in the frequency domain using $\phi_{12}(\omega)$ and $\phi_{34}(\omega)$. Finally, the inverse Fourier transform allows for selection of the correct time ordered signals, from which the phased F-2DES signals are obtained upon Fourier transform.

6.5.1 Determination of interferometric time delays

To determine the interferometric time delays t_1 and t_3, the two-pulse reference signals $S_{ref}^{MZ1}(t)$, $S_{ref}^{MZ2}(t)$) are extracted via filtering of the four-pulse reference signal $S_{4Pref}(t)$ in the frequency domain at Ω_{12} and Ω_{34} for MZ1 and MZ2, respectively. Fig. 6.5 (a) shows the Fourier transform of the $S_{4Pref}(t)$ signal, along with the filters of width 2 kHz and 3 kHz used for extracting $S_{ref}^{MZ1}(t)$ and $S_{ref}^{MZ2}(t)$, respectively. The extracted reference signals, along with the mixer signals $M_{12}(t)$ and $M_{34}(t)$, then enable interferometric determination of t_1 and t_3. Upon filtering, inverse Fourier transformation enables determination of the time domain signal phase. Demodulation of the $S_{ref}^{MZ1}(t)$ and $S_{ref}^{MZ2}(t)$ reference signals from the respective MZ1 and MZ2 mixer phase yields the interferometrically determined t_1 and t_3 delays, as shown in Fig. 6.5 (b), where knowledge of ω_{ref} has been used. Further details of this procedure are given in Appendix (Sec. 6.9).

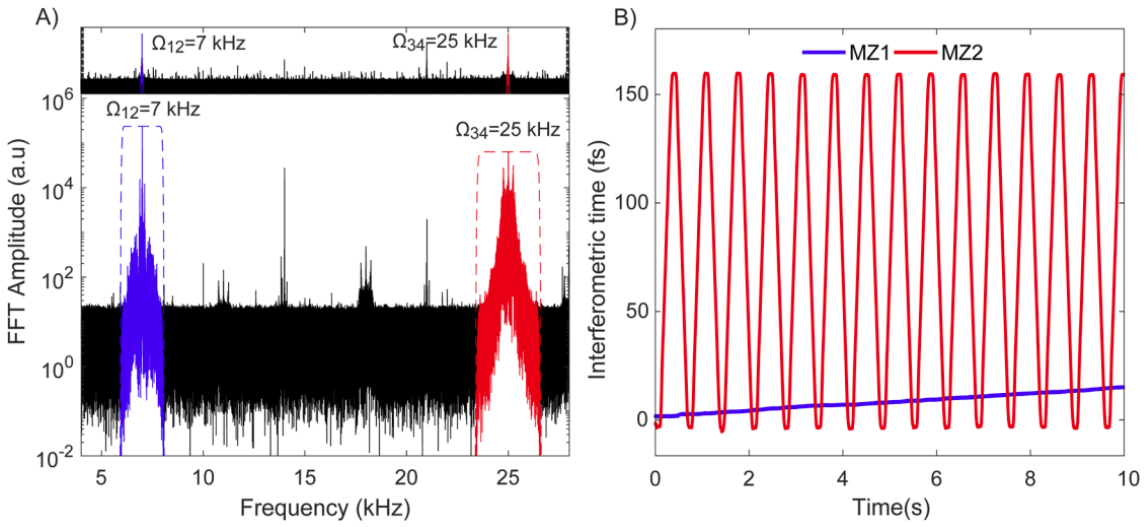

Figure 6.5: Interferometric determination of the time delays. (a) The Fourier transform of the mixer signals (top) and four-pulse reference signal (bottom), with amplitudes plotted on a logarithmic scale in both cases. Also shown are the filter functions used to extract the two-pulse reference signals $S_{ref}^{MZ1}(t)$, $S_{ref}^{MZ2}(t)$ for each MZ. (b) Interferometrically determined t_1 and t_3 delays, illustrating the unidirectional scanning of t_1 (MZ1) and the bidirectional scanning of t_3 (MZ2) (note that only an inset of the full scan is shown here)

6.5.2 Spectral phase correction, determination of zero delays, and linear excitation spectrum

To obtain spectral phase differences $\phi_{12}(\omega)$ and $\phi_{34}(\omega)$, the four-pulse fluorescence signal $S_{4PF}(t)$ is first demodulated and corrected for stage fluctuations using the two-pulse reference signals $S_{ref}^{MZ1}(t)$ and $S_{ref}^{MZ2}(t)$. In Fig. 6.6 (a), the signal in black corresponds to the Fourier transform of $S_{4PF}(t)$, centered around Ω_{34}. Below in red is shown the Fourier transform of the signal that is obtained after $S_{ref}^{MZ2}(t)$ is used to demodulate $S_{4PF}(t)$. The corrected data exhibit a distinct peak around zero frequency and are filtered about zero frequency using an appropriate bandwidth. For our analysis, we used a filter bandwidth of 1.25 Hz for MZ1 and 110 Hz for MZ2 fluorescence. The filtered signals are inverse Fourier transformed to yield the two-pulse linear fluorescence signals $S_{2PF}^{MZ1}(t)$ and $S_{2PF}^{MZ2}(t)$. In Fig. 6.6 (b), top plot shows the linear fluorescence signal $S_{2PF}^{MZ2}(t)$ for MZ2, plotted against the interferometrically determined time axis t_3. The figure shows 348 continuous repeated scans of MZ2 overlayed, demonstrating high reproducibility of the data.

Next, the two-pulse linear fluorescence signals $S_{2PF}^{MZ1}(t)$ and $S_{2PF}^{MZ2}(t)$ are interpolated to evenly spaced time points. In case of MZ2, the multiple scans are averaged to improve the signal-to-noise ratio. The evenly spaced data are filtered in the time domain prior to zeropadding to prevent the signal from falling abruptly to zero at the ends. After zeropadding, the signal is Fourier transformed to yield the spectral phase differences $\phi_{12}(\omega)$ and $\phi_{34}(\omega)$ for MZ1 and MZ2 respectively. This, in turn, leads to the determination of $t_1 = 0$ and $t_3 = 0$. The spectral phase differences arise due to slight path length differences and small dispersion imbalances from the AOMs between the arms of the interferometers, and are used to correct the spectra for phase-distortions. In addition to the spectral phase difference, we are also able to determine the product of the fluorescence linear excitation spectrum $g(\omega)$ and the pulse power

spectrum $|E(\omega)|^2$, given by $g(\omega)|E(\omega)|^2$. For MZ2, the zeropadded signal is shown in dashed red in Fig. 6.6 (b), bottom plot. Real part of the Fourier transform of the zeropadded signal is shown in gray in Fig. 6.6 (c), and corresponds to the linear fluorescence signal before phase correction. Fig. 6.6 (c) also shows the spectral phase $\phi_{34}(\omega)$ in solid black and the phase corrected signal (corresponding to $g(\omega)|E(\omega)|^2$) is shown in solid blue. Inverse Fourier transform of the phase corrected signal shows a symmetric scan MZ2 about $t_3 = 0$, as shown by the solid red curve in Fig. 6.6 (b), bottom.

The four-pulse interference signal $S_{4PAC}(t)$ is processed in a similar manner to the four-pulse fluorescence signal $S_{4PF}(t)$ described above. That is, it is first demodulated using the two-pulse reference signals $S_{ref}^{MZ1}(t)$ and $S_{ref}^{MZ2}(t)$ and filtered about zero frequency to obtain the two-pulse interference signals $S_{2PAC}^{MZ1}(t)$ and $S_{2PAC}^{MZ2}(t)$. These two-pulse interference signals are then interpolated to an evenly spaced time axis, filtered in the time domain, and zeropadded.

Finally, the Fourier transform of the zeropadded signal yields the pulse power spectrum $|E(\omega)|^2$. This independent measurement of $|E(\omega)|^2$ is used to determine the fluorescence excitation spectrum $g(\omega)$ from the product determined above using $S_{4PF}(t)$. Fig. 6.6 (c) shows the pulse power spectrum $|E(\omega)|^2$ of MZ2 in dashed cyan and the corresponding fluorescence excitation spectrum of IR-140 dissolved in DMSO in red. The linear absorption spectrum of IR-140 in DMSO is also shown in dashed magenta. The gray shaded area in Fig. 6.6 (c) marks the region of substantial uncertainty in the determination of the linear fluorescence excitation spectrum $g(\omega)$, due to the relatively low amplitude of $|E(\omega)|^2$ and differences between the actual pulse spectrum interacting with the sample and our measured $|E(\omega)|^2$, obtained from $S_{4PAC}(t)$. Sources of the spectral differences include the dichroic mirror (DM),

transmission through the microscope objective (AOB). An improved measurement of $g(\omega)$ would require matching the optical elements to collect the true pulse spectrum at the sample position.

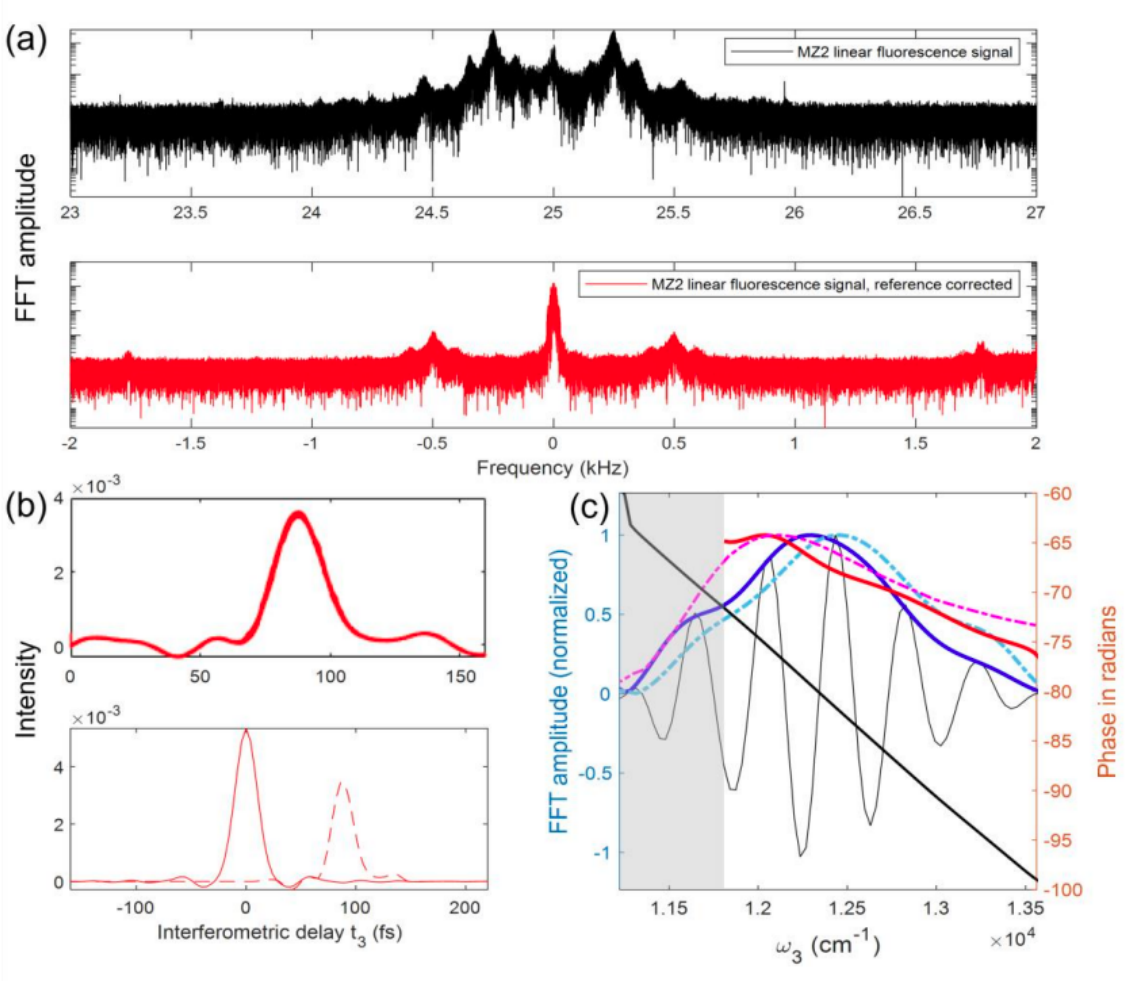

Figure 6.6: Top (black): Fourier transform of the fluorescence signal $S_{4PF}(t)$, zoomed around the peak at 25 kHz, corresponding to MZ2 difference frequency Ω_{34}. Doppler shift caused by bidirectional scanning leads to the appearance of distinct peaks. Bottom (red): Fourier transform of the fluorescence signal after demodulation using reference signal $S_{ref}^{MZ2}(t)$, showing correction for the MZ2 stage motion. (b) Top: Linear fluorescence signal for MZ2 showing the reproducibility of the multiple MZ2 scans. 348 such continuous scans are shown. These time domain data are obtained after inverse Fourier transforming the frequency domain signal shown in (a) after it is filtered about zero frequency. The x-axis shown is the interferometric time delay t_3 obtained from $S_{ref}^{MZ2}(t)$ as described in Sec. 6.5.1. Bottom: Linear fluorescence signal for MZ2 before (dashed) and after (solid) correction of the spectral phase, yielding a symmetric MZ2 scan about $t_3 = 0$. (c) Real part (blue) of $g(\omega)|E(\omega)|^2)$ of IR-140 in DMSO measured using MZ2 and the real part of $g(\omega)|E(\omega)|^2)$ prior to correction

(gray) of the spectral phase (solid black) are shown. In addition, the linear fluorescence excitation spectrum (red) of IR-140 in DMSO, and the pulse power spectrum for MZ2 (dashed teal) obtained using the four-pulse interference signal $S_{4PAC}(t)$ are shown. The linear absorption spectrum of IR-140 in DMSO (dashed magenta) is also shown. The shaded gray area marks the region of uncertainty in the determination of the linear fluorescence excitation spectrum. This uncertainty arises from different optical elements (shown in Fig. 6.2), most importantly the microscope objective and dichroic mirror, that produce differences in the spectral amplitude of the light that excites the sample compared to what is measured from the four-pulse interference signal $S_{4PAC}(t)$.

6.5.3 Processing and phasing of fluorescence-detected 2D spectra

Fig. 6.4 shows a flowchart depicting the steps in processing and phasing the F-2DES spectra. The rephasing and non-rephasing are processed separately and added to obtain the absorptive F-2DES spectra. To demodulate the rephasing and non-rephasing signals present in $S_{4PF}(t)$, we construct the corresponding reference signals $S_{refR/NR}(t)$ using the two-pulse reference signals $S_{ref}^{MZ1}(t)$ and $S_{ref}^{MZ2}(t)$, such that the rephasing reference signal $S_{refR}(t) = S_{ref}^{*MZ1}(t)S_{ref}^{MZ2}(t)$ and the non-rephasing reference signal $S_{refNR}(t) = S_{ref}^{MZ1}(t)S_{ref}^{MZ2}$. The demodulated and stage corrected rephasing and non-rephasing signals are then filtered in the frequency domain around zero frequency using filters of width 70 Hz and 46 Hz respectively. The filtered signals are inverse Fourier transformed to yield the rephasing signal $S_R(t_1, t_3)$ and the non-rephasing signal $S_{NR}(t_1, t_3)$, which are then interpolated to an evenly spaced grid of time points. We use a 2D time domain filter on the evenly spaced data prior to zeropadding and Fourier transform the data with respect to t_1 and t_3 to obtain the rephasing and non-rephasing F-2DES spectra.

The rephasing and non-rephasing spectra are then phase-corrected upon subtracting $\phi_{12}(\omega) + \phi_{34}(\omega)$ determined from the linear fluorescence signals. Inverse Fourier transformation then allows for the selection of the time domain quadrant corresponding to correct time ordering in the 2D measurement ($t_1 > 0$, $t_3 > 0$). Fourier transfor-

mation of the correct time quadrant yields phased 2D spectra. The rephasing spectra are flipped about the ω_1 axis before reporting. Addition of the flipped rephasing spectra with non-rephasing spectra yields the absorptive F-2DES spectra. Fig. 6.7 shows the phase-corrected rephasing, non-rephasing, and absorptive F-2DES spectra at $t_2 = 0$.

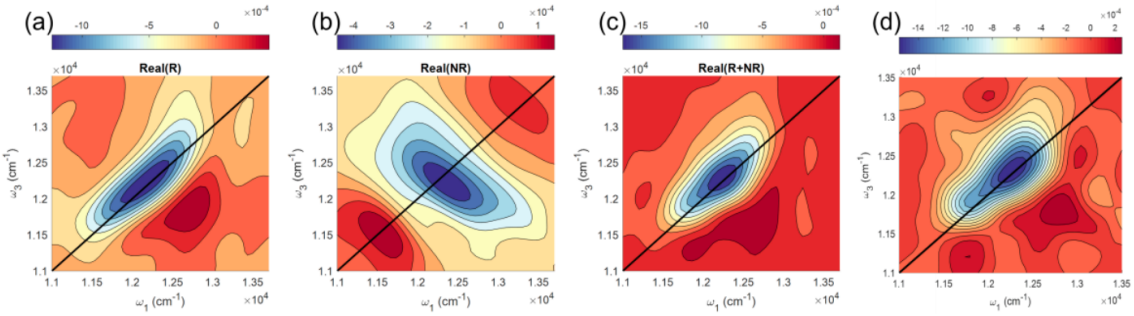

Figure 6.7: Fluorescence detected 2D spectra for IR-140 in DMSO at t_2=0. (a) Real Rephasing spectrum. (b) Real Non-rephasing spectrum. (c) Real absorptive spectrum (acquisition time of 120 s). (d) Real absorptive spectrum (acquisition time of 10 s))

6.6 Discussion

Continuous-scanning offers the advantage of speed in comparison to some step-scanning implementations of multidimensional spectroscopy, which may suffer from longer data acquisition times as delay stages "settle" to the target delay or phase-locked-loops establish locking. We estimate that our previous step-scan approach required ∼50% longer acquisition time due to stage travel and settling times, although this factor will vary for different motorized stages. Other continuous-scanning approaches to multidimensional spectroscopy have reported tenfold decreases in acquisition time, thereby making measurements less susceptible to laser fluctuations and enhancing signal-to-noise ratios [188]. Decreasing acquisition time is important for reducing photobleaching in F-2DES measurements, particularly on small ensembles approaching the single molecule level.

The digital lock-in approach has the advantage of enabling the simultaneous acquisition of multiple multidimensional spectroscopic measurements. Here, we have demonstrated the acquisition of linear fluorescence excitation spectra as well as fluorescence detected 2D rephasing and non-rephasing signals. The simultaneous acquisition of the two-quantum 2D spectra could be readily added to our approach. This would require the use of a fluorescence detector with higher bandwidth to enable distortion-free detection of the signal (at $\Omega_1 + \Omega_2 - \Omega_3 - \Omega_4 = 238$ kHz in our current implementation). For recording signals that rapidly oscillate during t_2, such as two-quantum 2D signals, the interferometric tracking of t_2 could be easily implemented in the same manner as for t_1 and t_3 with the addition of a third frequency mixer to detect Ω_{23}. We note that in typical implementations of 2DES, rephasing and nonrephasing spectra are recorded in separate scans, which can lead to difficulties in "phasing" the data [96]. In phase-modulated 2D measurements based on conventional lock-in detection, the phase is typically adjusted such that the real parts of the signal are maximized during the overlap of the pulses ($t_1 = t_3 = 0$) [74][70]. As discussed by Kalaee and co-workers, absolute signal phase determination, as we perform here, may enable the separation of true nonlinear signals from those produced by incoherent mixing of linear signals that can occur in action-based 2D spectroscopy [143].

We note that our approach is somewhat analogous to the recent demonstration of Mueller et al. in which they used a 125 fold phase-cycling scheme for the collection of multiple multidimensional signals using a 1 kHz laser source [189]. Their method employs step-scanning, and the pulse shaper used to implement the experiment has different bandwidth and repetition rate considerations than our approach. They report an acquisition time of 8 min for the acquisition of a 3D scan, requiring ∼28 s for a single 2D spectrum, with 125 phase cycles at 225 distinct (t_1, t_3) points at a

given t_2 time. Our approach is currently limited by the speed of our linear stages but benefits from the higher repetition rate of our laser source (1 MHz) and the increased speed offered by dynamic phase-cycling using AOMs. After appropriate optimization in stage speed and AOM frequencies, a gain in acquisition speed of more than three orders of magnitude can be expected. However, a fair comparison of various methods would examine the time required to collect the same set of multidimensional signals with equivalent signal-to-noise ratios on identical samples. We note that the AOMs used in our approach impart spatial chirp that may be important to compensate, depending on the application. Compensation could be achieved via prisms, the use of spatial filtering, or double-passing of the AOMs [190, 191]. The phase-modulation approach has been used with laser sources varying in the repetition rate from ∼80 MHz to 250 kHz. In order to effectively suppress $1/f$ noise, modulation rates should be selected to move the detection window to higher frequencies, within the digital sampling capabilities of the setup. We note that continuous-scanning with interferometric determination of the time delays could also be achieved via conventional lock-in detection rather than the fully digital lock-in approach we adopt here. To enable interferometric tracking of the delays, appropriate combinations of the MZ1 and MZ2 mixer signals would need to be constructed for use as references to isolate the signals of interest. In such an implementation, the number of signals that could be simultaneously detected would likely be limited by the number of channels on the lock-in amplifier.

While here we have collected fluorescence-detected linear and 2D spectra, an analogous digital lock-in phase-modulated approach could be readily developed for coherent 2D measurements, in which a fourth pulse would bypass the sample and be used for time domain heterodyne detection of the coherent 2D signal in a similar manner to the recent demonstration by Autry et al [183].

6.7 Conclusion and Perspectives

In conclusion, we have presented a continuous-scanning approach to F-2DES that combines acousto-optic phase-modulation with digital lock-in detection. We have demonstrated the method by measuring the linear excitation spectrum and absorptive fluorescence-detected two-dimensional electronic spectra of a laser dye. Advantages of phase-modulation include the suppression of $1/f$ laser noise due to the shifting of the signal detection window to frequencies above $\sim$1 kHz where laser noise dominates. Digital lock-in detection offers a straightforward path to the simultaneous measurement of linear and nonlinear spectroscopic signals without the need for a multiple-channel lock-in amplifier. Our experimental setup enables straightforward interferometric tracking of the time delay to allow for the robust real-time determination of the absolute signal phase. We expect our approach to be particularly useful for reducing the acquisition time of spatially resolved fluorescence-detected multidimensional spectroscopy measurements of samples that exhibit photobleaching [70].

6.8 Acknowledgements

J.P.O., D.A., and A.J. acknowledge support from the AFOSR Biophysics program under Grant Nos. FA9550-21-1-0098 and FA9550-19-1-0267. J.P.O. also acknowledges a visiting scientist grant from the Ecole Polytechnique. F.S. acknowledges support from the National Science Foundation through Grant No. PHY-1914608.

6.9 Appendix: Linear Fourier Transform Spectroscopy with Phase-Modulation and Continuous Scanning

We consider in this appendix a Fourier-transform spectroscopy measurement of a signal that is linear in the pulse intensity (two field interactions), such as a first-

order autocorrelation, or the two-pulse fluorescence signal in the current experiment. For generality, and to allow for the case of a dispersion-unbalanced Mach–Zehnder (MZ) interferometer, we assume that the total electric field delivered by using the MZ interferometer reads $E_1(t) + E_2(t-\tau)$, where $E_2(t)$ is a possibly dispersed replica of $E_1(t)$. The quantity t is the time, here at the femtosecond timescale, and τ is the time delay between pulses in the two distinct arms of the MZ. For a single laser shot, let us first consider the energy at the output of the MZ that would be measured using a perfect integrating photodetector. This quantity is given by

$$I_{MZ}(\tau) \propto \int_{-\infty}^{\infty} |E_1(t) + E_2(t-\tau)|^2 dt = const + S(\tau) + S(\tau)^*, \tag{6.1}$$

where

$$S(\tau) = \int_{-\infty}^{\infty} E_2^*(t-\tau) E_1(t) dt = \frac{1}{2\pi} \int_{0}^{\infty} E_2^*(\omega) E_1(\omega) e^{-\imath\omega t} d\omega \tag{6.2}$$

is the correlation function, equal to the Fourier transform of $E_2^*(\omega)E_1(\omega)$ according to the convolution theorem. This expression can be generalized to any time-invariant signal linear in the pulse energy, i.e., bilinear in the electric field, provided that the non-instantaneity of the response is appropriately taken into account. The previous expression must then be replaced with

$$S(\tau) = \frac{1}{2\pi} \int_{0}^{\infty} g(\omega) E_2^*(\omega) E_1(\omega) e^{-\imath\omega t} d\omega, \tag{6.3}$$

where $g(\omega)$ is the frequency domain function that describes the response of the system to the two electric-field interactions, one from each arm of the MZ. This function is known to be a real quantity, as a consequence of $S(-\tau) = S(\tau)$ in the case of a balanced interferometer (i.e., when $E_1 = E_2$). We retrieve the case discussed above of a first-order autocorrelation S_{2PAC} pulse measurement (with an ideal broadband

detector by assuming $g(\omega)$ = constant, whereas $g(\omega)$ should be replaced with the actual detector spectral response function for a non-ideal photodetector. In the case of the linear fluorescence signal $S_{2PF}(\tau)$, the response function $g(\omega)$ represents the fluorescence excitation spectrum.

Let us now consider a periodic train of laser shots centered at times t_n. Considering the fact that AOMs in arms 1 and 2 of the MZ modulate the pulse phases at frequencies Ω_1 and Ω_1, respectively, and that the diffracted ultrashort pulse samples the AOM phase at time t_n, we obtain

$$\begin{aligned} S_{2PF}(\tau, t_n) &\propto \frac{1}{2\pi} \int_{-\infty}^{\infty} g(\omega) E_2^*(\omega) e^{\iota\Omega_2 t_n} E_1(\omega) e^{-\iota\Omega_1 t_n} e^{-\iota\omega\tau} d\omega \\ &= \frac{1}{2\pi} \int_{-\infty}^{\infty} g(\omega) E_2^*(\omega) E_1(\omega) e^{-\iota\Omega_{12} t_n} e^{-\iota\omega\tau} d\omega \end{aligned} \tag{6.4}$$

where $\Omega_{12} = \Omega_1 - \Omega_2$. Assuming a constant stage-scanning speed of v, the time delay is sampled at the laser shot time according to the relation $\tau(t_n) = 2vt_n/c$. Finally, the measured signal reads

$$S_{2PF}(\tau, t_n) \propto \frac{1}{2\pi} \int_{-\infty}^{\infty} g(\omega) E_2^*(\omega) E_1(\omega) e^{-\iota(\Omega_{12} + 2v\omega/c)t} d\omega \tag{6.5}$$

where t now represents the measurement time, here at the sub-microsecond time scale. It is important to stress that the above expression is valid only when the scanning speed is small enough so that the frequency extent associated with the modulated signal is much smaller than the electronic detection bandwidth. Furthermore, the above expression is an idealization, assuming that the AOM frequencies and stage speed are perfectly constant. In practice, we may wish to take into account any small drift $\delta\Omega_{12}(t)$ of the AOM frequency difference (found to be several Hz in

our experiment). Even more importantly, due to mechanical imperfection, the stage speed is not exactly constant. The actual signal thus reads

$$S_{2PF}(\tau, t_n) \propto \frac{1}{2\pi} \int_{-\infty}^{\infty} g(\omega) E_2^*(\omega) E_1(\omega) e^{-\iota(\Omega_{12}+\phi(t)+\omega\tau(t))} d\omega, \tag{6.6}$$

where

$$\phi(t) = \int_0^t \delta\Omega_{12}(t')dt' \tag{6.7}$$

is the accumulated AOM phase drift, and

$$\tau(t) = \int_0^t \frac{2v(t')}{c} dt' \tag{6.8}$$

is the actual time delaym which can also include any contribution from vibrationsin the interferometer In order to measure these quantities with the required accuracy, we simultaneously record the mixer signal

$$M_{12}(t) \propto e^{-\iota(\Omega_{12}t+\phi(t))} \tag{6.9}$$

and a reference signal monitoring the interference of pulses 1 and 2 in a monochromator centered at frequency ω_{ref}. The measured signal, again linear in the pulse energy, is consequently given by

$$\begin{aligned} S_{2PF}(\tau, t_n) &\propto \frac{1}{2\pi} \int_{-\infty}^{\infty} f(\omega) E_2^*(\omega) E_1(\omega) e^{-\iota(\Omega_{12}+\phi(t)+\omega\tau(t))} d\omega \\ &\propto e^{-\iota(\Omega_{12}t+\phi(t)+\omega_{ref}\tau(t))} \end{aligned} \tag{6.10}$$

where $f(\omega)$ is the monochromator spectral response, assumed to be a narrow peak centered on frequency ω_{ref}. Selecting Ω_{12} via windowing in the frequency domain, we

take into account any phase drift by directly subtracting point-by-point in the time domain,

$$S_{ref}M_{12}^{*}(t) \propto e^{-\imath\omega_{ref}\tau(t)}, \tag{6.11}$$

which yields the actual time delay $\tau(t)$ after phase unwrapping, allowing us to

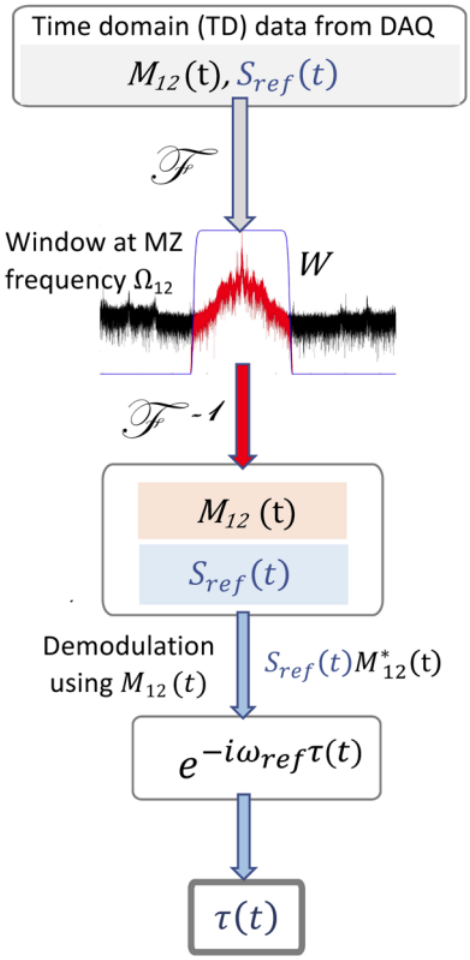

Figure 6.8: Flowchart depicting the processing of the time domain data to obtain the interferometric time delay $\tau(t)$.

average each measured data point in the appropriate time bin and thus record $S_{2PF}(\tau)$. The procedure for determining time delay $\tau(t)$ is depicted in Fig. 6.8.

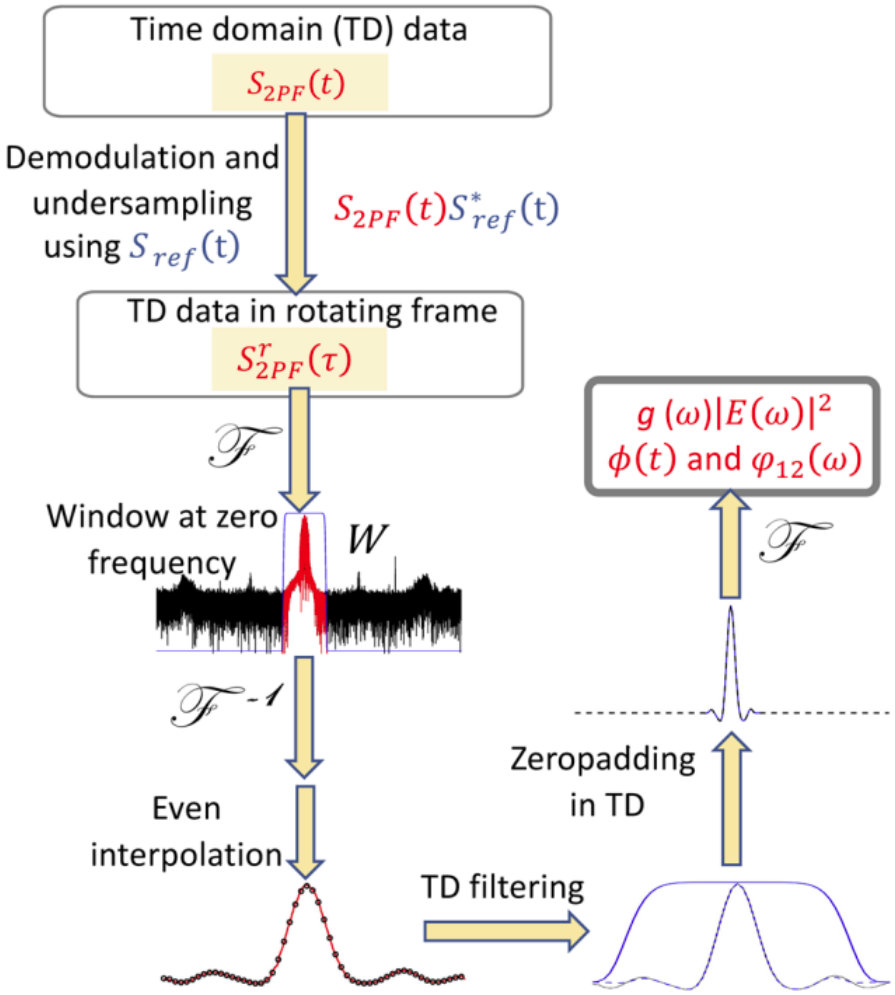

Figure 6.9: Flowchart depicting the processing of the linear two-pulse interference time domain data to obtain $g(\omega)|E(\omega)|^2$, the unknown spectral phase $\phi_{12}(\omega)$, $\phi(t)$, and the location of $\tau = 0$. The two-pulse interference data can be fluorescence $S_{2PF}(t)$ (notation used in the flowchart is for fluorescence data) or autocorrelation $S_{2PAC}(t)$, differing only in the value of $g(\omega)$ which represents the fluorescence excitation spectrum for $S_{2PF}(t)$ and is constant for $S_{2PAC}(t)$ assuming ideal detector response. Therefore, result of the above analysis when starting with $S_{2PAC}(t)$ yields the pulse power spectrum $|E(\omega)|^2$.

Furthermore, the signal of interest can be corrected with respect to AOM frequency drift and shifted to the rotating frame,

$$S^r_{2PF}(\tau) = S_{2PF}(t)S^*_{ref}(t) \propto \frac{1}{2\pi}\int_{-\infty}^{\infty} g(\omega)E^*_2(\omega)E_1(\omega)e^{-\iota(\omega-\omega_{ref})\tau}d\omega \tag{6.12}$$

We further assume identical spectra for the two pulses ($|E_1(\omega)| = |E_2(\omega)| = |E_2(\omega)|$) but allow for a possible spectral phase difference $\phi_{12}(\omega) = \phi_1(\omega) - \phi_2(\omega)$ induced by different dispersion between arms 1 and 2 due to AOM differences or slight misalignment,

$$S^r_{2PF}(\tau) \propto \frac{1}{2\pi} \int_{-\infty}^{\infty} g(\omega)|E(\omega)|^2 e^{\iota(\phi_{12}(\omega)-(\omega-\omega_{ref})\tau)} d\omega \tag{6.13}$$

Since $g(\omega)$ is purely real, the FT of $S^r_{2PF}(\tau)$ yields $g(\omega)|E(\omega)|^2$,the unknown spectral phase $\phi_{12}(\omega)$, and the location of $\tau = 0$. As a time shift is associated with a linear slope, the spectral phase is defined such that its first-order derivative at center frequency is zero so that the zero time delay can be defined unambiguously. The data processing steps are depicted in Fig. 6.9. Furthermore, an independent measurement of the power spectrum $|E(\omega)|^2$ by interferometric autocorrelation $S_{2PAC}(t)$ enables the determination of $g(\omega)$, the fluorescence excitation spectrum, shown by the red curve in Fig. 6.6 (c). In summary, the simultaneous measurements of $S_{2PF}(t)$, $S_{2PAC}(t)$, $S_{ref}(t)$, and $M_{12}(t)$ yield the interferometric time axis τ, including $\tau = 0$, $\phi(t)$, $\phi_{12}(\omega)$, and $g(\omega)$.

Author contributions

DA and AJ worked on the measurements and experimental setup, and data processing. FS assisted with the experiments. XS worked on the aspects that required a detailed knowledge of electronics. All the authors contributed to the writing of the manuscript.

CHAPTER VII

Future Directions

There are several future technical advances to F-2DES that could expand its applications, improve the signal-to-noise ratio of the measurements and increase the information available from the method. First of all, a number of materials containing a range of absorbers could benefit from a broadband implementation of F-2DES to decongest correlations between the different entities. Moreover, a broadband version of F-2DES will be useful for microscopy. From the work in this thesis, we have compared F-2DES against the conventional C-2DES method and find that in its current implementation, F-2DES is a rather poor choice to study energy transfer dynamics in large systems. Improved signal-to noise ratio by fast scanning along t_2, combined with higher averaging will enable the kinetics to be evident from F-2DES measurements. However, we note that the suppression of kinetics in F-2DES is both system and implementation dependent, and improved signal-to-noise can only help resolve the small rise in signals with more ease. In order to gain useful information about the system dynamics, for example, in the absence of annihilation, time-gating of the fluorescence during the detection time has been suggested [6, 73]. Implementations to separate the SE/GSB signals will also help to isolate the energy transfer pathways that carry information relevant to energy transfer. We discuss each of the aforementioned suggestions in this Chapter. For broadband F-2DES, we present preliminary lower-dimensional

results using a broadband phase-modulated Fourier-transform spectrometer.

7.1 Broadband phase-modulated Fourier-transform spectroscopy (PM-FTS)

We have discussed the implementation and applications of phase-modulated 2DES in this thesis. PM-FTS relies on AO modulators for modulating the pulse-to-pulse carrier-envelope phase. However, AOMs have a limited bandwidth of around 130 nm-150 nm and therefore, limit the spectroscopic bandwidth that can be studied with phase-modulation techniques. This is especially important in multidimensional spectroscopy where a broader bandwidth enables the study of diverse processes such as coherences and energy transfer between spectrally separated states [192–195]. While broadband multidimensional spectroscopy has been achieved so far [96, 107, 196], a broadband phase-modulation approach is missing.

Here, we present our preliminary work towards expanding the bandwidth of PM-FTS. Our approach circumvents the bandwidth limitations of AOMs by modulating the narrowband laser output before performing continuum generation to produce broadband pulses. As proof of principle, we report absorption and fluorescence linear excitation spectra of BChl *a*, which is the primary light-absorbing pigment in many photosynthetic bacteria. Our experiments pave the way for future broadband multidimensional spectroscopy experiments based on phase-modulation.

7.1.1 Experimental setup

A layout of the experimental setup used in our measurements is shown in Fig. 7.1. For the preliminary experiments, we employ a single MZ interferometer and perform signal acquisition and data processing using the procedure detailed in the Appendix

(Section 6.9), Chapter VI. The output from a 1040 nm, 1 MHz ytterbium amplified laser (Spectra Physics Spirit-HE, 7.5 W, 280 fs pulse duration) is split using a 3 mm 50/50 beamsplitter (Evaporated Coating Inc. 1040-1600 nm) into a Mach-Zehnder (MZ) interferometer. The reflected beam passes through a 3 mm N-BK7 window to compensate for the difference in dispersion compared to the reflected arm. The 1040 nm fundamental travels first through an AOM (Isomet M1346-aQ(fc) -H) in each arm. The modulation frequencies sent to the AOMs are generated by two outputs from an RF signal generator (Novatech, 409B, 1 kHz resolution) and amplified to about 50W (Mini-Circuits ZHL-100W-52-s+) for each AOM.

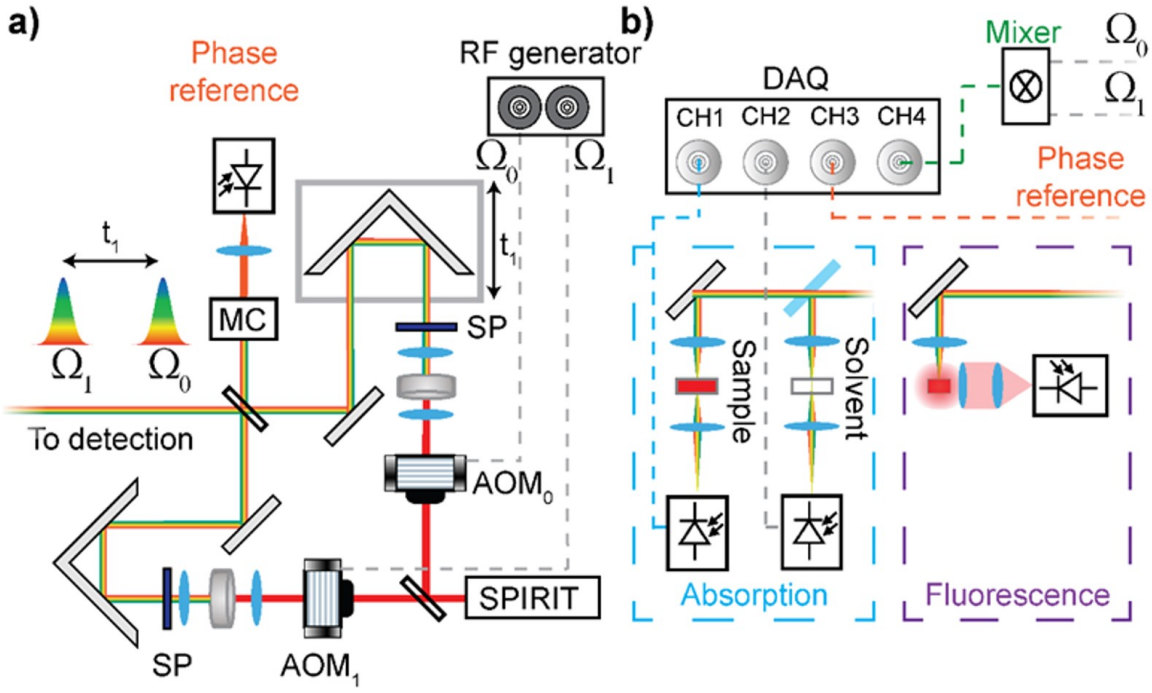

Figure 7.1: Experimental setup of the ultrabroadband continuous-scanning phase-modulated Fourier-transform spectrometer: beam splitter (BS), acousto-optic modulator (AOM), Mach–Zehnder (MZ) interferometer, delay stage (DS), retroreflector (R), monochromator (MC), short-pass optical filter (SP), and a 16-bit data acquisition card (DAQ).

The amplifiers are operated in the linear regime. For our measurements, we used AO frequency values Ω_0 =80 MHz and Ω_1 =79.997 MHz. We adjust the amplitude of

each RF signal sent to the AOMs such that the resulting first orders of each arm have the same average power of about 1W. The undiffracted zeroth order beam from the AOM (∼3W) is safely dumped into a beam block (Thorlabs LB2) using a D-shaped mirror. Each output from the RF generator is split into half and sent to a radio frequency mixer (Mini-Circuits, ZAD-1-1+). The output from the mixer is digitized by a 16-bit data acquisition card (DAQ, National Instruments, NI-USB 6366).

After each AOM, we place an iris to control the beam size that is used for continuum generation. The beams are then focused into an 8 mm thick YAG crystal using a 5 cm focal length achromatic lens (Thorlabs AC254-050-AB). The beam size, power, and focusing are matched between the two arms. We produce a continuum with a bandwidth of 500 nm to 1000 nm [159]. The beam is then collimated by an identical 5 cm focal length achromatic lens The fundamental beam is filtered out using a 950 nm short pass filter (Thorlabs FESH0950). Each arm is directed into a retro reflector. Arm 1 is fixed, while the retroreflector in Arm 0 is mounted on a mechanical delay stage (Newport, M-VP25XL). The two arms are then recombined with a 1 mm thick beam splitter, coated for 450-1000 nm (Layertec 106896). A 1 mm NKB7 compensating window is placed in Arm 1 before the recombination to compensate for additional dispersion added to Arm 0 due to the thickness of the recombining beam splitter.

One output of the MZ interferometer is spectrally narrowed at 630 nm using a monochromator (Optometric DMC1-03) and is focused onto a photodiode (Thorlabs PDA36A2) with a 5 cm focal length lens. The signal from the photodiode is recorded with the DAQ. The spectrally narrowed two-pulse interference signal enables the inteferometric tracking of the time delay [177]. In all the measurements, continuous rapid-scanning is performed by moving the mechanical stage back and forth at a speed of 0.1 mm/s about time zero. The delays are scanned between -800 fs to 800 fs. The

other output of the MZ interferometer is used to excite the sample. A small fraction of this beam is picked off with the help of a 3 mm thick uncoated window before the sample. Both the main beam to the sample and the weak pick off are collected by two identical photodiodes (Thorlabs PDA36A2) and the DAQ is used to record the photodiode signals. Fig. 7.2 (a) shows the time-domain inteferogram retrieved from the back and forth scans (in red) along with the averaged data. In Fig. 7.2 (b) we show the laser spectrum retrieved by recording the two-pulse interference signal from just the sample arm, along with the phase reference signal and the mixer signal. The linear signal analysis procedure shown in Fig. 6.9 is used. For all the measurements reported in this section, time delays are retrieved using the phase reference and mixer signals following the procedure outlined in Fig. 6.8. All the data shown in this section are measured within 2 min, but we have been able to achieve acquisition times as low as 8 s with respectable signal-to-noise ratios.

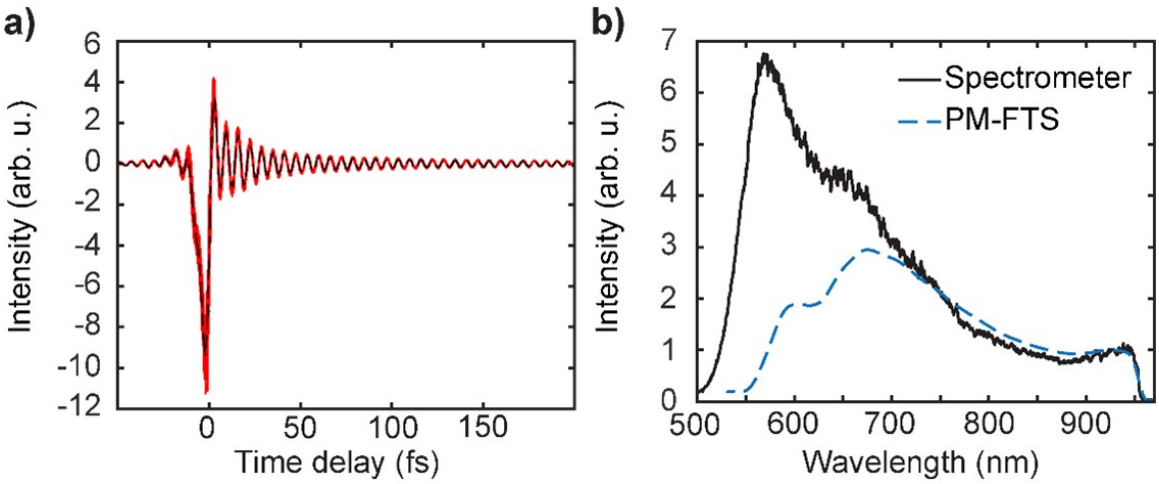

Figure 7.2: (a) Time-domain interferograms retrieved by recording the two-pulse interference output of the MZ. Data corresponding to 48 back and forth stage scans is shown (solid red line). Average of the 48 scans (dashed black line) used for calculating the pulse power spectrum is also shown. (b) (dashed blue line) The phase-corrected pulse power spectrum retrieved using the broadband PM-FTS setup, plotted against the spectrum measured using a commercial spectrometer (Ocean Optics, USB-2000) after recombination from the MZ (solid black line).

For linear absorption measurements we use two measurement positions (as shown

in Fig. 7.1): one contains just the solvent and uses the pick-off from the glass window (shown in blue), while the other contains the sample of interest. We will refer to the former as "solvent arm (S)" and the latter as "sample arm (S')". In order to measure the linear absorption, we perform two consecutive measurements. First, we measure the solvent in the sample arm and in the solvent arm. We then take a successive measurement where the solvent in the "sample arm" is replaced with the sample of interest. For a perfectly stable setup the first measurement would basically not contribute to the calculation of the absorption spectrum. However, if any drift of the continuum occurs we correct for it using the combination of measurements. Using the two measurements in the sample arm and solvent arm, we calculate the absorbance of the sample using

$$A = \log\left[I^{S}_{Sol}/I^{S}_{Samp}\right] - \log\left[I^{S'}_{Sol2}/I^{S'}_{Sol1}\right] \tag{7.1}$$

where I denotes the intensity retrieved from the measurements. The superscripts S and S' represent the sample and the solvent arms respectively and the subscripts $samp$ and $sol1,2$ stand for the measured material in each arm. $sol1$ and $sol2$ correspond to the two consecutive measurements taken. The intensity I in each of the four terms in Eq. 7.1 is obtained using the linear signal processing algorithm depicted in Fig. 6.9. Fig. 7.3 (a) compares the absorption spectrum (purple, dashed) retrieved from our PM-FTS measurements with one collected using a UV-Visible spectrometer (black), showing good agreement with our measurement. The laser spectrum used for collecting the spectra is shown in gray.

We also report fluorescence excitation measurements. A 90° detection geometry is used where the fluorescence is collected by a 2 inch diameter lens and is then focused onto an avalanche photodiode (Hamamatsu, c12703-01). Scattering light is

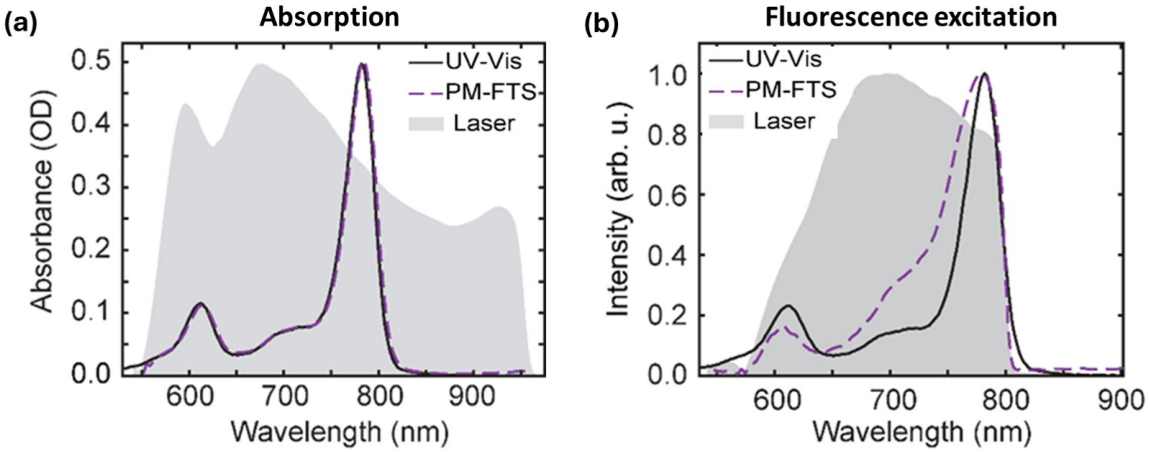

Figure 7.3: (a) Absorption spectrum of BChl *a* measured using broadband PM-FTS (dashed purple line). Eq. 7.1 is used to calculate the OD of the sample. For comparison, the absorption spectrum of BChl *a* measured using a UV-visible spectrometer is plotted (solid black line). Very good agreement is achieved between the two. (b) The fluorescence excitation spectrum (dashed purple) of BChl *a* retreived using broadband PM-FTS, plotted along with the absorption measured using UV-visible spectrometer (solid black line). The laser spectrum used for performing the measurements is shown in gray.

blocked by using appropriate long pass filters in front of the detector. The solvent arm without any sample or solvent is used as a reference arm to monitor the continuum throughout the experiment, recorded using a photodiode (Thorlabs PDA36A2). Fig. 7.3 (b) shows the product of the retrieved fluorescence linear excitation spectrum and the laser power spectrum (purple, dashed) from our PM-FTS measurements. The absorption spectrum (black) is shown for comparison. The laser power spectrum used in this measurement is shown in gray.

7.1.2 Discussion

We have demonstrated a broadband PM-FTS implementation and performed linear measurements as proof of principle. By performing the modulation prior to the continuum generation, the method allows full use of the continuum bandwidth, and also avoids the large spatial chirp that would accompany AO modulation after the continuum. This approach could be used for extreme bandwidth F-2DES as well as

C-2DES. This can be achieved by combining with broadband sources such as gas filled hollow-core fiber extending the available spectrum further to shorter wavelengths. An important future application of this setup will be broadband probing in F-2DES measurements, allowing correlation of spectrally separated peaks, such as Q_x and Q_y as well as Soret transitions of chlorophyll based excitonic systems. This approach is also very well suited for spatially-resolved F-2DES measurements since it combines fast acquisition times with low excitation intensities, and will be useful to study sensitive samples by reducing photobleaching effects.

7.2 Rapid-scanning fluorescence-detected three-dimensional electronic spectroscopy (F-3DES)

In Chapter VI, we have discussed a rapid-scanning implementation of F-2DES. We use a spectrally narrowed two-pulse interference signal combined with digital acquisition at a repetition rate of 1 MHz to continuously track the interferometric time delays t_1 and t_3 at a fixeed t_2. This method can be extended to scan all the three delays t_1. t_2, and t_3 at appropriate speeds and continuously track them all throughout the measurement. To achieve this experimentally, no additional optical element will be required. In order to track the third time delay, an additional mixer input to the DAQ is required. The RF generator outputs can be split three-ways instead of two-ways like in the current implementation VI such that the outputs oscillating at Ω_2 and Ω_3 are sent to a mixer to generate a third mixer signal. The reference signal from the monochromator already contains the two-pulse interference signal corresponding to $\Omega_{23} = \Omega_2 - \Omega_3$, and will need to be filtered out in the Fourier domain as an additional step. Similar steps will be needed for the fluorescence signal and AC signals.

While the procedure described above sounds rather simple, the bottleneck here

is the computational time. In the work shown in Chapter VI, the signal from each channel is acquired for a total of 2 min at a repetition rate of 1 MHz. This means that in 2D measurements, we deal with 5 channels with vectors of the size 1x120,000 points, making data processing per t_2 spectrum using MATLAB a time-consuming task ($\sim$15 min per t_2 point). Addition of another mixer channel will add to the computational time. Moreover, 3D interpolation of the data will be needed in the extension of the 2D rapid-scanning technique. Therefore, for future work, hardware based solutions such as an FPGA board will be required to overcome the limitations imposed by data processing in an otherwise really powerful technique.

7.3 Time-gated F-2DES and SE-GSB segregation

We discussed the effect of detection-time dynamics on the F-2DES spectral features. While in the measurements we have reported in this thesis, the measured fluorescence signal is integrated over the detection time, it has been suggested that time-gated fluorescence detection [73][71] can be used to separate annihilation contributions to the F-2DES spectra, retrieving information comparable to C-2DES. This will enable retrieving information equivalent to 2DES. Malý and Mancal [73] have shown using simulations by gating of the fluorescence signal at about half the annihilation time that their calculated F-2DES spectra resembled the C-2DES spectra. They also showed the variation of annihilation timescales on the cross peak behavior, indicating that detection time gating can also provide insights about the annihilation process itself. In addition to annihilation, other incoherent mixing contributions may also be suppressed using time-gating [150]. In an explicit description of detection time dynamics using a non-perturbative approach, Bruschi et al [144] recently investigated the interplay of exciton and biexciton states as a function of the detection time. It has also been highlighted by Kunsel et al that [71] the time-gated F-2DES spectra may contain contributions from coherences at early detection times. There-

fore, time-gating seems like the natural next step towards obtaining more meaningful information about multichromophoric systems like LH2 from F-2DES.

Another strategy may be able to investigate SE and GSB signals separately. Experimentally, this will involve a pump that overlaps with the lower energies of the absorption band and a probe that overlaps with the full band. The idea is that at early times, for the higher frequencies with overlap only with the pump, only GSB signals will be present, while both GSB and SE will be present at the pump frequencies [6]. Thus, time gating can also be used to exclusively select the SE pathways which originate from the lower lying excited states. Recently, Yang et al [175] proposed a 2D fluorescence excitation approach to selectively measure the SE contributions, capable of providing direct qualitative information about the system. Experimentally, this can be achieved by using two time delayed pulses for excitation followed by time- and frequency- resolved detection of the fluorescence spectra. A polarization-sensitive implementation of the 2D fluorescence excitation technique may also be useful for studying multichromophoric systems [175].

CHAPTER VIII

Conclusion and Outlook

2DES is a powerful technique for studying ultrafast dynamics in photosynthetic complexes. An collinear approach to 2DES based on fluorescence detection is attractive for microscopy purposes and allows for smaller ensemble studies. In Chapter II, we discussed the theory of incoherent mixing and exciton-exciton annhilation effects which distinguish the contributing signals in F-2DES spectra from C-2DES spectra. We reported the tests we conducted to check for the presence of incoherent mixing and detector nonlinearities in the F-2DES measurements in Chapter III. We also described our F-2DES setup which makes use of the phase-modulation and lock-in detection methodology first demonstrated by Tekavec et al [69].

In Chapter IV, we presented a comparison between F-2DES and C-2DES to study the energy transfer dynamics in LH2. We found that F-2DES (and more generally, action-detected 2DES) is not well-suited for this purpose. In Chapter V we studied a different photosynthetic system (dLH-RC), and found that F-2DES energy transfer dynamics were more pronounced compared to the LH2 case, despite the larger number of chromophores in the system. With insight from simulations, we found that the choice of the system, with different delocalization, changes the relative weighting of the SE to GSB pathways, manifesting directly in the energy transfer signatures observed. This makes observing energy transfer dynamics in large systems with weak

coupling or high disorder unfavorable. The sample dependence has also been pointed out in organic solar cells where incoherent mixing effects are non-negligible compared to perovskite solar cells, making the latter ill-suited for action-detected measurements [6]. In a recent report by Bolzonello et al [124] cross-peak dynamics attributed ultrafast hole transfer in a PM6/Y6 hetrojunction in an operating photovoltaic cell were observed using photocurrent detection.

Clearly, a careful choice of the system is necessary while using action-detected techniques. F-2DES has been shown to be an attractive alternative to C-2DES for small systems such as dyads and atomic systems. It may be particularly useful for studying charge separation in bacterial RCs with <10 pigments or isolated RCs such as the D1D2 cyt b559 PSII RC for which the C-2DES response is dominated by ESA pathways, because a clean GSB contribution may be revealed from the mutual cancellation of the two ESA pathways in F-2DES.

In Chapter VI, we demonstrated a rapid-scanning implementation of F-2DES, which will be an important way to achieve lower acquisition times for resolving dynamics in experiments prone to laser instabilities and mechanical vibrations in the setup. Finally in Chapter VII, we demonstrated a broadband implementation of the phase-modulated fluorescence measurement and proposed possible future strategies for the extension and improvement of F-2DES techniques. We conclude by saying that the future work based on time-gating and separation of SE pathways will determine the overall feasibility of F-2DES methods to shed useful information about excited-state dynamics in large systems.

Bibliography

[1] Jennifer L Herek, NJ Fraser, T Pullerits, P Martinsson, T Polivka, H Scheer, RJ Cogdell, and V Sundström. B800→ b850 energy transfer mechanism in bacterial lh2 complexes investigated by b800 pigment exchange. *Biophysical journal*, 78(5):2590–2596, 2000.

[2] Simon Scheuring and James N Sturgis. Chromatic adaptation of photosynthetic membranes. *Science*, 309(5733):484–487, 2005.

[3] Robert E Blankenship. *Molecular mechanisms of photosynthesis*. John Wiley & Sons, 2021.

[4] Yonghui Zeng, Vadim Selyanin, Martin Lukeš, Jason Dean, David Kaftan, Fuying Feng, and Michal Koblížek. Characterization of the microaerophilic, bacteriochlorophyll a-containing bacterium gemmatimonas phototrophica sp. nov., and emended descriptions of the genus gemmatimonas and gemmatimonas aurantiaca. *International journal of systematic and evolutionary microbiology*, 65(Pt_8):2410–2419, 2015.

[5] Pu Qian, Alastair T Gardiner, Ivana Šímová, Katerina Naydenova, Tristan I Croll, Philip J Jackson, Nupur, Miroslav Kloz, Petra Čubáková, Marek Kuzma, et al. 2.4-å structure of the double-ring gemmatimonas phototrophica photosystem. *Science Advances*, 8(7):eabk3139, 2022.

[6] Luca Bolzonello, Matteo Bruschi, Barbara Fresch, and Niek F van Hulst. Nonlinear optical spectroscopy of molecular assemblies: What is gained and lost in action detection? *The Journal of Physical Chemistry Letters*, 14(50):11438–11446, 2023.

[7] White paper principles of lock-in detection and the state of the art zurich instruments release. 2016.

[8] Miroslav Z Papiz, Steve M Prince, Tina Howard, Richard J Cogdell, and Neil W Isaacs. The structure and thermal motion of the b800–850 lh2 complex from rps. acidophila at 2.0 å resolution and 100 k: new structural features and functionally relevant motions. *Journal of molecular biology*, 326(5):1523–1538, 2003.

[9] Martin F Hohmann-Marriott and Robert E Blankenship. Evolution of photosynthesis. *Annual review of plant biology*, 62:515–548, 2011.

[10] Villy Sundström. Femtobiology. *Annu. Rev. Phys. Chem.*, 59:53–77, 2008.

[11] Gregory D Scholes, Graham R Fleming, Alexandra Olaya-Castro, and Rienk Van Grondelle. Lessons from nature about solar light harvesting. *Nature chemistry*, 3(10):763–774, 2011.

[12] Mark G Rockley, Maurice W Windsor, Richard J Cogdell, and William W Parson. Picosecond detection of an intermediate in the photochemical reaction of bacterial photosynthesis. *Proceedings of the National Academy of Sciences*, 72(6):2251–2255, 1975.

[13] Dewey Holten and Maurice W Windsor. Picosecond flash photolysis in biology and biophysics. *Annual Review of Biophysics and Bioengineering*, 7(1):189–227, 1978.

[14] S Hess, M Chachisvilis, K Timpmann, MR Jones, GJ Fowler, CN Hunter, and V Sundström. Temporally and spectrally resolved subpicosecond energy transfer within the peripheral antenna complex (lh2) and from lh2 to the core antenna complex in photosynthetic purple bacteria. *Proceedings of the National Academy of Sciences*, 92(26):12333–12337, 1995.

[15] Tobias Brixner, Jens Stenger, Harsha M Vaswani, Minhaeng Cho, Robert E Blankenship, and Graham R Fleming. Two-dimensional spectroscopy of electronic couplings in photosynthesis. *Nature*, 434(7033):625–628, 2005.

[16] Elad Harel and Gregory S Engel. Quantum coherence spectroscopy reveals complex dynamics in bacterial light-harvesting complex 2 (lh2). *Proceedings of the National Academy of Sciences*, 109(3):706–711, 2012.

[17] Franklin D Fuller, Jie Pan, Andrius Gelzinis, Vytautas Butkus, S Seckin Senlik, Daniel E Wilcox, Charles F Yocum, Leonas Valkunas, Darius Abramavicius, and Jennifer P Ogilvie. Vibronic coherence in oxygenic photosynthesis. *Nature chemistry*, 6(8):706–711, 2014.

[18] C Neil Hunter, Fevzi Daldal, Marion C Thurnauer, and J Thomas Beatty. *The purple phototrophic bacteria*, volume 28. Springer, 2009.

[19] Yonghui Zeng, Fuying Feng, Hana Medová, Jason Dean, and Michal Koblížek. Functional type 2 photosynthetic reaction centers found in the rare bacterial phylum gemmatimonadetes. *Proceedings of the National Academy of Sciences*, 111(21):7795–7800, 2014.

[20] Jean-David Rochaix. Regulation of photosynthetic electron transport. *Biochimica et Biophysica Acta (BBA)-Bioenergetics*, 1807(3):375–383, 2011.

[21] Roberta Croce and Herbert Van Amerongen. Natural strategies for photosynthetic light harvesting. *Nature chemical biology*, 10(7):492–501, 2014.

[22] Villy Sundström, Tõnu Pullerits, and Rienk van Grondelle. Photosynthetic light-harvesting: reconciling dynamics and structure of purple bacterial lh2 reveals function of photosynthetic unit, 1999.

[23] Herbert van Amerongen and Rienk van Grondelle. Understanding the energy transfer function of lhcii, the major light-harvesting complex of green plants, 2001.

[24] John TO Kirk. *Light and photosynthesis in aquatic ecosystems*. Cambridge university press, 1994.

[25] Yonghui Zeng and Michal Koblížek. Phototrophic gemmatimonadetes: A new "purple" branch on the bacterial tree of life. *Modern topics in the phototrophic prokaryotes: Environmental and applied aspects*, pages 163–192, 2017.

[26] Wim J Vredenberg and Louis NM Duysens. Transfer of energy from bacteriochlorophyll to a reaction centre during bacterial photosynthesis. *Nature*, 197(4865):355–357, 1963.

[27] GM McDermott, SM Prince, AA Freer, AM Hawthornthwaite-Lawless, MZ Papiz, RJea Cogdell, and NW Isaacs. Crystal structure of an integral membrane light-harvesting complex from photosynthetic bacteria. *Nature*, 374(6522):517–521, 1995.

[28] Juergen Koepke, Xiche Hu, Cornelia Muenke, Klaus Schulten, and Hartmut Michel. The crystal structure of the light-harvesting complex ii (b800–850) from rhodospirillum molischianum. *Structure*, 4(5):581–597, 1996.

[29] Richard J Cogdell, Alastair T Gardiner, Aleksander W Roszak, Christopher J Law, June Southall, and Neil W Isaacs. Rings, ellipses and horseshoes: how purple bacteria harvest solar energy. *Photosynthesis Research*, 81:207–214, 2004.

[30] Richard J Cogdell, Andrew Gall, and Jürgen Köhler. The architecture and function of the light-harvesting apparatus of purple bacteria: from single molecules to in vivo membranes. *Quarterly reviews of biophysics*, 39(3):227–324, 2006.

[31] Gregory D Scholes, Ian R Gould, Richard J Cogdell, and Graham R Fleming. Ab initio molecular orbital calculations of electronic couplings in the lh2 bacterial light-harvesting complex of rps. acidophila. *The Journal of Physical Chemistry B*, 103(13):2543–2553, 1999.

[32] MHC Koolhaas, RN Frese, GJS Fowler, TS Bibby, S Georgakopoulou, G Van der Zwan, CN Hunter, and R Van Grondelle. Identification of the upper exciton component of the b850 bacteriochlorophylls of the lh2 antenna complex, using a b800-free mutant of rhodobacter sphaeroides. *Biochemistry*, 37(14):4693–4698, 1998.

[33] Gregory D Scholes and Graham R Fleming. On the mechanism of light harvesting in photosynthetic purple bacteria: B800 to b850 energy transfer. *The Journal of Physical Chemistry B*, 104(8):1854–1868, 2000.

[34] Gregory D Scholes, Xanthipe J Jordanides, and Graham R Fleming. Adapting the förster theory of energy transfer for modeling dynamics in aggregated molecular assemblies. *The journal of physical chemistry B*, 105(8):1640–1651, 2001.

[35] Seogjoo Jang, Marshall D Newton, and Robert J Silbey. Multichromophoric förster resonance energy transfer. *Physical review letters*, 92(21):218301, 2004.

[36] Vladimir Chernyak and Shaul Mukamel. Collective coordinates for nuclear spectral densities in energy transfer and femtosecond spectroscopy of molecular aggregates. *The Journal of chemical physics*, 105(11):4565–4583, 1996.

[37] Wei Min Zhang, Torsten Meier, Vladimir Chernyak, and Shaul Mukamel. Exciton-migration and three-pulse femtosecond optical spectroscopies of photosynthetic antenna complexes. *The Journal of chemical physics*, 108(18):7763–7774, 1998.

[38] Rienk van Grondelle and Vladimir I Novoderezhkin. Energy transfer in photosynthesis: experimental insights and quantitative models. *Physical Chemistry Chemical Physics*, 8(7):793–807, 2006.

[39] Sussan Hess, Felix Feldchtein, Alexey Babin, Ildus Nurgaleev, Tonu Pullerits, Alexander Sergeev, and Villy Sundström. Femtosecond energy transfer within the lh2 peripheral antenna of the photosynthetic purple bacteria rhodobacter sphaeroides and rhodopseudomonas palustris ll. *Chemical physics letters*, 216(3-6):247–257, 1993.

[40] John TM Kennis, Alexandre M Streltsov, Simone IE Vulto, Thijs J Aartsma, Tsunenori Nozawa, and Jan Amesz. Femtosecond dynamics in isolated lh2 complexes of various species of purple bacteria. *The Journal of Physical Chemistry B*, 101(39):7827–7834, 1997.

[41] Jante M Salverda, Frank van Mourik, Gert van der Zwan, and Rienk van Grondelle. Energy transfer in the b800 rings of the peripheral bacterial light-harvesting complexes of rhodopseudomonas acidophila and rhodospirillum molischianum studied with photon echo techniques. *The Journal of Physical Chemistry B*, 104(47):11395–11408, 2000.

[42] V Sundström, R Van Grondelle, H Bergström, E Åkesson, and T Gillbro. Excitation-energy transport in the bacteriochlorophyll antenna systems of rhodospirillum rubrum and rhodobacter sphaeroides, studied by low-intensity pi-

cosecond absorption spectroscopy. *Biochimica et Biophysica Acta (BBA)-Bioenergetics*, 851(3):431–446, 1986.

[43] A Freiberg, VI Godik, T Pullerits, and K Timpmann. Directed picosecond excitation transport in purple photosynthetic bacteria. *Chemical physics*, 128(1):227–235, 1988.

[44] AP Shreve, JK Trautman, Harry A Frank, TG Owens, and AC Albrecht. Femtosecond energy-transfer processes in the b800–850 light-harvesting complex of rhodobacter sphaeroides 2.4. 1. *Biochimica et Biophysica Acta (BBA)-Bioenergetics*, 1058(2):280–288, 1991.

[45] S Hess, KJ Visscher, T Pullerits, V Sundström, GJS Fowler, and CN Hunter. Enhanced rates of subpicosecond energy transfer in blue-shifted light-harvesting lh2 mutants of rhodobacter sphaeroides. *Biochemistry*, 33(27):8300–8305, 1994.

[46] Gregory JS Fowler, Susan Hess, Tonu Pullerits, Villy Sundström, and C Neil Hunter. The role of βarg-10 in the b800 bacteriochlorophyll and carotenoid pigment environment within the light-harvesting lh2 complex of rhodobacter sphaeroides. *Biochemistry*, 36(37):11282–11291, 1997.

[47] Ying-Zhong Ma, Richard J Cogdell, and Tomas Gillbro. Energy transfer and exciton annihilation in the b800- 850 antenna complex of the photosynthetic purple bacterium rhodopseudomonas acidophila (strain 10050). a femtosecond transient absorption study. *The Journal of Physical Chemistry B*, 101(6):1087–1095, 1997.

[48] Tõnu Pullerits, Susan Hess, Jennifer L Herek, and Villy Sundström. Temperature dependence of excitation transfer in lh2 of rhodobacter sphaeroides. *The Journal of Physical Chemistry B*, 101(49):10560–10567, 1997.

[49] S Matsuzaki, V Zazubovich, NJ Fraser, RJ Cogdell, and GJ Small. Energy transfer dynamics in lh2 complexes of rhodopseudomonas a cidophila containing only one b800 molecule. *The Journal of Physical Chemistry B*, 105(29):7049–7056, 2001.

[50] Valter Zazubovich, Ryszard Jankowiak, and Gerald J Small. On b800→ b800 energy transfer in the lh2 complex of purple bacteria. *Journal of luminescence*, 98(1-4):123–129, 2002.

[51] Liu Wei-Min, Zhu Rong-Yi, Xia Chen-An, Liu Yuan, Xu Chun-He, and Qian Shi-Xiong. Femtosecond dynamics of energy transfer in native b800-b850 and b800-released lh2 complexes of rhodobacter sphaeroides. *Chinese physics letters*, 20(12):2148, 2003.

[52] A Kimura and T Kakitani. Theoretical analysis of the energy gap dependence of the reconstituted b800→ b850 excitation energy transfer rate in bacterial lh2 complexes. *The Journal of Physical Chemistry B*, 107(31):7932–7939, 2003.

[53] Andrew F Fidler, Ved P Singh, Phillip D Long, Peter D Dahlberg, and Gregory S Engel. Time scales of coherent dynamics in the light-harvesting complex 2 (lh2) of rhodobacter sphaeroides. *The journal of physical chemistry letters*, 4(9):1404–1409, 2013.

[54] Cathal Smyth, Daniel G Oblinsky, and Gregory D Scholes. B800–b850 coherence correlates with energy transfer rates in the lh2 complex of photosynthetic purple bacteria. *Physical Chemistry Chemical Physics*, 17(46):30805–30816, 2015.

[55] Pavel Malỳ, Alastair T Gardiner, Richard J Cogdell, Rienk Van Grondelle, and Tomáš Mančal. Robust light harvesting by a noisy antenna. *Physical Chemistry Chemical Physics*, 20(6):4360–4372, 2018.

[56] R Van Grondelle, H Bergström, V Sundström, and T Gillbro. Energy transfer within the bacteriochlorophyll antenna of purple bacteria at 77 k, studied by picosecond absorption recovery. *Biochimica et Biophysica Acta (BBA)-Bioenergetics*, 894(2):313–326, 1987.

[57] H Bergström, R Van Grondelle, and V Sundström. Characterization of excitation energy trapping in photosynthetic purple bacteria at 77 k. *FEBS letters*, 250(2):503–508, 1989.

[58] Andrew F Fidler, Ved P Singh, Phillip D Long, Peter D Dahlberg, and Gregory S Engel. Probing energy transfer events in the light harvesting complex 2 (lh2) of rhodobacter sphaeroides with two-dimensional spectroscopy. *The Journal of Chemical Physics*, 139(15), 2013.

[59] Sara C Massey, Po-Chieh Ting, Shu-Hao Yeh, Peter D Dahlberg, Sara H Sohail, Marco A Allodi, Elizabeth C Martin, Sabre Kais, C Neil Hunter, and Gregory S Engel. Orientational dynamics of transition dipoles and exciton relaxation in lh2 from ultrafast two-dimensional anisotropy. *The Journal of Physical Chemistry Letters*, 10(2):270–277, 2019.

[60] Marco Ferretti, Ruud Hendrikx, Elisabet Romero, June Southall, Richard J Cogdell, Vladimir I Novoderezhkin, Gregory D Scholes, and Rienk Van Grondelle. Dark states in the light-harvesting complex 2 revealed by two-dimensional electronic spectroscopy. *Scientific reports*, 6(1):20834, 2016.

[61] NRS Reddy, RJ Cogdell, L Zhao, and GJ Small. Nonphotochemical hole burning of the b800-b850 antenna complex of rhodopseudomonas acidophila. *Photochemistry and photobiology*, 57(1):35–39, 1993.

[62] Mirianas Chachisvilis, Oliver Kühn, Tonu Pullerits, and Villy Sundström. Exci-

tons in photosynthetic purple bacteria: wavelike motion or incoherent hopping? *The Journal of Physical Chemistry B*, 101(37):7275–7283, 1997.

[63] LD Book, AE Ostafin, N Ponomarenko, JR Norris, and NF Scherer. Exciton delocalization and initial dephasing dynamics of purple bacterial lh2. *The Journal of Physical Chemistry B*, 104(34):8295–8307, 2000.

[64] Ralph Jimenez, Frank van Mourik, Jae Young Yu, and Graham R Fleming. Three-pulse photon echo measurements on lh1 and lh2 complexes of rhodobacter sphaeroides: A nonlinear spectroscopic probe of energy transfer. *The Journal of Physical Chemistry B*, 101(37):7350–7359, 1997.

[65] Guangyu E Chen, Daniel P Canniffe, Samuel FH Barnett, Sarah Hollingshead, Amanda A Brindley, Cvetelin Vasilev, Donald A Bryant, and C Neil Hunter. Complete enzyme set for chlorophyll biosynthesis in escherichia coli. *Science Advances*, 4(1):eaaq1407, 2018.

[66] Melih Sener, Johan Strumpfer, Abhishek Singharoy, C Neil Hunter, and Klaus Schulten. Overall energy conversion efficiency of a photosynthetic vesicle. *Elife*, 5:e09541, 2016.

[67] Pu Qian, C Alistair Siebert, Peiyi Wang, Daniel P Canniffe, and C Neil Hunter. Cryo-em structure of the blastochloris viridis lh1–rc complex at 2.9 å. *Nature*, 556(7700):203–208, 2018.

[68] Long-Jiang Yu, Michihiro Suga, Zheng-Yu Wang-Otomo, and Jian-Ren Shen. Structure of photosynthetic lh1–rc supercomplex at 1.9 å resolution. *Nature*, 556(7700):209–213, 2018.

[69] Patrick F Tekavec, Thomas R Dyke, and Andrew H Marcus. Wave packet interferometry and quantum state reconstruction by acousto-optic phase modulation. *The Journal of chemical physics*, 125(19), 2006.

[70] Vivek Tiwari, Yassel Acosta Matutes, Alastair T Gardiner, Thomas LC Jansen, Richard J Cogdell, and Jennifer P Ogilvie. Spatially-resolved fluorescence-detected two-dimensional electronic spectroscopy probes varying excitonic structure in photosynthetic bacteria. *Nature Communications*, 9(1):4219, 2018.

[71] Tenzin Kunsel, Vivek Tiwari, Yassel Acosta Matutes, Alastair T Gardiner, Richard J Cogdell, Jennifer P Ogilvie, and Thomas LC Jansen. Simulating fluorescence-detected two-dimensional electronic spectroscopy of multichromophoric systems. *The Journal of Physical Chemistry B*, 123(2):394–406, 2018.

[72] Geoffrey A Lott, Alejandro Perdomo-Ortiz, James K Utterback, Julia R Widom, Alán Aspuru-Guzik, and Andrew H Marcus. Conformation of self-assembled porphyrin dimers in liposome vesicles by phase-modulation 2d fluorescence spectroscopy. *Proceedings of the National Academy of Sciences*, 108(40):16521–16526, 2011.

[73] Pavel Maly and Tomas Mancal. Signatures of exciton delocalization and exciton–exciton annihilation in fluorescence-detected two-dimensional coherent spectroscopy. *The Journal of Physical Chemistry Letters*, 9(19):5654–5659, 2018.

[74] Patrick F Tekavec, Geoffrey A Lott, and Andrew H Marcus. Fluorescence-detected two-dimensional electronic coherence spectroscopy by acousto-optic phase modulation. *The Journal of chemical physics*, 127(21), 2007.

[75] Shaul Mukamel. *Principles of nonlinear optical spectroscopy*. Number 6. Oxford University Press, USA, 1995.

[76] Paul N Butcher and David Cotter. *The elements of nonlinear optics*. Cambridge university press, 1990.

[77] Robert W Boyd. *Nonlinear optics*. Academic press, 2020.

[78] Andrei Tokmakoff. Time-dependent quantum mechanics and spectroscopy. 2014.

[79] Peter Hamm and Martin Zanni. *Concepts and methods of 2D infrared spectroscopy*. Cambridge University Press, 2011.

[80] David M Jonas. Two-dimensional femtosecond spectroscopy. *Annual review of physical chemistry*, 54(1):425–463, 2003.

[81] Agata M Brańczyk, Daniel B Turner, and Gregory D Scholes. Crossing disciplines-a view on two-dimensional optical spectroscopy. *Annalen der Physik*, 526(1-2):31–49, 2014.

[82] Richard R Ernst. Nuclear magnetic resonance fourier transform spectroscopy (nobel lecture). *Angewandte Chemie International Edition in English*, 31(7):805–823, 1992.

[83] Richard R Ernst, Geoffrey Bodenhausen, Alexander Wokaun, and Alfred G Redfield. Principles of nuclear magnetic resonance in one and two dimensions, 1989.

[84] Kristin LM Lewis and Jennifer P Ogilvie. Probing photosynthetic energy and charge transfer with two-dimensional electronic spectroscopy. *The journal of physical chemistry letters*, 3(4):503–510, 2012.

[85] Yumin Lee, Michael Gorka, John H Golbeck, and Jessica M Anna. Ultrafast energy transfer involving the red chlorophylls of cyanobacterial photosystem i probed through two-dimensional electronic spectroscopy. *Journal of the American Chemical Society*, 140(37):11631–11638, 2018.

[86] Andy S Sardjan, Floris P Westerman, Jennifer P Ogilvie, and Thomas LC Jansen. Observation of ultrafast coherence transfer and degenerate states with

polarization-controlled two-dimensional electronic spectroscopy. *The Journal of Physical Chemistry B*, 124(42):9420–9427, 2020.

[87] Jerome D Roscioli, Soumen Ghosh, Amy M LaFountain, Harry A Frank, and Warren F Beck. Structural tuning of quantum decoherence and coherent energy transfer in photosynthetic light harvesting. *The journal of physical chemistry letters*, 9(17):5071–5077, 2018.

[88] H Seiler, S Palato, and P Kambhampati. Investigating exciton structure and dynamics in colloidal cdse quantum dots with two-dimensional electronic spectroscopy. *The Journal of Chemical Physics*, 149(7), 2018.

[89] Steven T Cundiff, Alan D Bristow, Mark Siemens, Hebin Li, Galan Moody, Denis Karaiskaj, Xingcan Dai, and Tianhao Zhang. Optical 2-d fourier transform spectroscopy of excitons in semiconductor nanostructures. *IEEE Journal of Selected Topics in Quantum Electronics*, 18(1):318–328, 2011.

[90] Rohan Singh, Marten Richter, Galan Moody, Mark E Siemens, Hebin Li, and Steven T Cundiff. Localization dynamics of excitons in disordered semiconductor quantum wells. *Physical Review B*, 95(23):235307, 2017.

[91] Patrick Nuernberger, Stefan Ruetzel, and Tobias Brixner. Multidimensional electronic spectroscopy of photochemical reactions. *Angewandte Chemie International Edition*, 54(39):11368–11386, 2015.

[92] Sandra Doria, Timothy S Sinclair, Nathan D Klein, Doran IG Bennett, Chern Chuang, Francesca S Freyria, Colby P Steiner, Paolo Foggi, Keith A Nelson, Jianshu Cao, et al. Photochemical control of exciton superradiance in light-harvesting nanotubes. *ACS nano*, 12(5):4556–4564, 2018.

[93] Minhaeng Cho. *Two-dimensional optical spectroscopy*. CRC press, 2009.

[94] L Lepetit and Manuel Joffre. Two-dimensional nonlinear optics using fourier-transform spectral interferometry. *Optics letters*, 21(8):564–566, 1996.

[95] John D Hybl, Allison W Albrecht, Sarah M Gallagher Faeder, and David M Jonas. Two-dimensional electronic spectroscopy. *Chemical physics letters*, 297(3-4):307–313, 1998.

[96] Franklin D Fuller and Jennifer P Ogilvie. Experimental implementations of two-dimensional fourier transform electronic spectroscopy. *Annual review of physical chemistry*, 66:667–690, 2015.

[97] Tianhao Zhang, Camelia N Borca, Xiaoqin Li, and Steven T Cundiff. Optical two-dimensional fourier transform spectroscopy with active interferometric stabilization. *Optics Express*, 13(19):7432–7441, 2005.

[98] Somnath Biswas, JunWoo Kim, Xinzi Zhang, and Gregory D Scholes. Coherent two-dimensional and broadband electronic spectroscopies. *Chemical Reviews*, 122(3):4257–4321, 2022.

[99] David Paleček, Petra Edlund, Sebastian Westenhoff, and Donatas Zigmantas. Quantum coherence as a witness of vibronically hot energy transfer in bacterial reaction center. *Science Advances*, 3(9):e1603141, 2017.

[100] Erling Thyrhaug, Roel Tempelaar, Marcelo JP Alcocer, Karel Žídek, David Bína, Jasper Knoester, Thomas LC Jansen, and Donatas Zigmantas. Identification and characterization of diverse coherences in the fenna–matthews–olson complex. *Nature chemistry*, 10(7):780–786, 2018.

[101] Sang-Hee Shim, David B Strasfeld, Yun L Ling, and Martin T Zanni. Automated 2d ir spectroscopy using a mid-ir pulse shaper and application of this technology to the human islet amyloid polypeptide. *Proceedings of the National Academy of Sciences*, 104(36):14197–14202, 2007.

[102] Lauren P DeFlores, Rebecca A Nicodemus, and Andrei Tokmakoff. Two-dimensional fourier transform spectroscopy in the pump-probe geometry. *Optics letters*, 32(20):2966–2968, 2007.

[103] Erik M Grumstrup, Sang-Hee Shim, Matthew A Montgomery, Niels H Damrauer, and Martin T Zanni. Facile collection of two-dimensional electronic spectra using femtosecond pulse-shaping technology. *Optics Express*, 15(25):16681–16689, 2007.

[104] Jeffrey A Myers, Kristin LM Lewis, Patrick F Tekavec, and Jennifer P Ogilvie. Two-color two-dimensional fourier transform electronic spectroscopy with a pulse-shaper. *Optics express*, 16(22):17420–17428, 2008.

[105] Zhengyang Zhang, Kym Lewis Wells, Edward William James Hyland, and Howe-Siang Tan. Phase-cycling schemes for pump–probe beam geometry two-dimensional electronic spectroscopy. *Chemical Physics Letters*, 550:156–161, 2012.

[106] Victor Volkov, Roland Schanz, and Peter Hamm. Active phase stabilization in fourier-transform two-dimensional infrared spectroscopy. *Optics letters*, 30(15):2010–2012, 2005.

[107] ML Cowan, JP Ogilvie, and RJD Miller. Two-dimensional spectroscopy using diffractive optics based phased-locked photon echoes. *Chemical Physics Letters*, 386(1-3):184–189, 2004.

[108] JP Ogilvie, M Armstrong, A Nagy, and RJD Miller. Diffractive optics-based heterodyne detected three-pulse photon echo. In *International Conference on Ultrafast Phenomena*, page WD20. Optica Publishing Group, 2002.

[109] Tobias Brixner, Igor V Stiopkin, and Graham R Fleming. Tunable two-dimensional femtosecond spectroscopy. *Optics letters*, 29(8):884–886, 2004.

[110] Tobias Brixner, Tomáš Mančal, Igor V Stiopkin, and Graham R Fleming. Phase-stabilized two-dimensional electronic spectroscopy. *The Journal of chemical physics*, 121(9):4221–4236, 2004.

[111] Ulrike Selig, Florian Langhojer, Frank Dimler, Tatjana Löhrig, Christoph Schwarz, Björn Gieseking, and Tobias Brixner. Inherently phase-stable coherent two-dimensional spectroscopy using only conventional optics. *Optics letters*, 33(23):2851–2853, 2008.

[112] Ismael A Heisler, Roberta Moca, Franco VA Camargo, and Stephen R Meech. Two-dimensional electronic spectroscopy based on conventional optics and fast dual chopper data acquisition. *Review of Scientific Instruments*, 85(6), 2014.

[113] Haibin Zheng, Justin R Caram, Peter D Dahlberg, Brian S Rolczynski, Subha Viswanathan, Dmitriy S Dolzhnikov, Amir Khadivi, Dmitri V Talapin, and Gregory S Engel. Dispersion-free continuum two-dimensional electronic spectrometer. *Applied optics*, 53(9):1909–1917, 2014.

[114] Yizhu Zhang, Kristina Meyer, Christian Ott, and Thomas Pfeifer. Passively phase-stable, monolithic, all-reflective two-dimensional electronic spectroscopy based on a four-quadrant mirror. *Optics Letters*, 38(3):356–358, 2013.

[115] Joshua C Vaughan, T Hornung, KW Stone, and Keith A Nelson. Coherently controlled ultrafast four-wave mixing spectroscopy. *The Journal of Physical Chemistry A*, 111(23):4873–4883, 2007.

[116] Kenan Gundogdu, Katherine W Stone, Daniel B Turner, and Keith A Nelson. Multidimensional coherent spectroscopy made easy. *Chemical Physics*, 341(1-3):89–94, 2007.

[117] Wolfgang Wagner, Chunqiang Li, John Semmlow, and Warren S Warren. Rapid

phase-cycled two-dimensional optical spectroscopy in fluorescence and transmission mode. *Optics express*, 13(10):3697–3706, 2005.

[118] Adrien Bercegol, F Javier Ramos, Amelle Rebai, Thomas Guillemot, Jean-Baptiste Puel, Jean-Francois Guillemoles, Daniel Ory, Jean Rousset, and Laurent Lombez. Spatial inhomogeneity analysis of cesium-rich wrinkles in triple-cation perovskite. *The Journal of Physical Chemistry C*, 122(41):23345–23351, 2018.

[119] J-S Kang, G Kim, SC Wi, SS Lee, S Choi, Sunglae Cho, SW Han, KH Kim, HJ Song, HJ Shin, et al. Spatial chemical inhomogeneity and local electronic structure of mn-doped ge ferromagnetic semiconductors. *Physical review letters*, 94(14):147202, 2005.

[120] Gaël Nardin, Travis M Autry, Kevin L Silverman, and Steven T Cundiff. Multidimensional coherent photocurrent spectroscopy of a semiconductor nanostructure. *Optics express*, 21(23):28617–28627, 2013.

[121] Fikeraddis A Damtie, Andreas Wacker, Tõnu Pullerits, and Khadga J Karki. Two-dimensional action spectroscopy of excitonic systems: Explicit simulation using a phase-modulation technique. *Physical Review A*, 96(5):053830, 2017.

[122] Khadga J Karki, Junsheng Chen, Atsunori Sakurai, Qi Shi, Alastair T Gardiner, Oliver Kühn, Richard J Cogdell, and Tönu Pullerits. Before förster. initial excitation in photosynthetic light harvesting. *Chemical science*, 10(34):7923–7928, 2019.

[123] Khadga J Karki, Julia R Widom, Joachim Seibt, Ian Moody, Mark C Lonergan, Tonu Pullerits, and Andrew H Marcus. Coherent two-dimensional photocurrent spectroscopy in a pbs quantum dot photocell. *Nature communications*, 5(1):5869, 2014.

[124] Luca Bolzonello, Francisco Bernal-Texca, Luis G Gerling, Jana Ockova, Elisabetta Collini, Jordi Martorell, and Niek F Van Hulst. Photocurrent-detected 2d electronic spectroscopy reveals ultrafast hole transfer in operating pm6/y6 organic solar cells. *The Journal of Physical Chemistry Letters*, 12(16):3983–3988, 2021.

[125] Sebastian Roeding and Tobias Brixner. Coherent two-dimensional electronic mass spectrometry. *Nature Communications*, 9(1):2519, 2018.

[126] Martin Aeschlimann, Tobias Brixner, Alexander Fischer, Christian Kramer, Pascal Melchior, Walter Pfeiffer, Christian Schneider, Christian Strüber, Philip Tuchscherer, and Dmitri V Voronine. Coherent two-dimensional nanoscopy. *Science*, 333(6050):1723–1726, 2011.

[127] Artem A Bakulin, Carlos Silva, and Eleonora Vella. Ultrafast spectroscopy with photocurrent detection: watching excitonic optoelectronic systems at work. *The journal of physical chemistry letters*, 7(2):250–258, 2016.

[128] Lukas Bruder, Alexander Eisfeld, Ulrich Bangert, Marcel Binz, Max Jakob, Daniel Uhl, Markus Schulz-Weiling, Edward R Grant, and Frank Stienkemeier. Delocalized excitons and interaction effects in extremely dilute thermal ensembles. *Physical Chemistry Chemical Physics*, 21(5):2276–2282, 2019.

[129] Pavel Malỳ, Julian Lüttig, Stefan Mueller, Maximilian H Schreck, Christoph Lambert, and Tobias Brixner. Coherently and fluorescence-detected two-dimensional electronic spectroscopy: Direct comparison on squaraine dimers. *Physical Chemistry Chemical Physics*, 22(37):21222–21237, 2020.

[130] Vivek Tiwari, Yassel Acosta Matutes, Arkaprabha Konar, Zhanqian Yu, Marcin Ptaszek, David F Bocian, Dewey Holten, Christine Kirmaier, and Jennifer P Ogilvie. Strongly coupled bacteriochlorin dyad studied using phase-modulated

fluorescence-detected two-dimensional electronic spectroscopy. *Optics express*, 26(17):22327–22341, 2018.

[131] Stefan Mueller, Julian Luttig, Luisa Brenneis, Dan Oron, and Tobias Brixner. Observing multiexciton correlations in colloidal semiconductor quantum dots via multiple-quantum two-dimensional fluorescence spectroscopy. *ACS nano*, 15(3):4647–4657, 2021.

[132] Qingzhen Bian, Fei Ma, Shula Chen, Qi Wei, Xiaojun Su, Irina A Buyanova, Weimin M Chen, Carlito S Ponseca Jr, Mathieu Linares, Khadga J Karki, et al. Vibronic coherence contributes to photocurrent generation in organic semiconductor heterojunction diodes. *Nature communications*, 11(1):617, 2020.

[133] Ninghao Zhou, Zhenyu Ouyang, Jun Hu, Olivia F Williams, Liang Yan, Wei You, and Andrew M Moran. Distinguishing energy-and charge-transfer processes in layered perovskite quantum wells with two-dimensional action spectroscopies. *The Journal of Physical Chemistry Letters*, 11(12):4570–4577, 2020.

[134] Peifang Tian, Dorine Keusters, Yoshifumi Suzaki, and Warren S Warren. Femtosecond phase-coherent two-dimensional spectroscopy. *Science*, 300(5625):1553–1555, 2003.

[135] Arijit K De, Daniele Monahan, Jahan M Dawlaty, and Graham R Fleming. Two-dimensional fluorescence-detected coherent spectroscopy with absolute phasing by confocal imaging of a dynamic grating and 27-step phase-cycling. *The Journal of Chemical Physics*, 140(19), 2014.

[136] Simon Draeger, Sebastian Roeding, and Tobias Brixner. Rapid-scan coherent 2d fluorescence spectroscopy. *Optics express*, 25(4):3259–3267, 2017.

[137] Sebastian Goetz, Donghai Li, Verena Kolb, Jens Pflaum, and Tobias Brixner.

Coherent two-dimensional fluorescence micro-spectroscopy. *Optics express*, 26(4):3915–3925, 2018.

[138] Alejandro Perdomo-Ortiz, Julia R Widom, Geoffrey A Lott, Alan Aspuru-Guzik, and Andrew H Marcus. Conformation and electronic population transfer in membrane-supported self-assembled porphyrin dimers by 2d fluorescence spectroscopy. *The Journal of Physical Chemistry B*, 116(35):10757–10770, 2012.

[139] Julia R Widom, Neil P Johnson, Peter H von Hippel, and Andrew H Marcus. Solution conformation of 2-aminopurine dinucleotide determined by ultraviolet two-dimensional fluorescence spectroscopy. *New journal of physics*, 15(2):025028, 2013.

[140] Daan Brinks, Richard Hildner, Erik MHP Van Dijk, Fernando D Stefani, Jana B Nieder, Jordi Hernando, and Niek F Van Hulst. Ultrafast dynamics of single molecules. *Chemical Society Reviews*, 43(8):2476–2491, 2014.

[141] Oliver Kuhn, Tomas Mancal, and Tõnu Pullerits. Interpreting fluorescence detected two-dimensional electronic spectroscopy. *The Journal of Physical Chemistry Letters*, 11(3):838–842, 2020.

[142] Marco Schröter, Tõnu Pullerits, and Oliver Kühn. Using fluorescence detected two-dimensional spectroscopy to investigate initial exciton delocalization between coupled chromophores. *The Journal of Chemical Physics*, 149(11), 2018.

[143] Alex Arash Sand Kalaee, Fikeraddis Damtie, and Khadga Jung Karki. Differentiation of true nonlinear and incoherent mixing of linear signals in action-detected 2d spectroscopy. *The Journal of Physical Chemistry A*, 123(19):4119–4124, 2019.

[144] Matteo Bruschi, Federico Gallina, and Barbara Fresch. Simulating action-2d electronic spectroscopy of quantum dots: insights on the exciton and biexciton

interplay from detection-mode and time-gating. *Physical Chemistry Chemical Physics*, 24(45):27645–27659, 2022.

[145] Matteo Bruschi, Luca Bolzonello, Federico Gallina, and Barbara Fresch. Unifying nonlinear response and incoherent mixing in action-2d electronic spectroscopy. *The Journal of Physical Chemistry Letters*, 14(30):6872–6879, 2023.

[146] Luca Bolzonello, Matteo Bruschi, Barbara Fresch, and Niek F. van Hulst. Nonlinear optical spectroscopy of molecular assemblies: What is gained and lost in action detection? *The Journal of Physical Chemistry Letters*, 0(0):11438–11446, 0. PMID: 38085697.

[147] Khadga Jung Karki, Loni Kringle, Andrew H Marcus, and Tõnu Pullerits. Phase-synchronous detection of coherent and incoherent nonlinear signals. *Journal of Optics*, 18(1):015504, 2015.

[148] Pavel Malỳ, Stefan Mueller, Julian Lüttig, Christoph Lambert, and Tobias Brixner. Signatures of exciton dynamics and interaction in coherently and fluorescence-detected four-and six-wave-mixing two-dimensional electronic spectroscopy. *The Journal of Chemical Physics*, 153(14), 2020.

[149] Ilaria Bargigia, Elizabeth Gutiérrez-Meza, David A Valverde-Chávez, Sarah R Marques, Ajay Ram Srimath Kandada, and Carlos Silva. Identifying incoherent mixing effects in the coherent two-dimensional photocurrent excitation spectra of semiconductors. *The Journal of Chemical Physics*, 157(20), 2022.

[150] Pascal Grégoire, Ajay Ram Srimath Kandada, Eleonora Vella, Chen Tao, Richard Leonelli, and Carlos Silva. Incoherent population mixing contributions to phase-modulation two-dimensional coherent excitation spectra. *The Journal of Chemical Physics*, 147(11), 2017.

[151] Ben Brüggemann, Jennifer L Herek, Villy Sundström, Tonu Pullerits, and Volkhard May. Microscopic theory of exciton annihilation: Application to the lh2 antenna system. *The Journal of Physical Chemistry B*, 105(46):11391–11394, 2001.

[152] Mino Yang and Graham R Fleming. Third-order nonlinear optical response of energy transfer systems. *The Journal of chemical physics*, 111(1):27–39, 1999.

[153] Howe-Siang Tan. Theory and phase-cycling scheme selection principles of collinear phase coherent multi-dimensional optical spectroscopy. *The Journal of chemical physics*, 129(12), 2008.

[154] Dorine Keusters, Howe-Siang Tan, and Warren S. Warren. Role of pulse phase and direction in two-dimensional optical spectroscopy. *The Journal of Physical Chemistry A*, 103(49):10369–10380, 1999.

[155] Yin Song, Arkaprabha Konar, Riley Sechrist, Ved Prakash Roy, Rong Duan, Jared Dziurgot, Veronica Policht, Yassel Acosta Matutes, Kevin J Kubarych, and Jennifer P Ogilvie. Multispectral multidimensional spectrometer spanning the ultraviolet to the mid-infrared. *Review of Scientific Instruments*, 90(1), 2019.

[156] Stephanie E Sanders, Muyi Zhang, Ariba Javed, and Jennifer P Ogilvie. Expanding the bandwidth of fluorescence-detected two-dimensional electronic spectroscopy using a broadband continuum probe pulse pair. *Optics Express*, 32(6):8887–8902, 2024.

[157] Chen S Tsai. *Guided-wave acousto-optics: interactions, devices, and applications*, volume 23. Springer Science & Business Media, 2013.

[158] SALEH BEA and MC Teich. Fundamentals of photonics. *Wiley*, page 313, 1991.

[159] Nicholas M Kearns, Randy D Mehlenbacher, Andrew C Jones, and Martin T Zanni. Broadband 2d electronic spectrometer using white light and pulse shaping: noise and signal evaluation at 1 and 100 khz. *Optics express*, 25(7):7869–7883, 2017.

[160] Andrew M Weiner. Ultrafast optical pulse shaping: A tutorial review. *Optics Communications*, 284(15):3669–3692, 2011.

[161] I Pastirk, X Zhu, RM Martin, and M Dantus. Remote characterization and dispersion compensation of amplified shaped femtosecond pulses using miips. *Optics Express*, 14(19):8885–8889, 2006.

[162] Marcos Dantus, Vadim V Lozovoy, and Igor Pastirk. Miips characterizes and corrects femtosecond pulses. *Laser Focus World*, 43(5):101, 2007.

[163] Mattia Russo, Anna Paola Casazza, Giulio Cerullo, Stefano Santabarbara, and Margherita Maiuri. Direct evidence for excitation energy transfer limitations imposed by low-energy chlorophylls in photosystem i–light harvesting complex i of land plants. *The Journal of Physical Chemistry B*, 125(14):3566–3573, 2021.

[164] H Bouchiat, K Yunusova, D Konstantinov, and A Chepelianskii. Coupling between rydberg states and landau levels of electrons trapped on liquid helium.

[165] Elisabetta Collini. 2d electronic spectroscopic techniques for quantum technology applications. *The Journal of Physical Chemistry C*, 125(24):13096–13108, 2021.

[166] James Lim, David Paleček, Felipe Caycedo-Soler, Craig N Lincoln, Javier Prior, Hans Von Berlepsch, Susana F Huelga, Martin B Plenio, Donatas Zigmantas, and Jürgen Hauer. Vibronic origin of long-lived coherence in an artificial molecular light harvester. *Nature communications*, 6(1):7755, 2015.

[167] Daniel Uhl, Ulrich Bangert, Lukas Bruder, and Frank Stienkemeier. Coherent optical 2d photoelectron spectroscopy. *Optica*, 8(10):1316–1324, 2021.

[168] Lukas Bruder, Ulrich Bangert, Marcel Binz, Daniel Uhl, Romain Vexiau, Nadia Bouloufa-Maafa, Olivier Dulieu, and Frank Stienkemeier. Coherent multidimensional spectroscopy of dilute gas-phase nanosystems. *Nature Communications*, 9(1):4823, 2018.

[169] Meredith G McNamee, Zhenyu Ouyang, Liang Yan, Zijian Gan, Ninghao Zhou, Olivia F Williams, Wei You, and Andrew M Moran. Uncovering transport mechanisms in perovskite materials and devices with recombination-induced action spectroscopies. *The Journal of Physical Chemistry C*, 127(6):2782–2791, 2023.

[170] Erling Thyrhaug, Marco Schröter, Eglė Bukartė, Oliver Kühn, Richard Cogdell, Jürgen Hauer, and Donatas Zigmantas. Intraband dynamics and exciton trapping in the lh2 complex of rhodopseudomonas acidophila. *The Journal of Chemical Physics*, 154(4), 2021.

[171] Andrew F Fidler, Ved P Singh, Phillip D Long, Peter D Dahlberg, and Gregory S Engel. Dynamic localization of electronic excitation in photosynthetic complexes revealed with chiral two-dimensional spectroscopy. *Nature communications*, 5(1):3286, 2014.

[172] Vadim Cherezov, Jeffrey Clogston, Miroslav Z Papiz, and Martin Caffrey. Room to move: crystallizing membrane proteins in swollen lipidic mesophases. *Journal of molecular biology*, 357(5):1605–1618, 2006.

[173] Vladimir Novoderezhkin, Markus Wendling, and Rienk Van Grondelle. Intra- and interband transfers in the b800- b850 antenna of rhodospirillum m olis-

chianum: Redfield theory modeling of polarized pump- probe kinetics. *The Journal of Physical Chemistry B*, 107(41):11534–11548, 2003.

[174] Arkaprabha Konar, Riley Sechrist, Yin Song, Veronica R Policht, Philip D Laible, David F Bocian, Dewey Holten, Christine Kirmaier, and Jennifer P Ogilvie. Electronic interactions in the bacterial reaction center revealed by two-color 2d electronic spectroscopy. *The Journal of Physical Chemistry Letters*, 9(18):5219–5225, 2018.

[175] Jianmin Yang, Maxim F Gelin, Lipeng Chen, František Šanda, Erling Thyrhaug, and Jürgen Hauer. Two-dimensional fluorescence excitation spectroscopy: A novel technique for monitoring excited-state photophysics of molecular species with high time and frequency resolution. *The Journal of Chemical Physics*, 159(7), 2023.

[176] Ivana Šímová, Valentyna Kuznetsova, Alastair T Gardiner, Václav Šebelík, Michal Koblížek, Marcel Fuciman, and Tomáš Polívka. Carotenoid responds to excess energy dissipation in the lh2 complex from rhodoblastus acidophilus. *Photosynthesis Research*, 154(1):75–87, 2022.

[177] Damianos Agathangelou, Ariba Javed, Francesco Sessa, Xavier Solinas, Manuel Joffre, and Jennifer P Ogilvie. Phase-modulated rapid-scanning fluorescence-detected two-dimensional electronic spectroscopy. *The Journal of Chemical Physics*, 155(9), 2021.

[178] Ariba Javed, Damianos Agathangelou, Francesco Sessa, Xavier Solinas, Manuel Joffre, and Jennifer P Ogilvie. Phase-modulated rapid-scanning fluorescence-detected two-dimensional electronic spectroscopy. In *Multiscale Imaging and Spectroscopy III*, volume 11944, pages 40–51. SPIE, 2022.

[179] WP Aue, E Bartholdi, and Richard R Ernst. Two-dimensional spectroscopy.

application to nuclear magnetic resonance. *The Journal of Chemical Physics*, 64(5):2229–2246, 1976.

[180] AD Bristow, D Karaiskaj, X Dai, T Zhang, C Carlsson, KR Hagen, R Jimenez, and ST Cundiff. A versatile ultrastable platform for optical multidimensional fourier-transform spectroscopy. *Review of Scientific Instruments*, 80(7), 2009.

[181] Khadga J Karki, Junsheng Chen, Atsunori Sakurai, Qi Shi, Alastair T Gardiner, Oliver Kühn, Richard J Cogdell, and Tönu Pullerits. Unexpectedly large delocalization of the initial excitation in photosynthetic light harvesting. *arXiv preprint arXiv:1804.04840*, 2018.

[182] Suxia Yan and Howe-Siang Tan. Phase cycling schemes for two-dimensional optical spectroscopy with a pump–probe beam geometry. *Chemical Physics*, 360(1-3):110–115, 2009.

[183] Travis M Autry, Galan Moody, James Fraser, Corey McDonald, Richard P Mirin, and Kevin Silverman. Single-scan acquisition of multiple multidimensional spectra. *Optica*, 6(6):735–744, 2019.

[184] Norbert F Scherer, Roger J Carlson, Alexander Matro, Mei Du, Anthony J Ruggiero, Victor Romero-Rochin, Jeffrey A Cina, Graham R Fleming, and Stuart A Rice. Fluorescence-detected wave packet interferometry: Time resolved molecular spectroscopy with sequences of femtosecond phase-locked pulses. *The Journal of chemical physics*, 95(3):1487–1511, 1991.

[185] Fujin Long, Teresa B Freedman, Rick Hapanowicz, and Laurence A Nafie. Comparison of step-scan and rapid-scan approaches to the measurement of mid-infrared fourier transform vibrational circular dichroism. *Applied spectroscopy*, 51(4):504–507, 1997.

[186] L Mertz. Rapid scanning fourier transform spectrometry. *Le Journal de Physique Colloques*, 28(C2):C2–87, 1967.

[187] Peter R Griffiths. Fourier transform infrared spectrometry. *Science*, 222(4621):297–302, 1983.

[188] Zachary W Fox, Tyler J Blair, Robert B Weakly, Trevor L Courtney, and Munira Khalil. Implementation of continuous fast scanning detection in femtosecond fourier-transform two-dimensional vibrational-electronic spectroscopy to decrease data acquisition time. *Review of Scientific Instruments*, 89(11), 2018.

[189] Stefan Mueller, Julian Lüttig, Pavel Malỳ, Lei Ji, Jie Han, Michael Moos, Todd B Marder, Uwe HF Bunz, Andreas Dreuw, Christoph Lambert, et al. Rapid multiple-quantum three-dimensional fluorescence spectroscopy disentangles quantum pathways. *Nature Communications*, 10(1):4735, 2019.

[190] EA Donley, TP Heavner, F Levi, MO Tataw, and SR Jefferts. Erratum:"double-pass acousto-optic modulator system"[rev. sci. instrum. 76, 063112 (2005)]. *Review of Scientific Instruments*, 90(4):049901, 2019.

[191] Eric Martin. *Coherent Spectroscopy at the Diffraction Limit*. PhD thesis, 2018.

[192] Xiaonan Ma, Jakub Dostál, and Tobias Brixner. Broadband 7-fs diffractive-optic-based 2d electronic spectroscopy using hollow-core fiber compression. *Optics Express*, 24(18):20781–20791, 2016.

[193] Patrick F Tekavec, Jeffrey A Myers, Kristin LM Lewis, and Jennifer P Ogilvie. Two-dimensional electronic spectroscopy with a continuum probe. *Optics letters*, 34(9):1390–1392, 2009.

[194] Jakub Dostál, Jakub Pšenčík, and Donatas Zigmantas. In situ mapping of the energy flow through the entire photosynthetic apparatus. *Nature Chemistry*, 8(7):705–710, 2016.

[195] Andrew Niedringhaus, Veronica R Policht, Riley Sechrist, Arkaprabha Konar, Philip D Laible, David F Bocian, Dewey Holten, Christine Kirmaier, and Jennifer P Ogilvie. Primary processes in the bacterial reaction center probed by two-dimensional electronic spectroscopy. *Proceedings of the National Academy of Sciences*, 115(14):3563–3568, 2018.

[196] Tobias A Gellen, Laurie A Bizimana, William P Carbery, Ilana Breen, and Daniel B Turner. Ultrabroadband two-quantum two-dimensional electronic spectroscopy. *The Journal of Chemical Physics*, 145(6), 2016.